Alma Mater Studiorum · Università di Bologna

DIPARTIMENTO DI FISICA E ASTRONOMIA

Dottorato di ricerca in Astronomia

Ciclo XXVIII

Non-thermal emission in High Frequency Peaked blazars towards the Square Kilometer Array era

Relatore:
Chiar.mo Prof.
Gabriele Giovannini

Co-Relatori:
Dott. ***Marcello Giroletti***
Dott.ssa ***Monica Orienti***

Coordinatore:
Chiar.mo Prof.
Lauro Moscardini

Tesi di Dottorato di:
Rocco Lico

Settore Concorsuale: 02/C1 Astronomia, Astrofisica, Fisica della Terra e dei Pianeti
Settore Scientifico-Disciplinare: FIS/05 Astronomia e Astrofisica

Esame finale anno 2015

The present thesis work was carried out
in the framework of the research activities
of the Observatory of Radioastronomy (INAF, Bologna)

Ai miei genitori.

Contents

Introduction

In the class of Active Galactic Nuclei (AGN), blazars are the most extreme objects. They show a pair of prominent relativistic plasma jets closely aligned with our line of sight, powered from the gravitational potential of a super massive black hole (with a mass up to $\sim 10^9 M_\odot$), accreting matter and gas from the surrounding medium. Their emission is mainly non-thermal and it is detected throughout the electromagnetic spectrum, with a typical two-humped spectral energy distribution (SED). Due to their peculiar geometry, these jet structures are detected at extreme cosmological distances thanks to the strong Doppler boosting effects produced by the bulk relativistic motion. For this reason they are among the most powerful objects in the Universe.

Understanding the details of the production mechanism and the fueling processes of the relativistic jets is crucial to understand the physics of the matter in extremely compact states, the physics of high energy plasma and the role of magnetic fields. In recent years, the field of γ-ray astrophysics has greatly developed, thanks to the advent of the Large Area Telescope (LAT) on-board the *Fermi* satellite, which detects γ rays in the energy range between $\sim$20 MeV and $\sim$300 GeV, and of ground-based Cherenkov telescopes which allow us to study very-high energy (VHE, $E > 0.1$ TeV) γ rays. These instruments have clearly revealed that blazars dominate the census of the γ-ray sky.

Exploring the possible correlation between radio and γ-ray emission is a central issue to understand the blazar emission processes, and several works and observing campaigns were dedicated to this topic (e.g. Kovalev et al. 2009; Ghirlanda

et al. 2010; Giroletti et al. 2010; Ackermann et al. 2011a; Mufakharov et al. 2015). However, while a strong correlation between radio and γ-ray emission in the energy range 100 MeV–100 GeV was clearly demonstrated (Ackermann et al. 2011a), the possible correlation radio-VHE still remains elusive and unexplored. Any possible physical implication based on the relation between the two bands has remained hidden, mainly due to the lack of an homogeneous coverage of the VHE sky. Currently, VHE observations of blazars are conducted by imaging atmospheric Cherenkov telescopes (IACTs), which mainly operate in pointing mode with a limited sky coverage, and in general they observe sources in a peculiar state. All of these limitations introduce a strong bias in VHE catalogs, and it is difficult to assess any possible radio-VHE correlation.

At present, the First *Fermi*-LAT Catalog of Sources above 10 GeV (1FHL, Ackermann et al. 2013), represents the best resource for addressing the connection between radio and hard γ-ray emission, approaching and partly overlapping with the VHE band. The 1FHL catalog is based on LAT data accumulated during the first 3 years of the *Fermi* mission. Since *Fermi* operates in sky survey mode, the 1FHL provides us, for the first time, a large, deep and unbiased sample which is ideal to gather γ-ray data in the energy range 10-500 GeV.

Hard blazars are generally of the High Synchrotron Peaked (HSP) type, with the synchrotron SED component peaking at $\nu > 10^{15}$ Hz, characterized by low Compton dominance, low synchrotron luminosity, and peculiar very long baseline interferometric (VLBI) properties: their parsec scale jets are less variable in flux density and structure than in other blazars, and in general the inferred Doppler factors are far from the extreme values required at higher frequencies. About 40% of 1FHL blazars are of HSP type and the investigation of their properties provides us with details about the blazar sequence (Fossati et al. 1998), and the interaction of VHE photons with the extragalactic background light.

In this thesis work we will explore and discuss the properties of 1FHL sources, considering both blazars and the non negligible fraction of still unassociated gamma-

ray sources (UGS, 13%). We perform a statistical analysis of a complete sample of hard γ-ray sources, included in the 1FHL catalog, mostly composed of HSP blazars, and we present new VLBI observations of the faintest members of the sample. The new VLBI data, complemented by an extensive search of the archives for brighter sources, are essential to gather a sample as large as possible for the assessment of the significance of the correlation between radio and VHE emission bands.

UGS constitute 13% of the 1FHL, and about the 30% of every other *Fermi* catalog. Are these UGS just unrecognized blazars or more exotic objects? Do they show the same radio vs. high energy γ-ray connection found for the other γ-ray sources? With the new VLBI observations of the present work we will be able not only to definitively confirm the blazar nature of some 1FHL sources, but we will propose a reliable association for some UGS with a high significance.

After the characterization of the statistical properties of HSP blazars and UGS, we use a complementary approach, by focusing on an intensive multi-frequency observing VLBI and γ-ray campaign carried out for one of the most remarkable and closest HSP blazar Markarian 421 (Mrk 421).

In general HSP blazars show a violent variability on short timescales, from the order of years to few days, that is sometimes accompanied by the ejection of superluminal blobs. This violent activity suggests that the central engine is not stationary, and, due to the very short timescales involved, this behavior can be related to rapid changes in the magnetic field. For this reason, we investigate the inner jet structure of Mrk 421 on the finest possible linear scales: in radio, we can do this directly with parsec-scale imaging, by means of a one-year multi-frequency VLBI monitoring, both in total and in polarized intensity; in γ rays, we infer information on small spatial scales through the construction and analysis of a weekly-binned light curve. We constrain the geometry and kinematics of the jet by studying the evolution of shocks that arise in it and we estimate some important quantities and parameters such as the jet viewing angle, the Doppler factor and the bright-

ness temperature. Thanks to the electric vector position angles (EVPA) and the Faraday rotation analysis we obtain information about the magnetic field topology both in the core and in the jet region. Finally, we compare the information gathered from the radio and the γ-ray data.

From the study and results of the present thesis work it emerges how much important it is to achieve a higher sensitivity to understand the physical mechanisms occurring in hard γ-ray blazars. In general, faint *Fermi*-LAT sources are also faint radio sources. The weakest γ-ray sources detect by *Fermi* have 1.4 GHz flux densities of few mJy, and the unassociated ones are expected to be fainter.

The Square Kilometer Array (SKA), which is a new generation revolutionary aperture synthesis radio telescope, with its exceptional sensitivity (at μJy level) and large field of view, will be the ideal instrument to better characterize these sources and to disentangle among the low frequency candidate counterparts. In particular, the synergy between SKA and the new generation Cherenkov telescope Array (CTA), will provide us with the perfect chance to investigate the possible radio-VHE emission connection and to identify and reveal the nature of the unidentified *Fermi* high energy sources.

The thesis is laid out as follows: the first three Chapters are devoted to an introduction of the science topics and observing techniques: in Chapter 1 we introduce and describe the properties of AGNs in general and of blazars in particular; in Chapter 2 we describe some relativistic effects which play an important role in the observational properties of blazar jets; in Chapter 3 there is an introduction about the observing instruments and techniques used in this work: radio interferometry and VLBI technique, the Large Area Telescope on board the *Fermi* satellite and the new generation aperture synthesis radio telescope SKA.

Chapters 4 and 5 are focused on the 1FHL sample: in Chapter 4 we present our new VLBI observations for the faintest 1FHL sources; in Chapter 5 there are the results about the radio and γ-ray emission correlation analysis together with the correlation significance assessment.

The last two Chapters deal with the one-year broadband monitoring of the HSP blazar Mrk 421: Chapter 6 contains results about the total intensity analysis of the multi-epoch multi-frequency VLBI monitoring; in Chapter 7 we report on the polarimetric parsec-scale analysis, the γ-ray light curve, and their connection.

Throughout this work, we use a ΛCDM cosmology with $h = 0.71$, $\Omega_m = 0.27$, and $\Omega_\Lambda = 0.73$ (Komatsu et al. 2009). The radio spectral index is defined such that $S(\nu) \propto \nu^{-\alpha}$ and the γ-ray photon index Γ such that $dN_{\mathrm{photon}}/dE \propto E^{-\Gamma}$. All angles are measured from north through east.

Chapter 1

The blazar family

1.1 Active Galaxies

About 1% of the galaxies in the Universe show features that are markedly different with respect to those observed in the "normal" ones. These galaxies have a typical luminosity that is $L \sim 10^{47} - 10^{48}\,\mathrm{erg\,s^{-1}}$, i.e. about three orders of magnitude higher than what is found in a typical galaxy, and it cannot be solely attributed to the emission of stars, gas and dust. The huge amount of energy originates in the central compact region of these galaxies, called Active Galactic Nucleus (AGN), and the host galaxy is called active galaxy.

Under the name of active galaxies various sub-classes of objects are included (e.g. quasars, Seyfert galaxies, radio galaxies, blazars), which differ from each other in brightness, morphology, distance, variability and polarization degree.

However, some features seem to be common to all the different AGN classes, and a standard unified model was built. The basic scheme of this model, as reported in Fig.1.1, foresees the presence of a **super-massive black hole** (SMBH, with a mass of $\sim 10^{6-10} M_{\odot}$), which acts as a central engine. Due to the gravity of the SMBH, the surrounding gas falls towards the center, dissipating angular momentum due to viscosity and turbulent motions, and forms an **accretion disk**

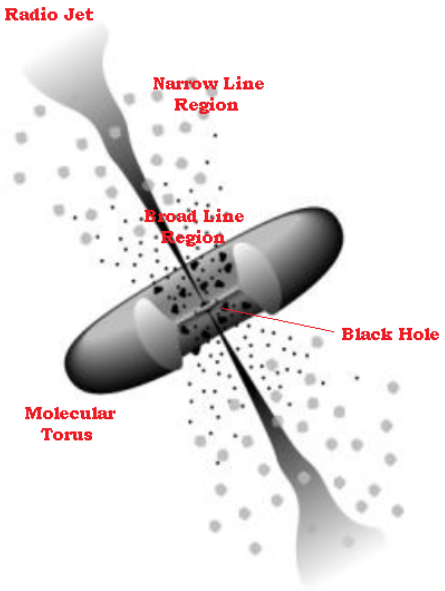

Figure 1.1: Schematic representation of the current AGN paradigm. Image adapted from Urry & Padovani (1995).

around the central engine, extending for about 10^{-3} pc (Krolik 1999). The accretion disk is responsible of the thermal emission in the optical-UV wavebands. In addition, above the disk, a hot corona forms, in which X-ray photons are produced by means of inverse Compton (IC) scattering of optical-UV photons coming from the disk.

Above the disk, at $\sim 0.01 - 0.1$ pc from the core, there is a region known as the **broad line region** (BLR), formed by moving and turbulent gas clouds which can reach electron densities of the order of 10^{8-11} cm^{-3}. Being close to the black hole, these clouds have high rotational speeds ($\sim 500 - 10^4$ km s^{-1}) and produce broad lines in the observed spectrum, because of Doppler effect. Beyond this region, between $\sim 1 - 100$ pc from the core, there is an optically thick **dusty torus**, which produces IR emission by reprocessing the optical/UV photons coming from the disk and re-radiating them at longer wavelengths.

Going outward (between $\sim 10^2 - 10^3$ pc from the core region), there is a

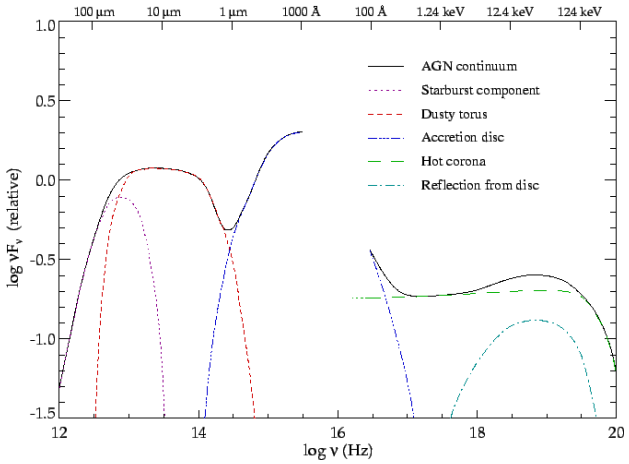

Figure 1.2: Schematic representation of the broadband continuum spectral energy distribution of AGNs. The main components are: the infrared bump, which is thought to be re-radiated emission from the dust torus; the Big Blue Bump (UV/Optical) from thermal emission from the accretion disk; and the X-ray emission from Comptonization of disk photons in a hot corona. Image from Elvis et al. (1994).

region of low-density clouds (electron densities of the order of 10^{4-6} cm^{-3}), with rotational speeds lower than $\sim 10^3$ km s^{-1}, producing narrow emission lines. This outer region is known as **narrow line region** (NLR) and is responsible for the forbidden lines observed in the spectrum (i.e. emission lines that in environments with higher densities would be suppressed by collisional processes).

A schematic representation of the broadband continuum emission spectrum of AGNs, with the contribution from the different components, is shown in Fig. 1.2.

It is clear how this unisotropic structure is highly directional (see Fig. 1.3): the observed spectrum and features strongly depend on the angle that this structure forms with the line of sight (Urry & Padovani 1995). In particular, when the molecular torus intercepts the line of sight, it can hide the emission of the internal regions (disk emission and emission lines produced by the BLR).

It should be noticed that this is a basic model. Although it could not take into account all the observational properties of the whole AGN class, it successfully

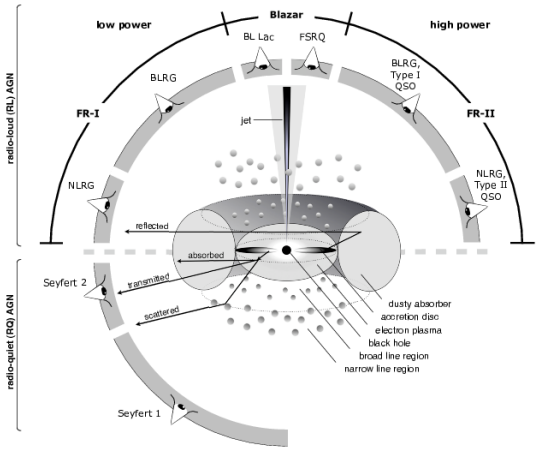

Figure 1.3: A cartoon of the AGN unified model from Beckmann & Shrader (2012). Depending on the viewing angle different type of objects are seen. Radio-loud and radio-quiet objects are represented in the top and in the bottom part of the image, respectively.

explains most of them. However, there are some clues indicating that also some intrinsic different properties are responsible of the AGN diversification. Some of the main discriminant parameters are thought to be the mass accretion rate onto the SMBH and the SMBH spin (e.g. D'Elia & Cavaliere 2001; Chiaberge & Marconi 2011).

1.1.1 Radio-loud AGNs

About 10% of the entire AGN population form bipolar and powerful **jet structures**, originating in the central region along the rotation axis of the black hole (Peterson 1997). These jets, which can extend from a few pc up to several Mpc, are mainly made of relativistic plasma, whose particles are accelerated and, by interacting with the radiation field and the magnetic field, produce part of the observed spectrum. These sources are classified as radio-loud sources, which means that the ratio of flux densities in the radio at 5 GHz and in the optical B-band in the source rest frame is higher than 10 (Kellermann et al. 1989).

Table 1.1: FRI and FRII properties.

FRI	FRII
$\log P_{1.4} < 10^{24.5}$ Watt Hz^{-1}	$\log P_{1.4} > 10^{24.5}$ Watt Hz^{-1}
diffuse jets	highly collimated jets
no hot spots	bright hot spots
edge-darkened	edge-brightened
weak optical emission lines	strong optical emission lines

Radio galaxies are the most common radio-loud AGNs. When we talk about radio galaxies, we intend extragalactic and spatially resolved radio sources, usually associated with giant elliptical galaxies, whose broadband spectrum is dominated by non-thermal emission. Their structure includes two radio jets, and in the most powerful ones, bow shocks create extended and diffuse structures called *radio lobes*.

The family of radio galaxies is further divided into two sub-classes, depending on the radio power and morphological features. The astronomers Fanaroff and Riley in 1974 noticed that when the radio power at 178 MHz of a radio galaxy is higher than $\sim 10^{25}$ Watt Hz^{-1} Sr^{-1}, there is a change in the source morphology. The fainter radio sources are called Fanaroff-Riley Type I (FRI), whereas the more powerful ones are called Fanaroff-Riley Type II (FRII).

From a morphological point of view, in FRI radio galaxies jets appear symmetrical, bright and diffuse, while in FRIIs there are well collimated, asymmetric and low-luminosity jets. In FRIIs the jet ends in a compact and bright region called *hot spot* at the edge of the lobes (edge-brightened), while in FRIs hot spots are absent and the lobes appear brighter in the inner part (edge-darkened). These differences may be related to the radiative efficiency of the accretion flow: in FRIIs the accretion is more efficient than in the FRIs (Ghisellini & Celotti 2001). The main properties and differences between FRI and FRII radio galaxies are summarized in Table 1.1.

Radio-loud AGNs with their jet structures closely aligned to the line of sight form the class of the so called **blazars**. In these objects the Doppler boosting effect plays a major role and produces high variability throughout the electromagnetic spectrum, high degree of radio and optical polarization and high brightness temperature (see Sect. 2). Moreover, apparent superluminal motions of jet components can be detected with high angular resolution observations. Due to this peculiar geometrical configuration, blazars represent the most extreme AGN family and they are less than 5% of the entire AGN class.

Blazars are the main topic of this thesis and their properties will be extensively discussed in Sect. 1.2.

1.2 The blazar properties

The blazar family consists of two sub-classes: BL Lacertae objects (hereafter BL Lacs) and Flat Spectrum Radio Quasars (hereafter FSRQs). Historically, they are classified into FSRQs and BL Lacs on the basis of their optical properties: FSRQs show broad and strong emission lines in their optical spectra while the optical spectra of BL Lacs are almost featureless.

In this section we will describe the main properties of blazars.

1.2.1 Variability

The study of the variability plays an important role for understanding the source physical state and for estimating the size of the emitting regions.

Blazars are among the most variable extragalactic objects, both in amplitude and timescales. Before entering into discussion, we should remind that when we speak about variability we intend a sudden increase in the emission intensity with respect to a flat or a slowly variable background, followed by a gradual decrease to the initial value. These intensity variations, called *outbursts*, usually are not regular (no evidence of any systematic periodicity have been established so far)

and occur over timescales that can range from several years to a few days. In some cases outbursts can be accompanied by structural changes in the source (e.g. Orienti et al. 2013; Jorstad et al. 2013).

After decades of efforts in the study of relativistic jets, many issues still remain elusive, as the jet launching mechanism and acceleration, the precise location of the high energy emitting region and the jet structure itself. Among the various scenarios proposed for explaining the observed variability, there is the so called "shock-in-jet" model (Marscher & Gear 1985) which foresees that a shock originates from a disturbance in the nuclear region and expands downstream across the jet region, producing both radio and high energy emission. On the other hand, there are pieces of evidence of relativistic jets showing a transverse velocity structure, in which the radio and the high energy emission originate in different regions (e.g. Ghisellini et al. 2005; Gabuzda et al. 2014).

With the argument of causality, from the observed variability it is possible to estimate the size of the emitting region. In other words, given a source of radiation of size Δd, from an external reference system, it cannot be measured variability on time scales which are shorter than the time that the light would take to travel a distance equal to the size of the source ($\Delta d < c\Delta t$).

Extremely short variability timescales, and therefore small sizes, imply high brightness temperature (T_B) values, within the synchrotron model framework. The brightness temperature, which is a different way of expressing the radiated power, is defined as the temperature that a black body should have to radiate the observed brightness. We can write T_B as a function of the source angular size (e.g. Piner et al. 1999; Tingay et al. 1998):

$$T_{\rm B} = 1.22 \times 10^{12} \frac{S\,(1+z)}{ab\nu^2} \ \ {\rm K} \tag{1.1}$$

where S is the flux density of the component measured in Jy, a and b are the full widths at half maximum of the major and minor axes respectively of the component measured in mas, z is the redshift, and ν is the observation frequency in GHz.

The brightness temperature can also be written as a function of the variability timescale (e.g. Hovatta et al. 2009):

$$T_{\mathrm{B,var}} = 1.548 \times 10^{-32} \frac{\Delta S_{\mathrm{max}} d_L^2}{\nu^2 \tau^2 (1+z)^{1+\alpha}} \ \mathrm{K} \tag{1.2}$$

where ν is the observed frequency in GHz, z is the redshift, d_L is the luminosity distance in meters, ΔS_{max} is the difference between the maximum and the minimum value of the core flux density in Jy, τ is the variability timescale and α is the spectral index.

For small values of τ, the observed T_B can reach high values, in some cases exceeding the IC process critical threshold value of 10^{12} K (Kellermann & Pauliny-Toth 1969). When the brightness temperature exceeds this limit, the Compton brightness dominates over the synchrotron brightness, and because of the rapid energy losses due to inverse Compton effect the source quickly cools down (Compton catastrophe).

On the other hand, by fixing $T_B \leq 10^{12}$K in Eq. 1.1 it is possible to obtain a lower limit for the angular size of the source. In some cases, from this estimation, it emerges that the diameter of the source should be much larger than the value obtained from the observed variability. This apparent inconsistency is explained in the context of relativistic theories presented in Sect. 2.

1.2.2 Broadband spectral properties

In Astronomy, when we deal with multi-frequency studies, the standard way to represent spectra is by means of the Spectral Energy Distribution (SED). It consists in representing $\log(\nu F_\nu)$ vs. $\log(\nu)$, where ν is the photon frequency and F_ν is the energy flux per frequency unit. In other words, we represent the source power per natural logarithmic frequency intervals with the big advantage of directly showing the relative energy output in each single frequency interval.

From the analysis of several blazar spectra, a universal trend in the $\log(\nu F_\nu)$ vs. $\log(\nu)$ plane was identified, represented by two non-thermal components. This

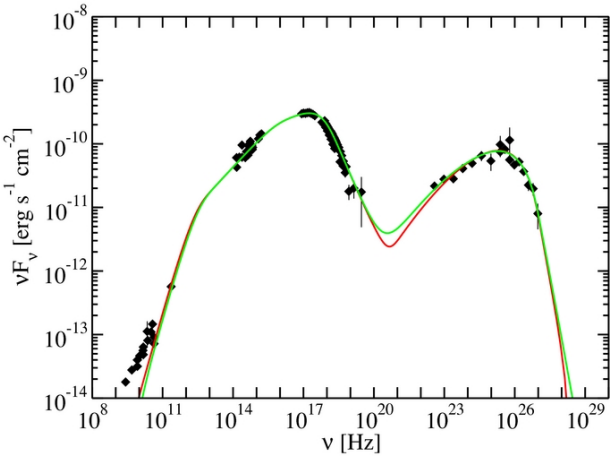

Figure 1.4: Spectral energy distribution of Mrk 421 obtained with two one-zone synchrotron-self-Compton model fits, by using different minimum variability timescales: t_{var} = 1 day (red curve) and t_{var} = 1 hr (green curve). For further details see Abdo et al. (2011).

can be seen in Fig. 1.4 where the SED of the blazar Markarian 421 (Mrk 421) is shown. Two broad humps cover the entire electro-magnetic spectrum from radio to γ rays, whose peaks can lay at different energies, depending on the physical properties of the object that we are considering.

The low-frequency component, as suggested by the power law trend and the high degree of polarization observed in radio and optical bands, is due to synchrotron emission by relativistic electrons moving along the magnetic field lines. The synchroton hump peak (ν^{Syn}_{peak}) can be found in the spectral region extending from radio to soft X-ray energies, and it reflects the maximum energy at which particles can be accelerated (Giommi et al. 2012a). According to the convention proposed by Abdo et al. (2010a), depending on the ν^{Syn}_{peak} position, blazars are classified as: Low Synchrotron Peaked (LSP) with $\nu^{Syn}_{peak} < 10^{14}$ Hz, Intermediate Synchrotron Peaked (ISP) with 10^{14} Hz $< \nu^{Syn}_{peak} < 10^{15}$ Hz , and High Synchrotron Peaked (HSP) with $\nu^{Syn}_{peak} > 10^{15}$ Hz (see Fig. 1.5). In general FSRQs are predominantly LSP objects, while BL Lacs could be of all the three types.

The high-frequency component peaks from X-ray to γ-ray frequencies, in an energy range from keV to TeV. While there are many and stringent indications that the low-frequency component is due to synchrotron radiation, the origin of the high energy emission component is not so obvious. It is important to understand which kind of relativistic particles are responsible for the high energy component. There are two main families of models: the hadronic model, in which relativistic protons within the jet are the ultimate responsible for the observed emission, and the leptonic model, in which leptons play a dominant role.

According to hadronic models, protons within the jet interact with the surrounding photons, producing $e^{\pm}$ pairs, which by means of synchrotron processes, produce the high-frequency emission represented by the second hump in the observed spectrum (e.g. Mannheim 1993). However, being protons more massive than electrons, the acceleration efficiency is lower and they have longer cooling times. Moreover, protons require magnetic fields of the order of tens of Gauss to produce the observed emission.

On the other hand, leptonic models explain the high energy emission through IC scattering between relativistic electrons in the jet (the same ones responsible for the synchrotron emission) and surrounding low energy photons.

To date, no definitive indication has been found to discern between these two scenarios. However the following observational pieces of evidence favor the leptonic model for the high frequency emission:

- the similar trend of the two non-thermal humps points out that the particles responsible for the high energy emission are the same producing the synchrotron emission at lower frequencies;
- in some objects, when one of the two peaks is higher or lower, the same behavior is then reflected in the other one;
- for a variability in the low frequency component, a subsequent instability in the high energy component is usually observed.

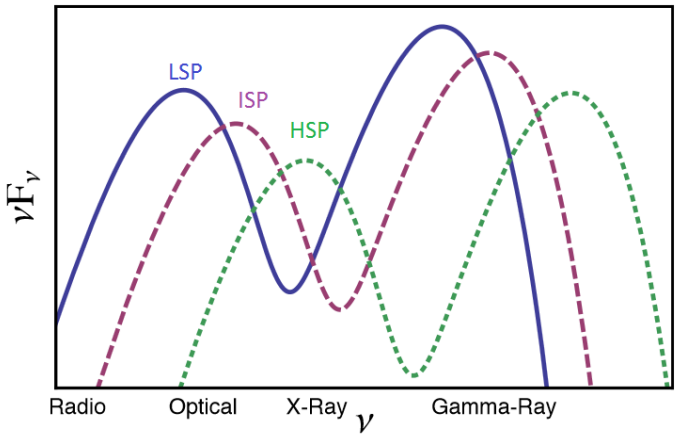

Figure 1.5: Blazar classification according to the synchrotron peak (ν^{Syn}_{peak}) position in the Spectral energy distribution: Low Synchrotron Peaked (LSP) with $\nu^{Syn}_{peak} < 10^{14}$ Hz, Intermediate Synchrotron Peaked (ISP) with 10^{14} Hz $< \nu^{Syn}_{peak} < 10^{15}$ Hz , and High Synchrotron Peaked (HSP) with $\nu^{Syn}_{peak} > 10^{15}$ Hz.

This observational evidence is naturally explained by leptonic models, which easily reproduce the multi-frequency observed properties, while it is more difficult to conciliate them with hadronic models. Moreover, the TeV emission is better explained within the leptonic scenario: being the electrons less massive, it is easier to accelerate them by shocks to such high energies.

Regarding the scattered photons involved in the IC process, they may be the same photons produced by synchrotron emission within the jet (Synchrotron Self Compton model or SCC, Maraschi et al. 1992), or photons from external sources such as the accretion disk, the BLR and/or the dusty torus (External Radiation Compton Model or ERC, Dermer et al. 1992; Sikora et al. 1994; Ghisellini & Madau 1996; Sikora et al. 2008).

The density of the radiation field plays an important role in the physics of these peculiar objects: both components of the spectrum move to lower frequencies when the brightness of the radio source increases (see Fig. 1.5). Basically, all electrons are accelerated at similar energies. However, in the most powerful

sources (i.e. the most luminous) the photon density is higher, therefore relativistic electrons cool more efficiently, and as a consequence, the emission shifts to lower frequencies (Ghisellini et al. 1998).

From the above mentioned SSC model, in which the high energy emission is produced by IC scattering of the synchrotron photons, another important property emerges. The peak frequency of the low energy (LE) synchrotron component is related to the magnetic field intensity and the energy distribution function of electrons. On the other hand, the peak frequency of the high energy (HE) inverse Compton component is related to the radiation field intensity and the energy distribution function of electrons. Therefore, in the jet we expect that the ratio between the brightness of the LE and HE components reflects the ratio between the energy density of the radiation field and of the magnetic field.

1.2.3 The blazar's divide

In this section we focus our attention on the main differences between the two blazar sub-groups, trying to understand if they are intrinsically different objects or if their differences are only apparent.

According to the optical classification of FSRQs and BL Lacs, for practical reasons, a threshold rest-frame equivalent width (EW) of 5Å was adopted to separate the two classes (Stickel et al. 1991). However no evidence of any bi-modal broad line EW distribution was ever found; of course there are also transition objects. By analyzing the properties of blazar spectral energy distributions, Ghisellini et al. (2011) proposed a refined method to classify the objects belonging to the two families, based on the luminosity of the BLR measured in Eddington units.

Blazar optical emission spectra are the result of a mix of three emission components: a non-thermal component coming from the jet, a thermal component originating in the accretion disk and in the BLR, and the host galaxy light. These three components are represented in Fig. 1.6 by red, blue and orange lines, respec-

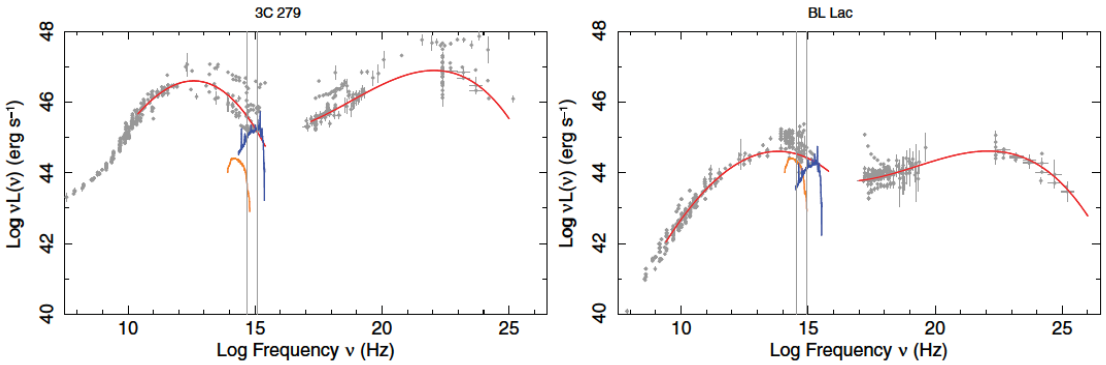

Figure 1.6: Spectral energy distribution for the FSRQs 3C 279 (left panel), and the BL Lac object BL Lacertae (right panel). Color lines represent the three main contributions to the blazar SEDs: non-thermal emission from the jet (red line), emission from the disc and from the BLR (blue line), and emission from the host galaxy (orange line). The two vertical grey lines denote the optical observing window (3800-8000 Å). For additional details see Giommi et al. (2012b).

tively, for the FSRQ 3C 279 and BL Lacertae.

Aside from the presence or not of emission lines in the optical spectra, there are other distinctive properties which characterize these two sub-classes. In the following we summarize the main differences:

- Redshift distribution: BL Lacs are closer than FSRQs (Fig. 1.7). BL Lacs are usually found at a redshift $z \lesssim 0.6$; this value is obtained by considering those objects for which a redshift estimation is possible (about 50% of known BL Lacs completely lack any detectable feature in their optical spectra). On the other hand, FSRQs usually lay in the redshift range $z \sim 1 - 2$, and in some cases they are detected up to $z \sim 5.5$ (Giommi et al. 2012b).

- Cosmological evolution: FSRQs show a strong cosmological evolution, while BL Lacs do not show any sign of such strong evolution (see e.g., Caccianiga et al. 2002). In particular, in the X-ray band, BL Lacs do not

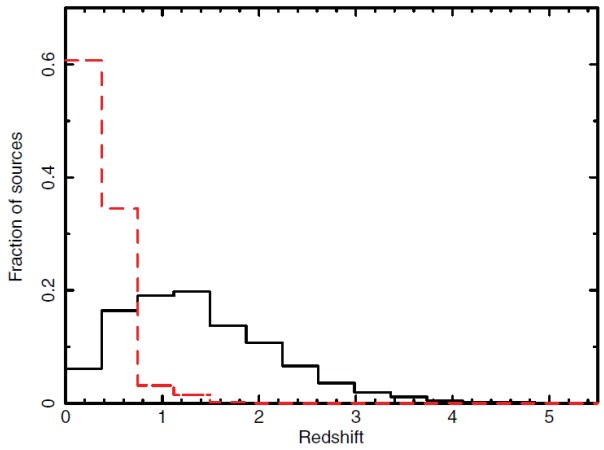

Figure 1.7: Redshift distribution of a sample of 1676 FSRQs (black solid line) and 537 BL Lacs (red dashed line) in the third edition of the BZCAT catalog (Massaro et al. 2009).

show evolution at all or they show negative evolution (Padovani et al. 2007; Rector et al. 2000); i.e. in the past they were less numerous (and luminous) than now.

- Distribution of the synchrotron peak in SEDs: for FSRQs the synchroton hump always peaks at frequencies $\lesssim 10^{14.5}$ Hz, while for BL Lacs it is shifted to higher frequencies, reaching in some cases values as high as 10^{18} Hz.

- γ-ray photon index Γ_γ distribution: FSRQs tend to cluster at the softest index values (i.e. $\Gamma_\gamma > 2$) while BL Lacs tend to have the hardest values (i.e. $\Gamma_\gamma < 2$).

- Integrated power: FSRQs are more luminous than BL Lacs. FSRQs have integrated power $L \sim 10^{46-48}$ erg s^{-1}, while for BL Lacs $L \lesssim 10^{46}$ erg s^{-1}.

These properties are summarized in Table 1.2.

The main blazar distinctive features are well explained in terms of beamed emission (Blandford & Rees 1978), originating in a relativistic jet closely aligned

to the line of sight, with Lorentz bulk factor (Γ) in the range 5-20 (Urry & Padovani 1995). This hypothesis implies a large number of "parent" objects (the so called **parent population**), i.e. objects which are intrinsically identical to FSRQs and BL Lacs, respectively, but misaligned with respect to the line of sight. To look for the parent population, a good method consists in comparing the extended radio emission, which, being far from the central regions, is not affected by the jet orientation and relativistic effects are less important.

In this framework, the most plausible candidates as the BL Lac parent population are the FRI (low-luminosity) radio galaxies while for FSRQs the most plausible parent objects are represented by FRII (high-luminosity) radio galaxies. Therefore, in this picture, FSRQs and BL Lacs represent the beamed fraction of FRII and FRI radio galaxies, respectively. For example, by selecting two complete samples of BL Lacs and FRI radio galaxies at 5 GHz, Padovani (1992) found similar values for the extended emission for both samples.

Moreover, in support of the beaming model, it was found that the predicted luminosity functions for the beamed sources, given the luminosity functions of the parent populations, are in good agreement with observations (Padovani & Urry 1992; Padovani et al. 2007).

Some authors (e.g., Vagnetti et al. 1991; Böttcher & Dermer 2002) proposed an evolutionary connection between the two blazar sub-classes. In this picture FSRQs evolve into BL Lacs, in which the emission lines are masked by a strongly enhanced optical continuum. Other authors (e.g, Ostriker & Vietri 1990) suggested that BL Lacs could be gravitational microlensed FSRQs, with their continuum emission strongly amplified by stars in a foreground galaxy. In both scenarios BL Lacs and FSRQs are considered to be the same objects.

However, by selecting and analyzing two complete samples of FSRQs and BL Lacs, Padovani (1992) ruled out the microlensing hypothesis as the main mechanism responsible for the blazar's divide. Moreover, an evolutionary connection between two blazar sub-classes was not in agreement with the results of the same

Table 1.2: FSRQs vs. BL Lacs - differences.

Property	BL Lacs	FSRQs
Optical spectrum	no or weak emission lines	strong emission lines
Typical redshift	$z < 0.6$	$z > 1$
Cosmological evolution	weak or negative	strong and positive
Integrated power	$L \lesssim 10^{46}\,\mathrm{erg\,s^{-1}}$	$L \sim 10^{46-48}\,\mathrm{erg\,s^{-1}}$
Synchrotron SED peak	$> 10^{15}$ Hz	$\lesssim 10^{14.5}$ Hz
Extended radio emission	FRI like	FRII like
SED photon energy	GeV/TeV	MeV/GeV
γ-ray photon index	$\Gamma_\gamma < 2$	$\Gamma_\gamma > 2$

work. Padovani (1992) showed that the emission lines in BL Lacs are intrinsically weak. Therefore they are not quasars whose emission lines are masked by a strongly amplified optical continuum, and argued that BL Lacs and FSRQs do not have any direct connection but represent the manifestation of similar relativistic phenomena, occurring in radio galaxies with different intrinsic power.

1.2.4 The blazar sequence

At the end of the 90s, Fossati et al. (1998) made a statistical study of the two blazar sub-classes by selecting a sample of 126 blazar objects. They built and analyzed the SEDs for all the selected objects and looked for any regularity in their trend. This was an essential step to better understand the nature of blazars and they found important outcomes.

Fossati et al. (1998) divided the selected sources into radio luminosity bins, averaging data belonging to the same bin. By looking at the SED trends, they found that the peak frequencies of the LE and HE components correlate, and their position depends on the radio/total power: when the radio/total power increases, both the LE and HE peaks shift to lower frequencies. This is represented in Fig. 1.8.

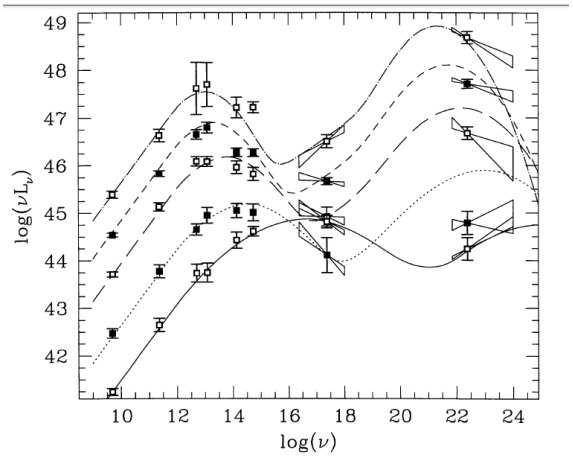

Figure 1.8: Average spectral energy distributions for a sample of 126 blazars. The overlaying curves represent the analytic approximations obtained according to the one-parameter-family definition described in Fossati et al. (1998).

Another relevant finding of this work is that the luminosity ratio for the two peaks ($L_{HE}^{peak}/L_{LE}^{peak}$), also known as Compton dominance, increases with the bolometric luminosity.

According to the spectral classification of blazars, we note that LSP objects are more luminous, with the LE and HE humps peaking at IR-Optical and MeV-GeV, respectively, while HSPs are less luminous, with the LE and HE humps peaking at UV-X and GeV-TeV, respectively. ISP objects have intermediate properties. The

Table 1.3: FSRQs vs. BL Lacs - Blazar sequence properties.

Property	FSRQs	BL Lacs
Radio power	high	low
LE peak	IR	IR-X
HE peak	keV-MeV	MeV-TeV
Compton dominance	high	low
Bolometric power	high	low

main properties are summarized in Table 1.3.

This is an important result because, for the first time, by using a single parameter (the luminosity), all blazar objects are unified in a unique sequence. The blazar sequence trend was confirmed by Donato et al. (2001), who added hard X-ray spectra, and by Meyer et al. (2011), who analyzed the multi-wavelength (MWL) spectrum of several hundred blazars. However, some authors argue that the blazar sequence could be an apparent effect due to an observational bias (e.g., Padovani et al. 2007). To date, observations are in agreement with the blazar sequence model, as well as the detection and discovery of BL Lac objects of HSP type emitting up to TeV energies.

1.3 High Synchrotron Peaked blazars

Blazars with the synchrotron hump peaking in the X-ray band are classified as high frequency peaked (HSP, $\nu_{peak}^{Syn} > 10^{15}$ Hz) objects, and they are good candidates for being TeV γ-ray emitters. Indeed, among the 60 currently known TeV blazars (as reported in TevCat[1]), about the 77% (46/60) of them belong to the HSP class.

A peculiar feature of HSP objects is that at TeV energies they display a very fast variability, on timescales of the order of few minutes, as reported by several works (see e.g., Aharonian et al. 2007; Sakamoto et al. 2008). Various attempts were made to explain the fast variability (e.g., Barkov et al. 2012; Nalewajko et al. 2011; Begelman et al. 2008), and all of them claim the presence of high bulk Lorentz factors ($\geq$25) for the γ-ray emitting plasma in the relativistic jet structures. Moreover, high values of the bulk Lorentz factors and Doppler factors are necessary to model their SED (e.g., Tavecchio et al. 2010).

In general, and in agreement with the anti-correlation between ν_{peak}^{Syn} an L_γ described by the blazar sequence, at radio wavelengths the HSP blazars are rel-

[1] `http://tevcat.uchicago.edu/`

atively low luminosity sources. Thanks to the VLBI technique (Sect. 3.1) it is possible to directly image their parsec scale structure, and to study their kinematic properties by means of multi-epoch VLBI observations. A relevant finding, arising from numerous kinematic analysis (e.g., Piner & Edwards 2014; Blasi et al. 2013; Lico et al. 2012; Giroletti et al. 2004b), is the detection, within their jets, of slowly moving features ($< c$), which in some cases are consistent with being stationary. The absence of superluminal features seems to be a distinctive characteristic of HSP blazars. Moreover, in HSP blazars, the measured brightness temperature reaches values which require modest bulk Doppler and Lorentz factors in their parsec-scale radio jets. This is in contrast with the high values for the Doppler and Lorentz factors required from the γ-ray data. This aspect is known as *Doppler factor crisis*, and may indicate that radio and γ-ray emission originate in different regions with different Lorentz factors. Based on this multi-emission-region assumption, several multi-component models were proposed, e.g. models which foresee either the presence of spine-layer structures (e.g., Ghisellini et al. 2005), or the presence of mini-jets within the main one (e.g., Giannios et al. 2009), or a deceleration occurring in the jet (e.g., Georganopoulos & Kazanas 2003). All of these models invoke the presence of velocity structures within the jet. Such velocity structures may produce distinctive observable features, such as limb brightening or transverse electric vector position angle (EVPA) distribution, which were clearly detected in many works (e.g., Giroletti et al. 2004b, 2008; Piner et al. 2009, 2010; Blasi et al. 2013; Lico et al. 2014).

HSP blazars are not only ideal to investigate the particle acceleration mechanisms in some of the most extreme environments in the Universe, but they also offer a precious contribution to obtain indirect constraints on the so-called Extragalactic Background Light (EBL). After the cosmic microwave background (CMB), the EBL is the most dominant cosmological radiation field in the Universe, containing the diffuse radiation that stars and galaxies have emitted since they formed. The EBL contains information about the radiative history and the

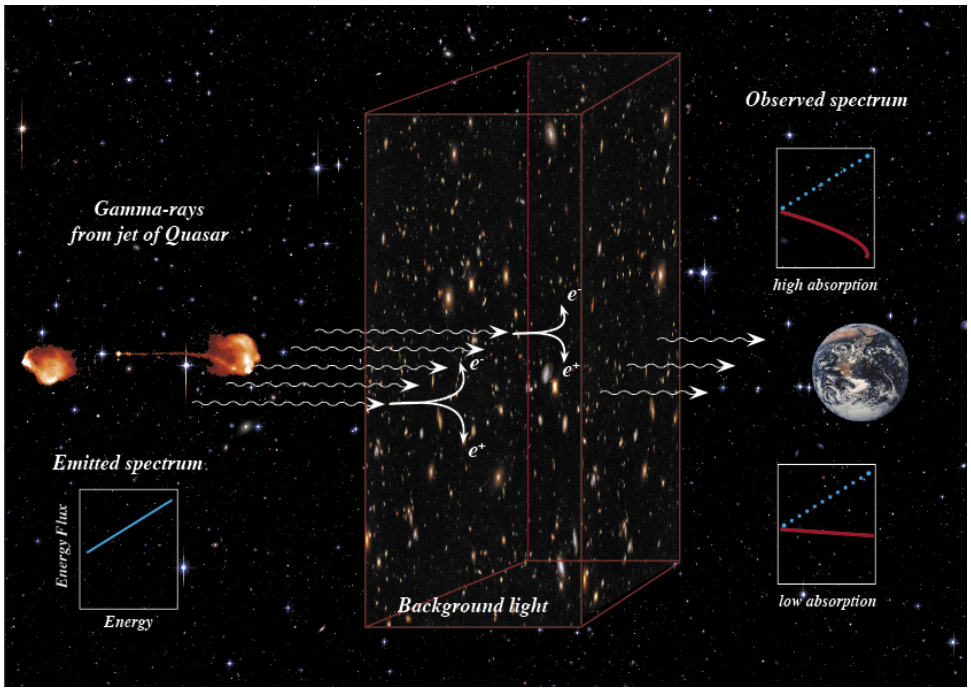

Figure 1.9: Schematic view of the propagation process of γ rays from active galaxies through the extra-galactic background radiation. Image credit: HESS Collaboration.

energetic budget of the Universe. It is a fundamental tool to study and understand, for example, the star and galaxy formation and evolution, the contribution of the obscuring dust, the cosmological parameters, and the high-energy-astrophysics phenomena. However, direct measurements of the EBL are difficult, mainly due to the strong foreground contribution from the zodiacal light and the light from stars in our Galaxy.

HSP objects provide us with an indirect method for investigating the EBL properties. VHE photons produced by HSP blazars interact with the EBL photons via the pair production process $\gamma_{VHE}\gamma_{EBL} \rightarrow e^+e^-$ (Gould & Schréder 1967; Huan et al. 2011) and as a consequence, the observed VHE emission spectra of blazars appear softer than the intrinsic one. Therefore, by assuming a theoretical limit on the hardness of the intrinsic spectrum, it is possible to determine a limit on the

maximum level of EBL absorption and to obtain information on its density (e.g., Orr et al. 2011). This process is depicted in Fig. 1.9.

It is worth mentioning, that TeV γ rays produced by HSP blazars can also be used to probe the intergalactic magnetic field (IGMF). This can be done by exploiting the fact that the positrons and electrons, produced by the interaction of TeV photons with the EBL, are deflected by the IGMF and can inverse-Compton scatter the photons of the CMB and EBL up to GeV energies. These secondary high energy photons produce a halo around the central source, whose angular size directly depends on the IGMF strength (Taylor et al. 2011).

Chapter 2

Physical and geometrical properties of sources in relativistic motion

When a source is in motion with respect to the observer frame, it is necessary to consider some relevant geometric properties. In particular, for a source in relativistic motion it is important to take into account some effects provided by the Theory of Relativity to properly interpret the physical scenario.

A fundamental role is played by the Doppler effect, which can intensify or dim the value of some physical parameters, depending on whether the source is approaching or receding. For an approaching source the intensity of the radiation appears amplified, the variability appears faster and the polarization is higher. On the other hand, for a receding source the brightness could be so attenuated that becomes undetectable. This is the case of blazars, with their relativistic jets closely aligned with the line of sight: only the approaching jet is detected, while the receding one (also known as counter-jet) usually is not visible.

2.1 Doppler boosting

In this section, we investigate the effects of the relativistic motion on some fundamental physical parameters, by considering a source (e.g. a jet), which is approaching in the observer direction, forming an angle θ with respect to the line of sight, at a speed $v = \beta c$. The frequency at which the radiation is emitted is indicated as ν_e.

In the observer frame, the frequency ν_e needs to be corrected for the relativistic Doppler effect:

$$\nu_o = \frac{\nu_e}{\gamma(1 - \beta\cos\theta)} = \delta\nu_e \tag{2.1}$$

The factor:

$$\delta = \frac{1}{\gamma(1 - \beta\cos\theta)}. \tag{2.2}$$

is called *relativistic Doppler factor*, where γ is the Lorentz factor defined as $\gamma = (1 - \beta^2)^{-\frac{1}{2}})$.

When the source is approaching, i.e. $\beta > 0 \Rightarrow (1 - \beta\cos\theta) < 1$, the observed frequency (ν_o) appears to be higher (*blueshifted* than ν_e). The opposite effect is observed for $\beta < 0$ (*redshift*).

We adopt the model in which the approaching speed is positive, therefore $\delta > 1$ when $\beta > 0$, and $\nu_o > \nu_e$ for a source moving in the observer direction. If the involved speeds are not relativistic, i.e. $\beta \ll 1$ ($v \ll c$) and $\gamma \sim 1$, the Doppler factor assumes its classic expression $\delta \rightarrow (1 + \beta\cos\theta)$. In Fig. 2.1 it is shown the Doppler factor trend vs. θ for different γ values. It is clear that for $\beta \rightarrow 1$ and $\theta \rightarrow 0$ the Doppler factor can assume high values. Therefore, what we observe and measure could be different from what is the intrinsic value of the source.

To relate the absolute brightness emitted in the source frame (L_{em}) to the one observed in the observer frame (L_{obs}), we must take into account the following relativistic transformations.

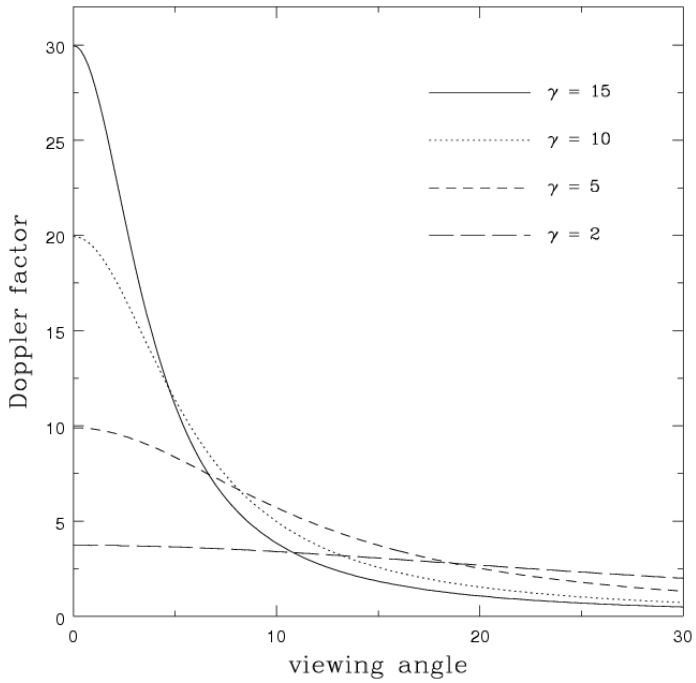

Figure 2.1: Doppler factor trend as a function of the viewing angle. The different curves represent different Lorentz factor γ values, as reported in the top-right corner.

- **Energy transformation.**

  According to Eq. 2.1, in the observer frame the energy of photons will be $h\nu_o = h\delta\nu_e$. For this, L_{obs} differs of a factor δ with respect to L_{em}:

$$L_{obs} \propto \delta \cdot L_{em} \tag{2.3}$$

- **Time transformation.**

  When we consider an approaching source, the time intervals in the observer frame (dt_o) will appear shorter than those measured in the source frame (dt_e). In fact, for the observer $dt_o$is a proper time and it will appear dilated by a factor γ, i.e. $dt_0 = \gamma dt_e$. Furthermore, being the source approaching to the observer, between the first emitted photon and the last one the source moved (approached) of $\gamma v dt_e \cos\theta$ (see Fig. 2.2):

$$dt_0 = \gamma dt_e - \frac{\gamma dt_e v \cos\theta}{c} = \gamma dt_e(1 - \beta\cos\theta) = \frac{dt_e}{\delta} \tag{2.4}$$

  Therefore, there is a further variation of a factor δ for L_{obs} with respect to L_{em}:

$$L_{obs} \propto \delta \cdot L_{em} \tag{2.5}$$

- **Angle transformation**

  We also need to take into account the transformation of the solid angle, centered on the source, from which the observer receives the radiation. Because of the relativistic aberration effect, the solid angle $d\Omega_o$ within which the observer receives the radiation, through a unitary area (supposed to be circular), will differ from the emission solid angle in the source frame $d\Omega_e$:

$$d\Omega_o = \frac{d\Omega_e}{\delta^2} \tag{2.6}$$

  This means that, if the source emits radiation within a solid angle $d\Omega_e$, for the observer it will be concentrated in a solid angle $d\Omega_o$, which is a factor δ^2 smaller. This is called *relativistic beaming* effect. Since we assume that

the emission is isotropic, this implies a variation of a factor δ^2 for L_{obs} with respect to L_{em}:

$$L_{obs} \propto \delta^2 \cdot L_{em} \tag{2.7}$$

By taking into account all the above mentioned effects, we obtain:

$$L_{obs} = \delta^4 \cdot L_{em} \tag{2.8}$$

From Eq. 2.8 it emerges how, for an approaching source approximately moving along the line of sight at a relativistic speed, the brightness can be highly overestimated due to the high value of the Doppler factor (*relativistic boosting* effect).

An important consequence of this effect is the so called *Doppler favoritism*. It is a selection effect for which, for example, faint sources are included in flux-density limited catalogs even if their intrinsic flux density would be too faint to reach the catalog threshold.

When the monochromatic brightness $L_{oss}(\nu_o)$ is considered, i.e. the energy emitted per unit of time in a unitary frequency interval (in erg s^{-1} Hz^{-1} cm^{-2}), we have:

$$L_{obs}(\nu_o)d\nu_0 = L_{em}(\nu_e)d\nu_e \cdot \delta^4 \tag{2.9}$$

and, being $d\nu_0 = d\nu_e \cdot \delta$, we obtain:

$$L_{obs}(\nu_o) = L_{em}(\nu_e) \cdot \delta^3 \tag{2.10}$$

If we deal with a synchrotron spectrum, where $L(\nu) \propto \nu^{-\alpha}$, the previous equation becomes:

$$L_{obs}(\nu_o) = L_{em}(\nu_o) \cdot \delta^{3+\alpha} \tag{2.11}$$

The term $\delta^{3+\alpha}$ can be written as $\delta^4 \cdot \delta^{-(1-\alpha)}$, where the second factor is the *K correction*.

A useful quantity in Astronomy is the *flux density* $S(\nu)$, defined as the amount of energy received per unit of time and frequency interval, through a unitary surface:

$$S(\nu) = \frac{L(\nu)}{4\pi d^2} \tag{2.12}$$

where $L(\nu)$ is the monochromatic luminosity and d is the distance of the source. The flux density is measured in Jansky (Jy)[1] units. This quantity is distance dependent, therefore it does not represent an intrinsic property of the source. For this reason, another quantity often used is the *surface brightness* $B(\nu)$, defined as the ratio between the measured flux density and the solid angle under which the source is seen:

$$B(\nu) = \frac{S(\nu)}{d\Omega} \tag{2.13}$$

Since both the flux density and the solid angle depend on the distance square, their ratio does not depend on the distance.

2.2 Brightness asymmetries

As described in Sect. 1.2, blazars have two relativistic jets ejected from a central and compact region (core) in opposite directions, closely aligned with the line of sight. The approaching jet is called *jet*, while the receding one is called *counter-jet*. By considering that the jet (J) and the counter-jet (cJ) are propagating in opposite directions with respect to the observer frame, they have velocities $+v$ e $-v$, respectively, and their Doppler factors will be:

$$\delta_c = \frac{1}{\gamma(1-\beta\cos\theta)} \;; \qquad \delta_{cJ} = \frac{1}{\gamma(1+\beta\cos\theta)} \tag{2.14}$$

According to Eq. 2.11 the flux density for the approaching jet (S_J) will be higher than the counter-jet flux density (S_{cJ}) by the quantity:

$$\frac{S_J}{S_{cJ}} = R = \left(\frac{1+\beta\cos\theta}{1-\beta\cos\theta}\right)^{3+\alpha} \tag{2.15}$$

However, these considerations are applied to isolated components moving away from the source nucleus. When we consider almost continuous structures, like jet structures, we use the surface brightness B_ν instead of the flux density S_ν. By taking into account that the length of each jet (ℓ) for the observer is $\ell_{oss} =$

[1] 1Jy corresponds to 10^{-26} Watt Hz^{-1} m^{-2}.

$\ell \times \delta$, together with the previous considerations made for the synchrotron emission (§2.1), it is easy to derive that the measured brightness is $\delta^{2+\alpha}$ times higher than that which would be measured if the source was stationary. Therefore, the ratio between the jet (B_J) and the counter-jet (B_{cJ}) brightness, will be:

$$\frac{B_J}{B_{cJ}} = R = \left(\frac{1+\beta\cos\theta}{1-\beta\cos\theta}\right)^{2+\alpha} \tag{2.16}$$

In other words, the jet brightness will be higher than the one of the counter-jet of a factor R. For large values of γ and small angles, R can become so high, that the counter-jet is not detected. Thanks to this effect, by assuming that both the jet and the counter-jet have the same intrinsic power, the knowledge of R allows us to make an estimation of both β and θ. In Chapter 6 we will apply this method to the case of the blazar Mrk 421.

2.3 Brightness temperature

An apparent inconsistency, which can be easily explained within the framework of the above mentioned relativistic effects, is the detection of high energy photons together with high values for the brightness temperatures. According to Eq. 1.2, when the variability timescale τ assumes small values, T_B can easily overcome the critical value of 10^{12} K (see Sect. 1.2.1). However, if we assume that the radiation is moving in the observer direction at a relativistic speed, the variability time scale appears shorter, therefore the size of the emitting region is underestimated. On the other hand, the luminosity appears amplified, therefore the brightness temperature may be overestimated even of several orders of magnitude.

According to Eq. 2.4, the variability time in the observer frame τ_{obs} is related to the intrinsic variability τ_{int} by:

$$\tau_{int} = \tau_{obs} \cdot \delta \tag{2.17}$$

The size r of the emitting region will be:

$$r \lesssim c\tau_{int} = c\tau_{obs} \cdot \delta \tag{2.18}$$

where c is the speed of light. With all these ingredients, we can now relate the intrinsic brightness temperature T_B^{int} to the observed one T_B^{obs}:

$$T_B^{int} \approx T_B^{obs} \cdot \delta^{-(3+\alpha)} \tag{2.19}$$

2.4 Apparent transverse speed

In this section we describe how apparent superluminal motions, often detected in relativistic jets, can be explained in terms of geometrical effects.

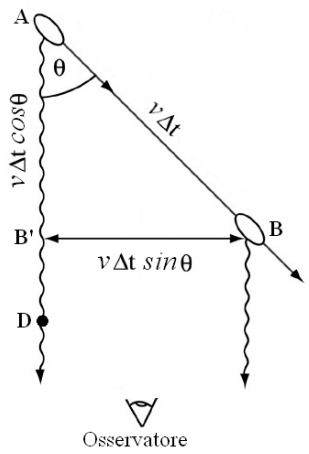

Figure 2.2: Geometrical representation of a source located in A in motion towards B, forming an angle θ with the line of sight.

As illustrated in Fig. 2.2, we consider a source located in A, approaching the observer with a speed v, and forming an angle θ with the line of sight. The source emits photons while it is moving from A to B. When the source emits a photon while it is in B, the radiation emitted when the source was in A has already traveled the distance $AD = c\Delta t$. The time difference (Δt_{app}) in the arrival of the two

photons (the one emitted in A and the one emitted in B) in the observer frame will be:

$$\Delta t_{app} = \frac{AD - AB'}{c} = \frac{c\Delta t - v\Delta t \cos\theta}{c} = \Delta t(1 - \beta\cos\theta) \tag{2.20}$$

where Δt is the interval time in the source frame and $\beta = v/c$. In the observer frame the source apparent transverse speed (v_{app}) will be:

$$v_{app} = \frac{BB'}{\Delta t_{app}} = \frac{v\Delta t \sin\theta}{\Delta t(1 - \beta\cos\theta)} = \frac{v\sin\theta}{1 - \beta\cos\theta}. \tag{2.21}$$

Therefore we have:

$$\beta_{app} = \frac{v_{app}}{c} = \frac{\beta\sin\theta}{1 - \beta\cos\theta} \tag{2.22}$$

For suitable values of β and θ, $\beta_{app} > 1$, and apparent superluminal motions can be detected. In more detail, by making the derivative of Eq. 2.20, we obtain that v_{app} reaches its maximum value (v_{max}) for $\cos\theta = \beta$, and for $sin\theta = \frac{1}{\gamma}$. By replacing these values in Eq. 2.20, we get:

$$v_{max} = \gamma \cdot v \tag{2.23}$$

From Eq. 2.23, it is clear how the v_{app} can appear superluminal when the source is moving at a relativistic speed, in a direction that is close to the line of sight.

Chapter 3

Observing instruments and techniques

3.1 Radio interferometry

The angular resolution of a telescope is defined as the ratio between the observing wavelength and the aperture diameter. Therefore, for a given wavelength, to achieve a higher spatial resolution it is necessary to use a large aperture. At radio frequencies this is a key point, because for increasing the resolution extremely large apertures are required. For example, for a telescope operating in the optical emission band, to achieve an arcsecond resolution an aperture of few meters is required, while to achieve the same resolution at radio wavelengths we need an aperture of several kilometers. Of course, the construction of a radio telescope with such a large aperture is not feasible, mainly because of mechanical and structural problems.

The technique of interferometry help us to overcome this problem. The main idea is to use two or more radio telescopes (radio interferometer), separated by a distance called baseline, which simultaneously collect the electromagnetic radiation, like a diffraction grating. In other words, a radio interferometer represents

a high-resolution single virtual radio telescope with a diameter equivalent to the maximum baseline length.

The voltages, produced in each antenna of a radio interferometer by the incident radio waves, are multiplied and time averaged by a device called correlator, producing the interference pattern. Analytically, an interferometer measures the signal spatial coherence function:

$$V(u,v) = V_0 e^{-i\phi} \propto \int_{-\infty}^{+\infty} \int_{-\infty}^{+\infty} B(x,y) e^{2\pi i(ux+vy)}\, dx\, dy \tag{3.1}$$

where V_0 and ϕ represent the amplitude and the phase terms of this complex function, known as fringe visibility, which is the Fourier inverse transform of the sky brightness distribution $B(x, y)$. The amplitude term gives us information about the source flux density while the phase term gives information about the source structure and position in the sky.

All of the amplitude and phase terms sampled over all baselines form the fringe visibility, which is represented in Cartesian coordinates u (West-East axis) and v (North-South axis). In practice, u and v are the baseline lengths, projected in a plane which is perpendicular to the line of sight, the so called (u, v) plane. The number of antennas of a radio interferometer and their displacement are an essential requirement to obtain a good coverage of the (u, v) plane. A big advantage is provided by the fact that the projected baseline lengths vary with time because of the Earth rotation, increasing the frequency sampling (Earth rotation aperture synthesis).

At present one of the main radio interferometers is the Karl G. Jansky Very Large Array (JVLA) in Socorro (New Mexico, USA), which consists of 27 radio antennas, each one with a diameter of 25 m, spread out along three 21 km arms of a Y-shaped track (see Fig. 3.1). The 27 antennas of the array can be arranged in different configurations with a maximum antenna separation of about 36 km. The JVLA mainly operates in a frequency range ranging from L-band (∼1-2 GHz) to Q-band (∼40-50 GHz), reaching an angular resolution of the order of 0.05 arcsec

Figure 3.1: Overall view of the JVLA radio interferometer. Image courtesy of NRAO/AUI.

at 43 GHz.

During the 90s, one of the most important continuum radio survey at 1.4 GHz was realized by using the JVLA, producing a catalog of sources which covers the sky north of Declination -40° (about 82% of the celestial sphere), known as NRAO VLA Sky Survey (NVSS). The NVSS catalog contains about 2 million discrete sources with a flux density stronger than ~2.5 mJy, with a 45 arcsecond angular resolution.

In the JVLA radio interferometer all antennas are physically connected and this is a limitation for the maximum achievable baseline, which limits the angular resolution. It is possible to extend the radio interferometry technique by simultaneously using radio telescopes situated in very distant regions of the Earth's surface. This technique is known as Very Long Baseline Interferometry (VLBI), and allows us to reach an angular resolution down to sub-milliarcsecond.

At present, one of the largest VLBI array is the Very Long Baseline Array (VLBA, Fig. 3.2), situated in USA, consisting of 10 identical radio antennas, each one with a diameter of 25 m, with baselines from ~200 km (Los Alamos - Pie Town baseline, with both stations situated in New Mexico) up to ~8600 km (Mauna kea, Hawaii - St. Croix, Virgin Islands baseline). The VLBA operates in

Figure 3.2: Representation of the VLBA telescopes. Image courtesy of NRAO/AUI.

a frequency range from 1.2 GHz) to 86 GHz, reaching an angular resolution of the order of 0.12 milliarcsec at 86 GHz.

Othe major VLBI arrays are the European VLBI Network (EVN), with stations in Europe, Asia, South Africa and Arecibo, and the Long Baseline Array (LBA) in the southern hemisphere.

To obtain an even higher angular resolution, a radio telescope in Earth orbit can be used, providing greatly extended baselines (Space VLBI). At present the Russian satellite RadioAstron is orbiting around Earth and together with some of the largest ground-based radio telescopes form baseline extending up to 350,000 km.

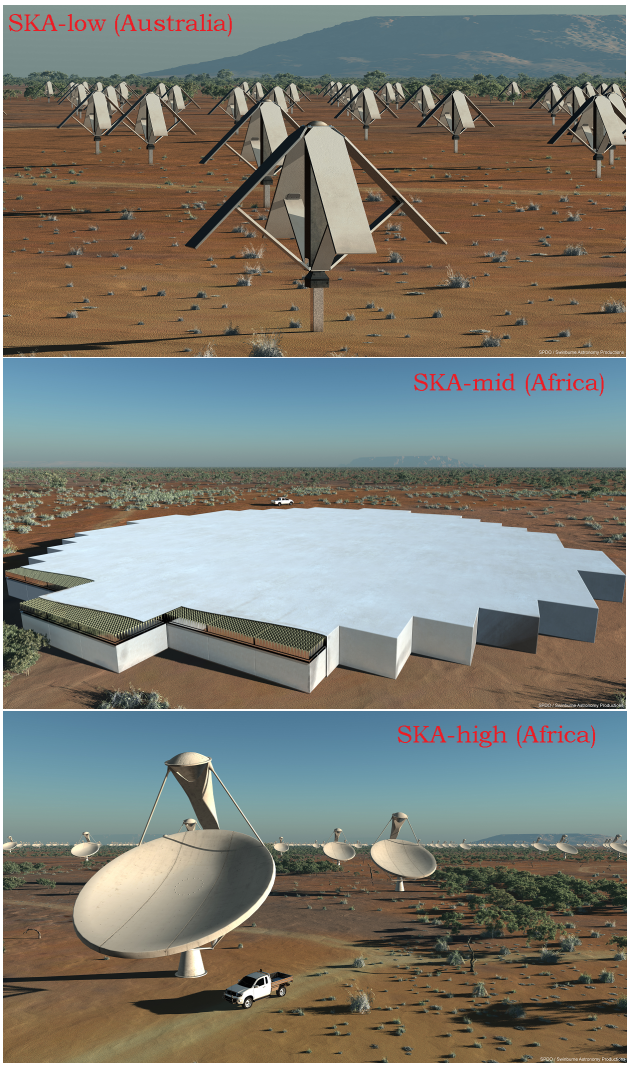

Figure 3.3: Artist impression of the low-frequency sparse aperture array to be built in Australia (upper panel), of the mid-frequency (middle panel) and high-frequency (lower panel) arrays, to be built in Africa.

3.2 Towards the future: Square kilometer Array

The Square Kilometer Array (SKA) is a new generation revolutionary aperture synthesis radio telescope, that will combine signals from a network of antennas distributed over more than 3000 kilometers, producing a radio telescope with a collecting surface up to one square km and a very large field of view.

Ten countries (Australia, Canada, China, India, Italy, New Zealand, South Africa, Sweden, the Netherlands and the United Kingdom) are full members of the SKA international organization and around 100 organizations in about 20 countries are collaborating for the scientific and technical development of the project.

The SKA will operate over a frequency range from 70 MHz up to 25 GHz, divided into three frequency bands: low-band from 70 to 300 MHz, mid-band from 0.3 to 10 GHz, and high-band from 10 to 25 GHz. The sensitivity improvement will be of about two orders of magnitude (reaching the μJy level) with respect to the current radio telescopes, and the expected survey speed improvement will be of about 4 orders of magnitude. A key feature of the SKA telescope is the capability to simultaneously observe multiple sky regions, by means of multiple independent beams, by increasing the telescope survey speed. The multi-beam capability will also increase the total field of view, which, at frequencies below 1 GHz, will reach several tens of square degrees. For all of these reasons, the SKA project will develop innovative technology for receiving systems, signal transport and computing. The SKA is a very ambitious and demanding project that will provide the development of new technologies, e.g. large field of view, multi-beam, high speed in data acquisition, computation, and a strong industrial return.

SKA will help astronomers to address numerous and fundamental astrophysical questions such as the origin and evolution of the Universe, the formation and evolution of black holes, galaxies and large-scale structures, the origin of magnetic fields and the nature of the dark energy. All of the main astrophysical topics investigated by SKA are represented by five key science projects: Galaxy Evo-

lution, Cosmology and Dark Energy; Probing the Dark Ages; The Origin and Evolution of Cosmic Magnetism; Strong Field Tests of Gravity Using Pulsars and Black Holes; The Cradle of Life.

The two sites chosen for hosting SKA are the Western Australia's Murchison Shire (hosting the low frequency array) and the South Africa's Karoo region (hosting the mid and high frequency dishes), which, being among the most remote regions on Earth, are suitable for radio observations thanks to very low radio frequency interferences (RFI). The realization and the development of the SKA project is organized into two main phases, expected to be accomplished between 2018 and the late 2020s. For the phase 1, the low-frequency instrument, consisting of sparse aperture arrays with more than 500 stations, will be built in the Australian site (SKA1-low), while the mid-frequency instrument, possibly operating at frequencies up to 20 GHz, will be built in the African site with an array of 200 dishes (SKA1-mid). With the phase 2 there will be the full realization of the telescope arrays in both sites, with one million of low frequency antennas and about 2000 high and mid frequency dishes. The design of the SKA low, mid and high-frequency arrays is shown in Fig. 3.3.

The VLBI capability of SKA can be implemented at the early stages with the SKA1-mid, by including it within the existing VLBI networks (SKA-VLBI). With a sensitivity down to μJy and an angular resolution down to the milliarcsecond, the SKA-VLBI will be an ideal tool, for example, for studying low luminosity AGNs and it will allow us to shed light on the details about the physics of the jet formation and the relation with the accretion processes. Thanks to the high-resolution SKA-VLBI polarimetric observations it will be possible to investigate the magnetic field structure close to the jet base, which is crucial for understanding the jet launch mechanisms and the related processes (Blandford & Payne 1982). Both as a stand-alone interferometer and as a VLBI sensitive element, SKA1 will have a fundamental impact on the study of AGNs in synergy with high energy observations (Agudo et al. 2015; Giroletti et al. 2015; Paragi et al. 2015).

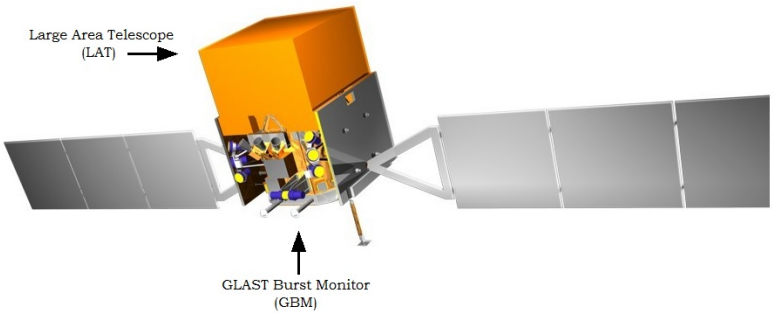

Figure 3.4: *Fermi* satellite sketch, with the LAT (top yellow area) and the GLAST (bottom) instruments.

3.3 The *Fermi* satellite

The *Fermi* Gamma-ray Space Telescope was launched on June 11, 2008 on an elliptical orbit at an altitude of about 565 km, with an inclination of 25.6° with respect to the Earth's equator (Atwood et al. 2009). *Fermi* is the successor of the Energetic Gamma Ray Experiment Telescope (EGRET), on board the Compton Gamma Ray observatory (CGRO), which operated from 1991 to 2000 (Thompson et al. 1993). The *Fermi* satellite was intended and designed to mainly operate in survey mode. It covers the full orbit in about 96 min, and every ~3 hours (two orbits) it scans the entire sky.

On board the *Fermi* satellite there are two scientific instruments: the Large Area Telescope (LAT) and the Gamma-ray Burst Monitor (GBM, Fig. 3.4). The LAT is the primary instrument. It is a pair conversion telescope which detects γ rays in the energy range between ~20 MeV and ~300 GeV, with a field of view of 2.4 sr, and an angular resolution[1] $< 0.15°$ for $E > 10$ GeV (Atwood et al. 2009). As illustrated in Fig. 3.5, the *Fermi*-LAT is made by a 4×4 array of towers, consisting of a tracker, in which γ rays are converted into charged pairs electron/positron, and a segmented calorimeter, which measures the electron-positron pairs energy.

[1] Single photon angular resolution (on-axis, 68% space angle containment radius) for $E > 10$ GeV.

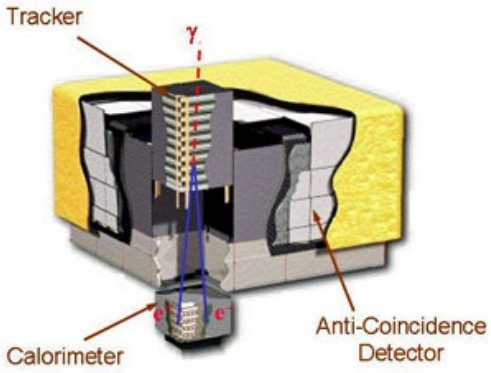

Figure 3.5: Cutaway of the *Fermi*-LAT.

The external surface of the tracker detector is fully covered by an anti-coincidence detector, which allows the instrument to reject the charged particle background. By combining the information from the anti-coincidence detector, the tracker and the calorimeter, it is possible to estimate the direction and the energy of the γ rays. Additional technical details can be found in Atwood et al. (2009) and Ackermann et al. (2012a).

The secondary instrument, the GBM, complements the LAT detector and is dedicated to the study of transient phenomena in the energy range between 8 keV and 40 MeV. Occasionally the satellite can move from survey mode into pointing mode to study relevant transient phenomena.

The *Fermi* mission is led by NASA with the collaboration from various institutions in France, Italy, Germany and Japan.

The *Fermi* satellite provides the international community with a unique and precious opportunity to explore and study the high energy phenomena in the Universe and powerful transients as γ-ray bursts, flaring active galactic nuclei, solar flares, pulsars, supernova remnants and binary systems.

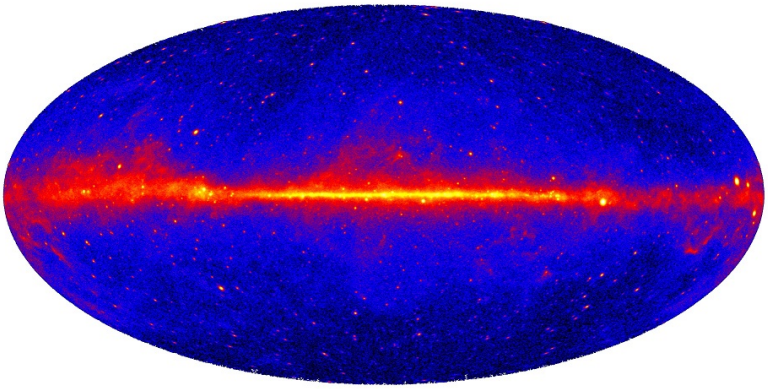

Figure 3.6: All-sky γ-ray view based on five years of *Fermi*-LAT data at energies greater than 1 GeV, in Galactic coordinates. The central horizontal bright band corresponds to the plane of our Galaxy. Brighter colors represent brighter γ-ray sources. Additional details are provided in the text. Image credit: NASA/DOE/Fermi LAT Collaboration.

3.3.1 The γ-ray sky and the *Fermi*-LAT catalogs

In Fig. 3.6 there is a count map of the γ-ray sky at energies above 1 GeV in Galactic coordinates, based on five years of data collected from the *Fermi*-LAT.

The most prominent feature is the horizontal band corresponding to the Galactic plane, which is primarily produced from cosmic-ray particle interactions with the interstellar gas and the diffuse radiation field. Many discrete γ-ray sources (bright spots) are detected in all directions, and the entire sky is filled by an isotropic background glow from unresolved extragalactic sources. An interesting and unexpected feature is the presence of two large hard spectrum emission lobes extending for about 50° above and below the Galactic Center direction, called *Fermi* bubbles. These structures may represent a huge reservoir of energetic particles, whose origin is still debated (see e.g. Ackermann et al. 2014).

During these years, four main catalogs of bright γ-ray sources detected by the *Fermi*-LAT were released: the bright source list catalog (0FGL), the *Fermi*-LAT

Table 3.1: The four main catalogs of bright γ-ray sources detected by the *Fermi*-LAT.

Catalog	Obs. time	Number of sources	Ref.
0FGL	3 months	205	Abdo et al. (2009b)
1FGL	11 months	1451	Abdo et al. (2010b)
2FGL	2 years	1873	Nolan et al. (2012)
3FGL	4 years	3033	Acero et al. (2015)

first source catalog (1FGL), the *Fermi*-LAT second source catalog (2FGL), the *Fermi*-LAT third source catalog (3FGL). Details about the total observing time, the number of sources and the references for each catalog are given in Table 3.1.

In each catalog the number of sources progressively increases. This is mainly do to greater amount of data and to analysis improvements: the procedure for source detection, the calibrations at the event reconstruction level and the model for Galactic diffuse γ-ray emission.

The nature of the objects detected by the *Fermi*-LAT was already clear from the 0FGL catalog. If we exclude the *Fermi* sources which do not have any obvious counterparts at other wavelengths (unassociated γ-ray sources, hereafter UGS), the vast majority (>90%) of γ-ray sources are identified or statistically associated with blazars. The Galactic population is primarily made of pulsars, supernova remnants, high mass X-rays binaries, globular clusters and the Galactic center.

Being AGNs the primary population of *Fermi*-LAT sources, four dedicated LAT AGN Catalogs (LAC) were released, associated to the four FGL catalog, respectively: LBAS (106 sources, Abdo et al. 2009a), 1LAC (709 sources, Abdo et al. 2010c), 2LAC (1017 sources, Ackermann et al. 2011b), 3LAC (1591 sources, Ackermann et al. 2015). For example, of the 2192 LAT sources with $b > 10^{\circ}$ in the 3FGL, 1563 are classified as AGNs and are included in the 3LAC. The vast majority (98%) of these 1563 3LAC sources consist of blazars or blazar candidates.

It is interesting to note that, while most of *Fermi*-LAT sources have been ob-

served at different wavelengths, a non negligible fraction of them (about 1/3 of the 3FGL sources) do not have any clear counterpart at lower frequencies. For this reason, various works and observing campaigns were dedicated to develop new methods and to search for new low-frequency counterparts for the UGS detected by *Fermi* (e.g. Massaro et al. 2013a, 2014; Landi et al. 2015; Schinzel et al. 2015).

Chapter 4

VLBA observations of *Fermi*-LAT sources above 10 GeV

The first *Fermi*-LAT catalog of sources above 10 GeV (1FHL, Ackermann et al. 2013), based on LAT data accumulated during the first 3 years of the mission, is providing us for the first time with a large, deep and unbiased sample to gather γ-ray data in the energy range 10-500 GeV. At present, 1FHL represents the best available resource for addressing both the connection between radio and VHE emission and the characterization of the most extreme γ-ray sources.

In this Chapter, we present new VLBA observations of radio sources localized in the sky regions of a subset of 84 1FHL sources in the northern hemisphere. The subset of the 1FHL in the northern hemisphere counts 269 sources, 185 of which have a blazar counterparts which has been observed at high angular resolution. The NVSS flux density distribution at 1.4 GHz for the sources with and without a VLBI observation is shown in Fig. 4.1 and suggests that the sources without a VLBI observation are on average much fainter than the others. This is confirmed by a Kolmogorov-Smirnov (KS) test, which shows that the null hypothesis that the two sets are drawn from the same population has a chance probability as low as 2×10^{-12}. Therefore, completing the observations of the 1FHL sources in the

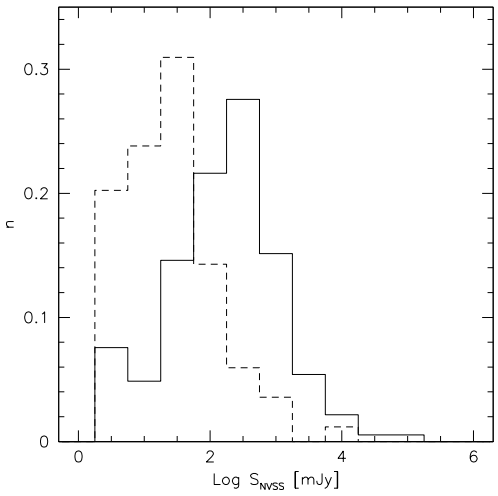

Figure 4.1: Histogram of the NVSS flux density distribution for VLBA observed sources (solid line) and unobserved sources (dashed line) of our sample.

northern hemisphere with the new sources does not only provide a better statistics for the assessment of the properties of this population; it actually allows us to sample and characterize an unexplored region of the parameter space, which is clearly necessary for a proper understanding of the most extreme high energy blazar population.

While the detailed analysis of 1FHL blazars will be the subject of Chapter 5, here we present in details the observations, data analysis, and results obtained for the sources in this peculiar subset.

4.1 The first *Fermi*-LAT catalog of sources above 10 GeV

By using the data collected by *Fermi*-LAT from 2008 August 4 to 2011 August 1, the *Fermi* collaboration produced the first catalog of γ-ray sources detected in the energy range 10-500 GeV.

The catalog contains 514 sources detected with Test Statistic (TS) larger than 25 (significance of $\sim 4\sigma$), of which 449 (about 87%) are associated with known

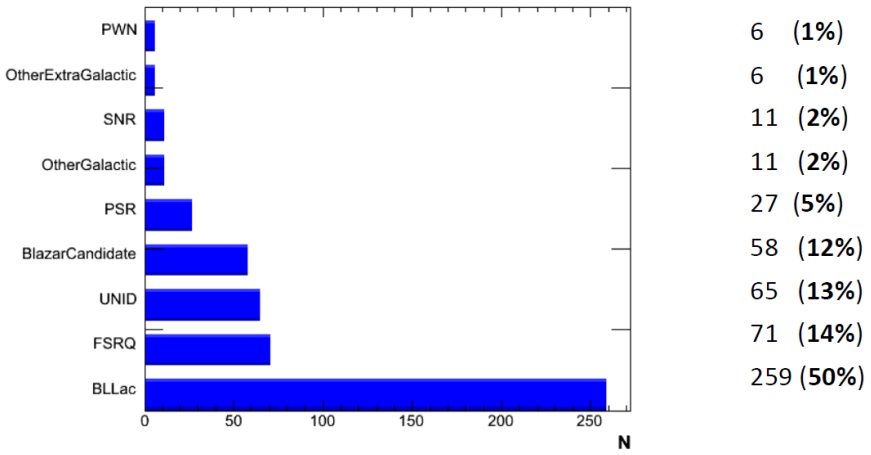

Figure 4.2: Fractional composition of 1FHL objects.

sources, while the remaining objects, about 13%, have no low energy counterparts. In more detail, of the 449 γ-ray sources with an associated counterpart, ~88% (393 sources) are associated with AGNs while the remaining ~ 12% are of Galactic nature.

We note that ~64% (330) of the sources of the entire catalog are associated with blazars (259 BL Lacs and 71 FSRQs), and this is a remarkable feature which indicates that this AGN family dominates the γ-ray sky at E >10 GeV. A detailed report with the fraction of the various 1FHL objects is shown in Fig. 4.2. For each source, the 1FHL catalog reports the location, the energy flux, the spectral and variability properties, and the possible association with objects detected at other frequencies.

The count map of the γ-ray sky at energies above 10 GeV in Galactic coordinates is shown in Fig. 4.3. Along the Galactic equator there is a bright band due to diffuse γ-ray emission originating from the interaction of cosmic rays with interstellar gas and diffuse radiation field. Point sources are present throughout the sky. We also observe an isotropic background and the so-called *Fermi* bubbles are visible below and above the Galactic center.

In Fig. 4.4 the source positions of the whole 1FHL sample, in Galactic coordi-

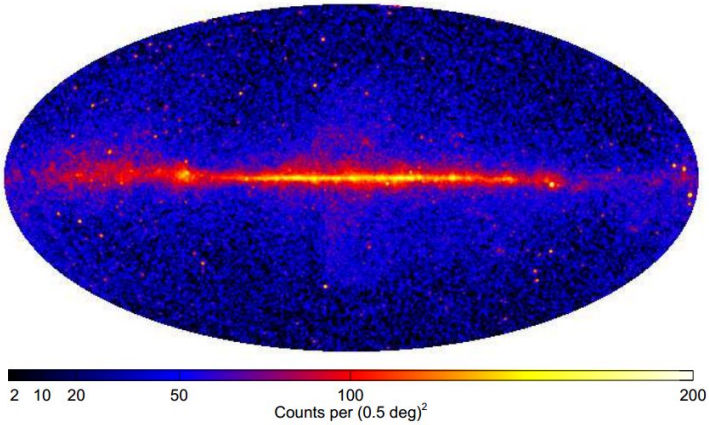

Figure 4.3: All-sky γ-ray view based on three years of *Fermi*-LAT data at energies greater than 10 GeV, in Galactic coordinates. Image credit: NASA/DOE/*Fermi*LAT Collaboration.

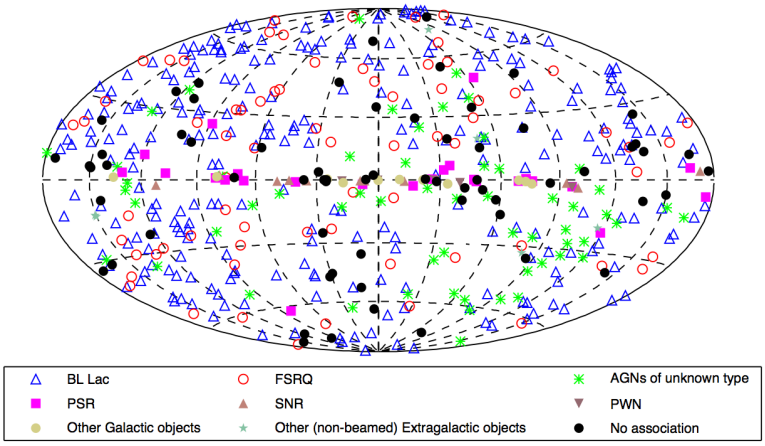

Figure 4.4: Localization in the sky of 1FHL sources belonging to different classes, in Galactic coordinates. Image credit: NASA/DOE/*Fermi*LAT Collaboration.

nates, are depicted. Blazars (blue triangles and red circles represent BL Lacs and FSRQs, respectively) and AGNs of unknown type (green asterisks) are roughly uniformly distributed outside the Galactic plane. The Galactic sources, apart from some pulsars, are concentrated along the Galactic plane. UGS show a fairly uniform distribution outside the Galactic plane; they are also present at low-latitudes, and a large fraction of them are expected to be pulsars, pulsar wind nebulae (PWNe) and supernova remnants (SNRs).

In the whole 1FHL sample there are 63 sources (39 UGS, 9 blazars, 8 blazar candidates, 4 supernova remnants, 2 pulsar wind nebulae and 1 star forming region) which do not have any association with the sources of the previous 2FGL catalog (Nolan et al. 2012), which was realized from the analysis of two years of survey data in the 100 MeV-300 GeV energy range. Among the whole 1FHL sample, these sources not included in the 2FGL, have the lowest photon fluxes, the hardest photon indexes and most of them are located outside the Galactic plane. As argued by Ackermann et al. (2013), these 63 sources are thought to be blazars with hard spectrum and weak emission, which were more active during the third year of the *Fermi*-LAT activity. This is confirmed by the fact that $\sim 76\%$ of the 1FHL sources not included in the 2FGL catalog were later included in the 3FGL catalog (Acero et al. 2015).

In Fig. 4.5 we show the distribution of the photon fluxes (upper panel) and of the photon indexes (lower panel) for the various classes of the 1FHL sources: extragalactic (red solid line), Galactic (blue solid line) and unassociated (green dashed line) sources. While there is no significant difference for the distribution of the spectral indexes among the various classes, the measured photon fluxes for the Galactic sources tend to be greater with respect to the extragalactic ones. In the upper panel of Fig. 4.5 we see that the lowest values for the photon fluxes are reached by UGS or sources associated with extragalactic objects. This difference does not reflect an intrinsic feature of the Galactic sources, but it arises from the fact that in the Galactic plane there is a worse photon flux sensitivity due to the

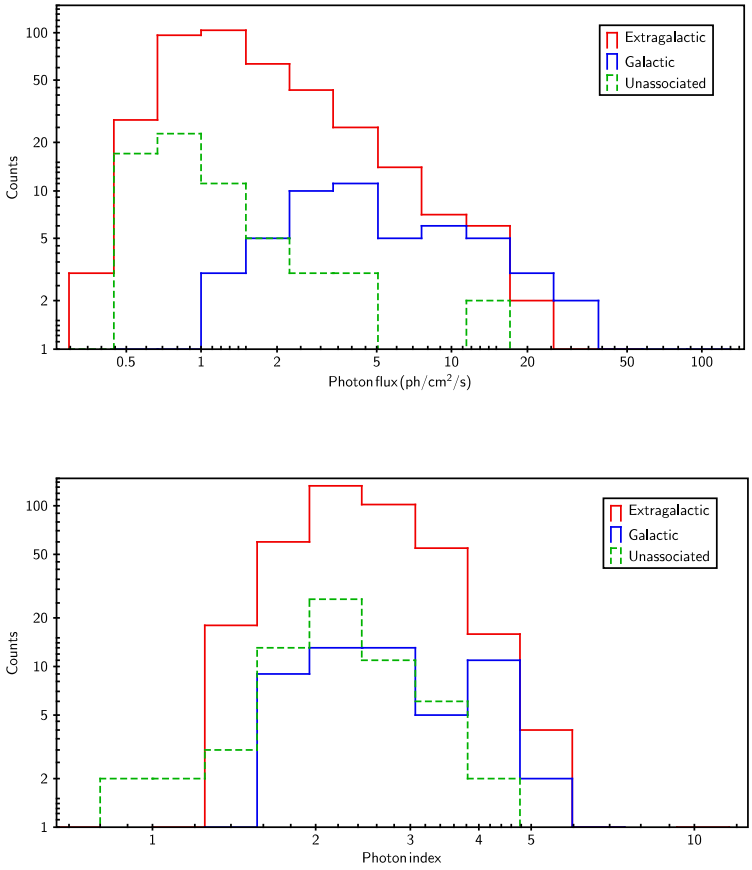

Figure 4.5: Distribution of the photon fluxes (upper panel) and photon indexes (lower panel) for the various classes of the 1FHL sources: extragalactic (red line), Galactic (blue line) and unassociated (green line) sources.

brighter diffuse background.

4.2 Sample selection

From the whole 1FHL catalog, we extracted a sample of 269 sources in the northern sky with a radio counterpart in the NVSS within the 95% confidence radius (r95). If we consider the well known targets, such as Mrk 421 and Mrk 501, and a large number of less studied sources that have been targeted by other projects[1], VLBA archival observations are already available for 185 sources, while a significant fraction (84/269, i.e. 31%) of sources have never been observed with the VLBA. We focus our attention on these 84 1FHL sources, which completely lack high resolution radio observations.

An important step, on the basis of the analysis and interpretation of the physical properties of γ-ray sources, is the investigation and comparison of the multi-frequency properties for the entire 1FHL catalog. However, such a study cannot be carried out neglecting a significant fraction of the sample.

For this reason we have observed with the VLBA the sky regions of these 84 1FHL sources in the northern sky, with the aim to confirm their low-frequency association and to study their parsec scale properties. In more detail, among the 84 1FHL sources of our sample, 49 (about 58%) are classified as blazars, one (~1%) is a supernova remnant, 13 (~15%) are classified as active galaxies of uncertain type (agu), and the remaining 21 (25%) are unassociated, i.e. they completely lack a statistically reliable low frequency association. For the UGS (~ 25%) we want to investigate their nature, possibly detecting a compact radio source associated with them, and search for new low-frequency counterparts.

The final goal is to increase the size of the population of $E > 10$ GeV sources with high angular resolution observations and explore the existence of a correlation between VLBI and $E > 10$ GeV emission on a sample as large and unbiased

[1] see e.g. `http://astrogeo.org/faps/`

as possible.

Details about the 84 sources of our sample are reported in Table 4.1.

Table 4.1: Observational details of the sources in our sample. Col. 1: 1FHL name; Col. 2: low frequency association; Col. 3: source classification: bzb = blazar of the BL Lac type, bzq = blazar of the FSRQ type, agu = active galaxy of uncertain type, snr = Supernova remnant; Cols. 4 and 5: pointing coordinates; Cols. 6 and 7: R.A. and Dec. shift from the phase tracking center; Col. 8: redshift; Col. 9: detection; Col. 10: Experiment code.

IFHL name[a]	Assoc	Class	R.A. h:m:s	Dec d:m:s.	Shift R.A. mas	Shift Dec mas	z	Detection	Exp. code
J0007.7+4709*	MG4 J000800+4712	bzb	00:07:45.22	+47:11:31.0	-	-	0.28	N	S6340A
J0009.2+5032	NVSS J000922+503028	bzb	00:09:22.53	+50:30:28.9	-2190.5	52.0	-	Y	S6340A
J0037.8+1238	NVSS J003750+123818	bzb	00:37:50.85	+12:38:18.8	-443.0	-1079.5	0.09	Y	S6340A
J0040.3+4049	1ES 0037+405	bzb	00:40:13.50	+40:50:05.4	-	-	-	N	S6340B
J0043.7+3425	GB6 J0043+3426	bzq	00:43:48.86	+34:26:26.3	210.0	206.5	0.97	Y	S6340A
J0053.9+4030*	Unassociated	-	00:53:31.76	+40:27:21.5	-	-	-	N	S6340B
J0103.4+5336	1RXS J010325.9+533721	agu	01:03:26.08	+53:37:12.1	1085.0	-1179.0	-	Y	S6340B
J0122.7+3425*	1ES 0120+340	bzb	01:22:38.81	+34:26:11.3	-	-	0.27	N	S6340B
J0131.3+6121	1RXS J013106.4+612035	agu	01:31:07.16	+61:20:33.0	-478.5	-368.0	-	Y	S6340B
J0134.4+2643	1RXS J013427.2+263846	agu	01:34:27.99	+26:38:42.5	-2759.0	-525.0	-	Y	S6340B
J0153.1+7515	BZB J0153+7517	bzb	01:53:07.26	+75:17:44.2	-459.5	1268.0	-	Y	S6340B
J0213.1+2246	MG3 J021252+2246	bzb	02:12:52.78	+22:44:55.1	-752.0	2858.0	0.46	Y	S6340B
J0241.3+6548*	NVSS J024121+654311	agu	02:41:26.41	+65:45:47.7	-	-	-	N	S6340B
J0307.4+4915	Unassociated	-	03:07:27.06	+49:15:10.3	246.0	546.0	-	Y	S6340B
J0322.1+2337	MG3 J032201+2336	bzb	03:22:00.05	+23:36:10.0	1093.5	-1205.5	-	Y	S6340B
J0332.1+6307	Unassociated	-	03:31:53.76	+63:08:14.3	-1056.5	139.0	-	Y	S6340A
J0333.6+2918	TXS 0330+291	bzb	03:33:49.02	+29:16:31.6	214.0	51.0	-	Y	S6340A
J0334.0+6539	TXS 0329+654	bzb	03:33:56.74	+65:36:56.2	1.0	-1.5	-	Y	S6340A
J0338.4+1304	Unassociated	-	03:38:29.30	+13:02:15.0	305.0	-449.0	-	Y	S6340A
J0425.3+6320	Unassociated	-	04:25:24.77	+63:20:05.6	-	-	-	N	S6340B
J0425.4+5601	Unassociated	-	04:26:04.31	+56:03:39.6	-	-	-	N	S6340B
J0432.2+5555*	Unassociated	-	04:32:02.39	+55:48:44.2	-	-	-	N	S6340B
J0515.9+1528	GB6 J0515+1527	bzb	05:15:47.41	+15:27:16.9	820.0	307.5	-	Y	S6340C
J0516.4+7351	GB6 J0516+7350	bzb	05:16:31.12	+73:51:08.8	-469.0	140.0	0.25	Y	S6340C
J0529.0+0937	GB6 J0529+0934	agu	05:29:02.57	+09:34:32.5	-	-	-	N	S6340C
J0540.5+5822	GB6 J0540+5823	bzb	05:40:29.97	+58:23:39.5	-309.0	1048.0	-	Y	S6340C
J0601.0+3838	Unassociated	-	06:01:02.90	+38:38:28.8	362.0	-370.5	-	Y	S6340C
J0605.0+0001	GB6 J0604+0000	agu	06:04:58.43	+00:00:43.1	-	-	-	N	S6340C
J0605.4+2726	Unassociated	-	06:05:01.05	+27:24:56.3	-1216.5	-1138.0	-	Y	S6340C
J0606.6+4742*	CGRaBS J0607+4739	bzb	06:06:38.31	+47:41:47.4	-	-	-	N	S6340C
J0625.9+0002	Unassociated	-	06:26:12.88	+00:03:34.6	-	-	-	N	S6340C

Table 4.1: Continued.

IFHL name[a]	Assoc	Class	R.A.	Dec	Shift R.A.	Shift Dec	z	Detection	Exp. code
			h:m:s	d:m:s.	mas	mas			
J0644.2+6036	Unassociated	-	06:44:35.64	+60:38:49.8	-777.0	-1363.0	-	Y	S6340C
J0648.9+1516	VER J0648+152	bzb	06:48:47.63	+15:16:25.0	-268.5	200.5	0.18	Y	S6340C
J0650.4+2056	Unassociated	-	06:50:35.23	+20:55:56.8	-1715.0	-576.5	-	Y	S6340C
J0706.5+3744	GB6 J0706+3744	bzb	07:06:31.67	+37:44:36.7	-	-	-	N	S6340C
J0743.0+5446*	GB6 J0742+5444	bzq	07:42:46.10	+54:47:06.0	-	-	0.72	N	S6340C
J0745.2+7439	MS 0737.9+7441	bzb	07:44:05.45	+74:33:58.1	298.5	-155.0	0.32	Y	S6340E
J0745.2+8511	NVSS J074715+851208	agu	07:47:15.44	+85:12:08.2	-891.0	-422.0	-	Y	S6340E
J0828.9+0902	Unassociated	-	08:28:47.28	+09:03:37.3	-	-	-	N	S6340D
J0850.0+4849	GB6 J0850+4855	bzb	08:50:26.79	+48:52:00.7	873.1	-71.3	-	Y	S6340G-D
J0912.5+2758*	1RXS J091211.9+275955	bzb	09:12:20.81	+27:55:47.1	-	-	-	N	S6340D
J0930.4+8611	S5 0916+864	bzb	09:29:43.06	+86:12:21.3	-10.5	-18.5	-	Y	S6340E
J0946.2+0106	RXS J094620.5+010459	bzb	09:46:19.81	+01:06:26.1	130.8	-25.2	0.56	Y	S6340G-D
J0959.5+6535	S4 0954+65	bzb	09:59:53.60	+65:34:57.0	-156.4	-518.1	0.37	Y	S6340G-D
J1023.6+2959*	RX J1023.6+3001	bzb	10:23:54.58	+29:58:00.4	-	-	0.43	N	S6340D
J1100.6+4018	RX J1100.3+4019	bzb	11:00:21.09	+40:19:27.7	-	-	0.23	N	S6340D
J1107.5+0223	BZB J1107+0222	bzb	11:07:35.99	+02:22:25.6	1112.5	1004.5	-	Y	S6340D
J1130.4+5814	BZB J1131+5809	bzb	11:31:18.69	+58:08:58.5	444.0	-302.0	0.36	Y	S6340D
J1135.7+6736*	RX J1136.5+6737	bzb	11:35:52.30	+67:37:24.2	-	-	0.13	N	S6340E
J1137.0+2553	RX J1136.8+2551	bzb	11:37:01.13	+25:51:33.8	-1320.5	-1603.5	0.16	Y	S6340G-E
J1212.2+2318	Unassociated	-	12:12:26.70	+23:14:18.9	487.9	-126.9	-	Y	S6340G-E
J1223.3+7953	Unassociated	-	12:23:58.22	+79:53:29.0	377.5	781.0	-	Y	S6340E
J1224.5+2437	MS 1221.8+2452	bzb	12:24:24.20	+24:36:23.6	134.0	60.5	0.22	Y	S6340E
J1244.9+5708	1RXS J124510.5+571020	bzb	12:45:09.99	+57:09:54.4	-0.5	-0.5	-	Y	S6340E
J1249.7+3706	RX J1249.8+3708	bzb	12:49:46.76	+37:07:48.0	140.0	88.0	-	Y	S6340E
J1310.9+0036	RX J1311.1+0035	bzb	13:11:06.42	+00:35:09.8	-841.0	-248.5	-	Y	S6340E
J1315.0+2346	TXS 1312+240	bzb	13:14:43.81	+23:48:26.8	0.0	0.5	-	Y	S6340D
J1322.9+2942*	4C +29.48	agu	13:23:02.59	+29:41:33.4	-	-	-	N	S6340D
J1406.4+1646	Unassociated	-	14:06:14.40	+16:46:35.0	-	-	-	N	S6340E
J1418.6+2539	BZB J1417+2543	bzb	14:17:56.27	+25:43:23.1	-	-	0.24	N	S6340D
J1419.0+7730*	1RXS J141901.8+773229	agu	14:19:41.54	+77:34:43.6	-	-	-	N	S6340E
J1548.3+1455	NON assoc	-	15:48:24.34	+14:57:02.9	-669.5	184.5	-	Y	S6340D
J1619.8+7540	Unassociated	-	16:19:13.77	+75:37:53.8	100.0	347.5	-	Y	S6340E
J1631.0+5224	TXS 1629+524	bzb	16:30:43.12	+52:21:38.7	-261.5	105.5	-	Y	S6340D
J1735.9+2033*	NVSS J173605+203301	bzb	17:35:41.48	+20:35:08.8	-	-	-	N	S6340F
J1744.2+1938*	1ES 1741+196	bzb	17:44:15.87	+19:39:02.1	-	-	0.08	N	S6340F
J1809.3+2040	RX J1809.3+2041	bzb	18:09:25.48	+20:41:31.0	394.0	101.1	-	Y	S6340F
J1841.1+2914*	Unassociated	-	18:41:20.50	+29:11:28.5	-	-	-	N	S6340F
J1841.8+3219	RX J1841.7+3218	bzb	18:41:47.17	+32:18:38.6	1625.5	-555.0	-	Y	S6340F
J1911.0+0905*	SNR G043.3-00.2	snr	19:11:03.97	+09:05:02.5	-	-	-	N	S6340F
J1926.9+6153	1RXS J192649.5+615445	bzb	19:26:49.95	+61:54:41.4	414.0	-946.5	-	Y	S6340F

Table 4.1: Continued.

IFHL name[a]	Assoc	Class	R.A.	Dec	Shift R.A.	Shift Dec	z	Detection	Exp. code
			h:m:s	d:m:s.	mas	mas			
J1942.8+1034	1RXS J194246.3+103339	agu	19:42:47.48	+10:33:27.8	-60.0	698.5	-	Y	S6340F
J2002.6+6303	Unassociated	-	20:02:44.96	+63:02:30.8	-	-	-	N	S6340F
J2004.7+7003*	Unassociated	-	20:04:41.67	+70:06:16.8	-	-	-	N	S6340F
J2015.8+3710*	VER J2016+372	bzq	20:15:53.68	+37:11:30.2	-	-	0.86	N	S6340F
J2031.4+1941*	RX J2030.8+1935	agu	20:31:40.96	+19:40:34.0	-	-	-	N	S6340F
J2127.8+3614	B2 2125+35	bzb	21:27:43.04	+36:13:05.0	138.5	-736.0	-	Y	S6340F
J2212.5+2803	CRATES J221238+275944	agu	22:12:39.10	+27:59:38.5	0.5	4.5	-	Y	S6340F
J2223.4+0104	NVSS J222329+010226	bzb	22:23:29.59	+01:02:26.7	286.0	50.0	-	Y	S6340A
J2247.7+4412	NVSS J224753+441317	bzb	22:47:53.10	+44:13:17.0	-1133.0	1604.0	-	Y	S6340A
J2308.1+1459*	MG1 J230734+1449	bzb	23:07:59.07	+14:58:58.4	-	-	0.50	N	S6340A
J2314.0+1446	RGB J2313+147	bzb	23:13:57.27	+14:44:22.7	-918.5	-355.0	0.16	Y	S6340A
J2329.1+3754	NVSS J232914+375414	bzb	23:29:14.25	+37:54:14.9	-206.5	417.5	0.26	Y	S6340A
J2347.2+0707*	CRATES J234639+07050	agu	23:47:06.48	+07:03:51.9	-	-	-	N	S6340A

[a] With asterisks we indicate the 21 sources excluded from the analysis because of wrong pointing or failed multiple phase center correlation.

4.2.1 Observations and data reduction

We performed the observations with the VLBA between 2013 September 30 and December 7. We divided the sample into six observing blocks (Table 4.2). The observations were carried out at a central frequency of 5 GHz in full polarization, with a total bandwidth of 512 MHz divided into eight 32 MHz sub-bands in each polarization, with a recording rate of 2 Gbps. Observations were carried out in phase reference mode, with a duty cycle of 5 minutes (4 min on target and 1 min on calibrator), repeated six times, resulting in a net observing time of $\sim$ 24 minutes per source. The total observing time for this project is 48 hours.

As reported in Table 4.2, during each observing block one antenna did not work properly because of technical problems. Moreover, from mid-September through mid-November 2013, the Kitt Peak (KP) station experienced some tech-

Table 4.2: Observations details.

Observing date	Experiment Code	Stations log[1]
2013 Dec 9	S6340A	No FD
2013 Oct 3	S6340B	No LA
2013 Oct 4	S6340C	No LA
2013 Sep 30	S6340D	No LA
2013 Nov 22	S6340E	No FD
2013 Dec 7	S6340F	No FD

[1] Station codes: FR – Fort Davis, LA – Los Alamos.

nical problems[2], and in some cases it was necessary to flag the data.

Even if the error ellipse at $E > 10\,\mathrm{GeV}$ is smaller than at lower γ-ray energies, it still is much larger than the typical field of view of VLBI observations. In particular, there are 27 sources for which there is not a well identified radio counterpart, but rather a set of a few possible candidates (between 2 and 5). For these sources we planned to exploit the capability of the DiFX correlator (Deller et al. 2011) to correlate the data at multiple phase centers, one for each candidate radio counterpart. Thanks to this feature it is possible to observe all the radio sources within the r95 region with one single pointing.

We carried out a full calibration in AIPS (Greisen 2003) with the following steps: phase calibration by applying ionospheric and Earth orientation parameters correction; amplitude calibration based on gain curves and measured system temperatures; parallactic angle correction; removal of residual instrumental phase and delay offset by using the pulse-cal tones table; global fringe fitting on all the calibrator sources, and transfer of the solutions to the targets.

After this, we fringe fitted also the phase-calibrated target visibility data, to check for which sources we could expect a detection in the image plane; this was

[2] Additional details about KP technical problems can be found here: `http://www.vla.nrao.edu/astro/archive/issues/`

mainly a "sanity check" and we did not apply the solutions to a CL table. Instead, we split phase-referenced calibrated visibility data, averaging data in frequency within each sub-band but not across IFs, and without any time average (the correlator integration time was 1 second). This provided a nominal field of view of 6.2 arcseconds.

With these single source data sets, we started the editing and imaging process in DIFMAP (Shepherd 1997). Since the phase tracking centers were based on NVSS observations, which for faint sources can be as inaccurate as a few arcseconds, we often had to image wide sky regions before finding a significant source in the image plane. We determined the accurate positions and shift from the phase tracking center for all the detected sources (cols. 6 and 7 in Table 4.1). We then went back to the multi file in AIPS and for each source we corrected the position using the task CLCOR.

After splitting the single sources, we started a final cycle of imaging and self calibration, obtaining the peak flux density, and for each source we determined the deconvolved angular size by using the AIPS task JMFIT.

In particular, for the sources 1FHL J0516.4+7351, 1FHL J2223.4+0104, 1FHL J0338.4+1304, 1FHL J1315.0+2346, 1FHL J1244.9+5708 and 1FHL J1942.8+1034, the calibrators that we chose have some extended structure. For this reason, to have an accurate phase calibration, after the above mentioned calibration procedure, we imaged the calibrator in DIFMAP, producing a model that we use in AIPS for a couple of self-calibration cycles with the task CALIB. As a double check, for these calibrators we performed a separate fringe-fit on the calibrator itself by using the model produced in DIFMAP, and then we applied the solutions to the related target. For the same reason, also the source 1FHL J0930.4+8611 needed a dedicate calibration. However, in this case, being the target quite strong ($S > 200$ mJy/beam) we performed a global fring-fit on the target source itself.

For 8 sources (1FHL J0122.7+3425, 1FHL J0606.6+4742, 1FHL J0743.0+5446, 1FHL J1322.9+2942, 1FHL J0912.5+2758, 1FHL J1023.6+2959, 1FHL J1135.7+6736,

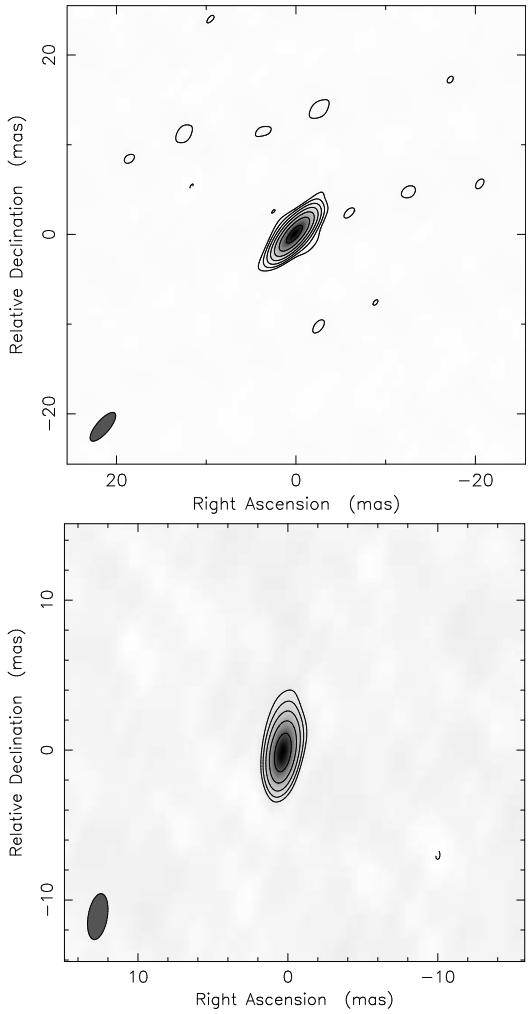

Figure 4.6: 5 GHz VLBA image of the radio counterparts of the γ-ray sources 1FHL J0043.7+3425 (upper panel), classified as a FSRQ, and 1FHL J0648.9+1516 (lower panel), classified as a BL Lac. The beam size is 4.04 mas × 1.47 mas and 3.10 mas × 1.28 mas, respectively. Levels are drawn at $(-1, 1, 2, 4...)\times$ the lowest contour (that is, at 1.3 mJy/beam for the source 1FHL J0043.7+3425 and at 1.5 mJy/beam for the source 1FHL J0648.9+1516) in steps of 2. The noise level is 0.44 mJy/beam and 0.39 mJy/beam, respectively.

Table 4.3: Modelfit details for the extended sources.

1FHL name	Component	S[a]	σ_S	a[b]	b[b]	D_{core}[c]	Orientation[d]
		mJy	mJy	mas	mas	mas	deg
J0338.4+1304	Core	6.33	0.29	0.80	unr	-	-
	C1	3.94	0.29	0.39	unr	1.46	-28.0
J2223.4+0104	Core	6.80	0.24	0.96	0.30	-	-
	C1	3.41	0.13	0.88	unr	1.35	157.4
J1315.0+2346	Core	51.27	0.12	0.22	unr	-	-
	C1	30.57	0.33	1.76	0.72	0.50	-49.1
J1809.3+2040	Core	26.82	0.20	0.67	unr	-	-
	C1	14.48	0.72	5.02	1.46	1.36	-18.7
J1942.8+1034	Core	53.30	0.78	0.73	0.52	-	-
	C1	13.07	0.41	1.06	unr	0.72	89.0

[a] Fitted core flux density at 5 GHz measured in mJy.

[b] *a* and *b* are the full widths at half maximum (FWHM) of the major and minor axes of the elliptical Gaussian component measured in mas.

[c] Distance from the core of the C1 Gaussian component.

[d] Orientation of the extended structure. Angles are measured from North through East.

and 1FHL J1419.0+7730), we pointed the NVSS source which is closer to the 1FHL source centroid, instead of the proposed association in 1FHL. Moreover, for 13 sources the multiple phase center correlation could not be performed because of technical problems that occurred during observations. We exclude these 21 sources from our analysis and they are marked with an asterisk in Table 4.1.

4.3 VLBI properties and detection rate

We detect radio emission on VLBI scales for 51 sources, which corresponds to an overall detection rate of ~81% (51/63). For blazars the detection rate is ~87% (40/46), while for the UGS it is ~65% (11/17). The significance level for

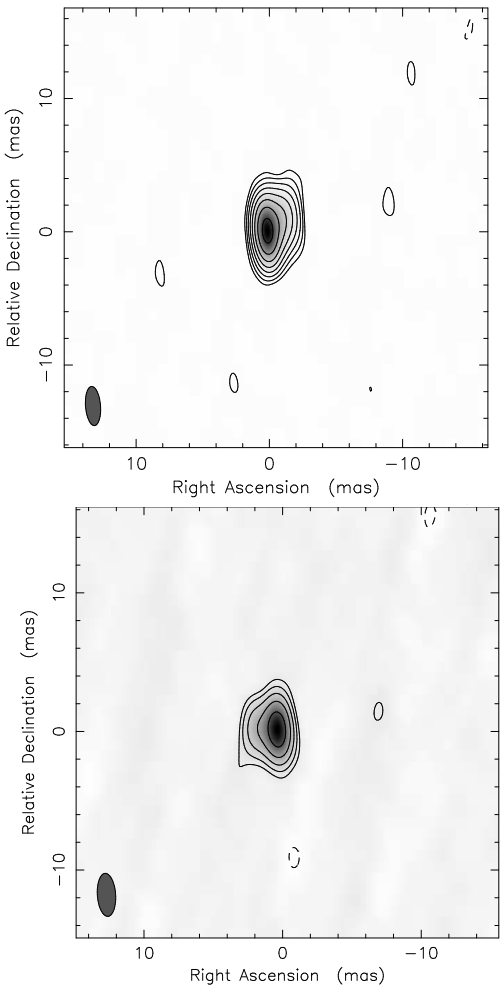

Figure 4.7: 5 GHz VLBA image of the radio counterparts of the γ-ray sources 1FHL J1315.0+2346 (upper panel), classified as a BL Lac, and 1FHL J1942.8+1034 (lower panel), classified as active galaxy of uncertain type. The beam size is 2.95 mas $\times$ 1.13 mas and 3.11 mas $\times$ 1.32 mas, respectively. Levels are drawn at $(-1, 1, 2, 4...)\times$ the lowest contour (that is, at 0.4 mJy/beam for the source 1FHL J1315.0+2346 and at 2.0 mJy/beam for the source 1FHL J1942.8+1034) in steps of 2. The noise level is 0.14 mJy/beam and 0.52 mJy/beam, respectively.

the detection of these sources is always $\gg 5\sigma$. Details about the detected sources are reported in Table 4.4.

Table 4.4: Details about the 51 detected sources. Col. 1: source 1FHL name; Cols. 2 and 3: post-shift VLBI coordinates; Cols. 4 and 5: the 10-500 GeV energy flux of the γ-ray source and the relative 1-sigma uncertainty; Cols. 6 and 7: 1.4 GHz NVSS flux density and the relative uncertainty; Cols. 8 and 9: 5 GHz VLBA peak flux density and the relative uncertainty (calculated by considering a calibration error of about 10% of the flux density and a statistical error provided by the map rms noise); Col. 10: Brightness temperature. For those sources whose radio core is unresolved we calculate lower limits for the brightness temperature.

IFHL name	R.A.	Dec	S_γ	σ_{E_γ}	S_{NVSS}	$\sigma_{S_{NVSS}}$	S_{VLBI}	$\sigma_{S_{VLBI}}$	T_B
	h:m:s	d:m:s	10^{-12} erg/cm^2/s	10^{-12} erg/cm^2/s	mJy	mJy	mJy	mJy	10^9 K
J0009.2+5032	00:09:22.76	50:30:28.85	12.30	3.79	11.8	0.5	5.79	0.59	0.5
J0037.8+1238	00:37:50.88	12:38:19.88	2.07	1.17	75.1	2.3	28.54	2.89	5.8
J0043.7+3425	00:43:48.84	34:26:26.09	7.59	3.33	92.8	2.8	106.0	10.63	80.5
J0103.4+5336	01:03:25.96	53:37:13.28	4.77	1.93	30.4	1.0	27.27	2.74	>1.5
J0131.3+6121	01:31:07.23	61:20:33.37	19.48	5.37	19.1	0.7	6.16	0.63	>0.4
J0134.4+2643	01:34:28.20	26:38:43.01	2.90	1.19	30.1	1.0	11.73	1.20	>0.7
J0153.1+7515	01:53:07.38	75:17:42.93	1.65	1.00	21.2	0.8	6.71	0.69	>0.4
J0213.1+2246	02:12:52.84	22:44:52.24	5.75	3.68	66.9	2.0	63.01	6.30	>5.1
J0307.4+4915	03:07:27.04	49:15:09.75	6.26	3.06	56.0	1.7	300.0	30.04	104.2
J0322.1+2337	03:21:59.97	23:36:11.20	9.14	4.56	76.2	2.3	28.52	2.86	>2.0
J0332.1+6307	03:31:53.92	63:08:14.16	3.24	1.75	42.2	1.3	18.90	1.90	2.4
J0333.6+2918	03:33:49.00	29:16:31.55	5.24	2.13	193.1	5.8	28.33	2.92	>1.7
J0334.0+6539	03:33:56.74	65:36:56.19	8.64	4.22	287.9	8.6	34.33	3.52	5.2
J0338.4+1304	03:38:29.28	13:02:15.45	10.56	5.94	15.1	0.6	6.13	0.64	>0.4
J0515.9+1528	05:15:47.35	15:27:16.59	6.69	3.64	26.5	0.9	31.56	3.31	>2.0
J0516.4+7351	05:16:31.23	73:51:08.66	4.83	3.35	55.5	1.7	8.48	0.86	>0.6
J0540.5+5822	05:40:30.01	58:23:38.45	6.47	3.53	29.3	1.0	11.71	1.18	>0.8
J0601.0+3838	06:01:02.87	38:38:29.17	7.28	5.06	704.0	21.1	62.35	6.24	92.9
J0605.4+2726	06:05:01.14	27:24:57.42	4.56	3.23	23.8	0.8	2.54	0.28	>0.2
J0644.2+6036	06:44:35.75	60:38:51.17	1.93	0.99	33.5	1.1	3.63	0.38	>0.3
J0648.9+1516	06:48:47.65	15:16:24.80	18.42	7.46	64.2	2.0	37.45	3.75	7.8
J0650.4+2056	06:50:35.35	20:55:57.36	4.53	2.86	6.4	0.5	4.62	0.48	>0.3
J0745.2+7439	07:44:05.38	74:33:58.25	3.37	1.88	22.6	0.8	16.28	1.63	>1.2
J0745.2+8511	07:47:16.15	85:12:08.62	5.12	3.00	11.3	0.6	5.03	0.51	>0.3
J0850.0+4849	08:50:00.44	48:54:58.60	3.15	1.92	91.6	2.8	16.11	1.62	>3
J0930.4+8611	09:29:43.07	86:12:21.30	3.33	1.87	142.3	4.3	263.0	26.31	69.3
J0946.2+0106	09:46:24.47	01:05:59.90	2.24	1.28	14.5	0.6	7.57	0.77	0.8
J0959.5+6535	09:58:47.22	65:33:54.30	3.12	2.08	729.4	21.9	95.61	9.57	8.8

Table 4.4: Continued.

IFHL name	R.A.	Dec	S_γ	σ_{E_γ}	S_{NVSS}	$\sigma_{S_{NVSS}}$	S_{VLBI}	$\sigma_{S_{VLBI}}$	T_B
	h:m:s	d:m:s	10^{-12} erg/cm^2/s	10^{-12} erg/cm^2/s	mJy	mJy	mJy	mJy	10^9 K
J1107.5+0223	11:07:35.92	02:22:24.60	2.45	1.30	20.8	0.8	7.95	0.89	>0.6
J1130.4+5814	11:31:18.63	58:08:58.79	1.53	0.95	42.6	1.3	21.22	2.15	>1.5
J1137.0+2553	11:36:50.03	25:50:50.80	7.16	4.82	14.7	0.6	2.20	0.34	>0.8
J1212.2+2318	12:12:38.61	23:11:10.70	1.59	0.79	44.0	1.4	0.34	0.06	>0.03
J1223.3+7953	12:23:58.08	79:53:28.22	2.35	1.43	31.2	1.0	8.93	0.90	>0.6
J1224.5+2437	12:24:24.19	24:36:23.50	11.53	7.03	24.5	0.8	19.53	1.95	8.1
J1244.9+5708	12:45:10.00	57:09:54.38	1.18	0.67	83.3	2.5	66.93	6.69	5.5
J1249.7+3706	12:49:46.75	37:07:47.91	4.38	2.56	5.5	0.5	5.91	0.59	1.2
J1310.9+0036	13:11:06.48	00:35:10.05	3.87	2.19	17.2	0.7	15.71	1.57	3.6
J1315.0+2346	13:14:43.81	23:48:26.78	2.04	0.95	183.7	5.5	60.59	6.06	>3.3
J1548.3+1455	15:48:24.39	14:57:02.72	4.23	1.89	23.9	0.8	17.61	1.92	>1.3
J1619.8+7540	16:19:13.74	75:37:53.45	1.43	0.68	88.1	2.7	15.23	1.53	0.8
J1631.0+5224	16:30:43.15	52:21:38.62	3.11	2.04	120.0	3.6	18.88	1.92	>1.2
J1809.3+2040	18:09:25.45	20:41:30.90	3.30	2.15	51.9	1.6	28.24	2.83	>1.8
J1841.8+3219	18:41:47.04	32:18:39.14	4.63	2.12	20.4	0.7	10.38	1.05	>0.7
J1926.9+6153	19:26:49.89	61:54:42.35	10.46	2.89	22.1	0.8	18.45	1.87	6.8
J1942.8+1034	19:42:47.48	10:33:27.10	20.73	8.06	98.6	3.0	48.56	4.87	8.6
J2127.8+3614	21:27:43.03	36:13:05.74	6.10	2.97	191.2	5.8	38.25	3.85	3.6
J2212.5+2803	22:12:39.10	27:59:38.45	1.88	0.99	144.4	4.3	72.23	7.23	14.1
J2223.4+0104	22:23:29.57	01:02:26.65	1.54	1.13	6.1	0.5	6.29	0.64	1.5
J2247.7+4412	22:47:53.21	44:13:15.40	7.85	4.65	70.6	2.6	28.75	2.97	2.7
J2314.0+1446	23:13:57.33	14:44:23.06	8.75	4.95	40.6	1.3	14.85	1.52	0.7
J2329.1+3754	23:29:14.27	37:54:14.48	8.44	4.25	19.8	0.7	13.19	1.32	3.9

In Fig. 4.6 we show an example of 5 GHz images of the FSRQ source 1FHL J0043.7+3425 (left panel), and the BL Lac source 1FHL J0648.9+1516 (right panel), which are representative of the global dataset. For these two sources, as well as for the vast majority of the detected sources of our sample, for the first time we reveal a VLBI compact structure, and this is confirmed by a visual inspection of the visibility data.

In 5 sources (the unassociated source 1FHL J0338.4+1304, the active galaxy of uncertain type 1FHL J1942.8+1034, and the BL Lac objects 1FHL J2223.4+0104, 1FHL J1315.0+2346, 1FHL J1809.3+2040) we reveal some extended structure close to the compact region. Examples of extended sources are shown in Fig. 4.7. We used the AIPS task JMFIT to fit the brightness distribution of each extended

source in the image plane with two elliptical Gaussian components. Details about model-fit components are reported in Table 4.3.

4.4 Flux density distribution

The distribution of the NVSS flux densities at 1.4 GHz is shown in the top panel of Fig. 4.8 (red solid line), which has a median value of 41 mJy. In the middle panel of Fig. 4.8 we show the 5 GHz VLBA flux density distribution (red solid line), which has a median value of 18 mJy. In both panels we also show the distribution of flux densities for the sources associated with AGNs (green dashed line) and for the unassociated ones (blue dashed line).

In the bottom panel of Fig. 4.8 we show the distribution of the ratio between the 5 GHz VLBI and the 1.4 GHz NVSS flux densities, which peaks at ~0.3, indicating that a fair amount of resolved flux is present.

In particular, we note that for the UGS the median values for both NVSS (33.5 mJy) and VLBI (8.9 mJy) flux densities are lower than for the associated ones (median values of 41.6 and 19.2 for NVSS at 1.4 GHz and VLBI flux densities at 5 GHz, respectively).

By an inspection of both NVSS and VLBI flux densities, it emerges that there are some interesting sources. In some cases ($\sim$ 10%) S_{VLBI} is significantly higher than S_{NVSS}. For example, this is the case of the unassociated source 1FHL J0307.4+4915, with S_{VLBI} = 300.4 ± 30.0 mJy while S_{NVSS} is 56.0 ± 1.7 mJy.

On the other hand, there are sources with NVSS flux densities significantly higher than the VLBI ones. For example, for the sources 1FHL J0333.6+2918, 1FHL J0334.0+6539, 1FHL J0601.0+3838, and 1FHL J2127.8+3614, the ratio S_{VLBI}/S_{NVSS} is between 0.1 and 0.2.

The immediate interpretation is that the sources with $S_{NVSS} \gg S_{VLBI}$ have extended emission, while in the case of $S_{VLBI} \gg S_{NVSS}$ a flare event could be

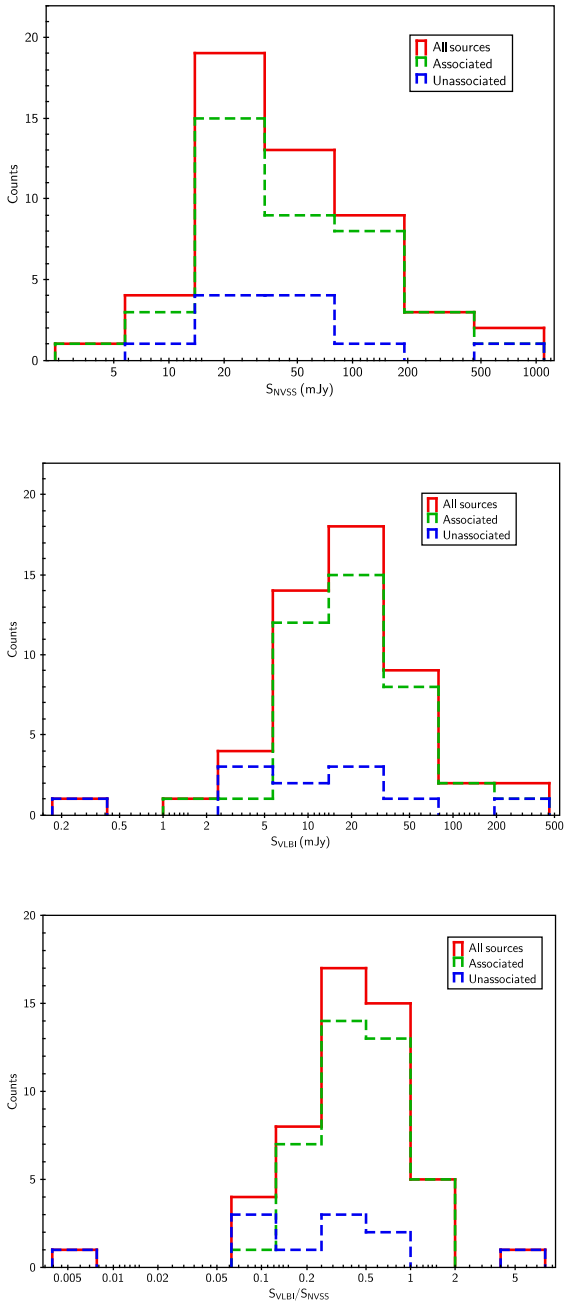

Figure 4.8: Flux density distribution for the detected sources. Top panel: 1.4 GHz NVSS flux density distribution; middle panel: 5 GHz VLBA flux density distribution; bottom panel: distribution of the ratio between the 5 GHz VLBA and the 1.4 GHz NVSS flux densities. Solid red line: all sources; green dashed line: associated sources; blue dashed line: UGS.

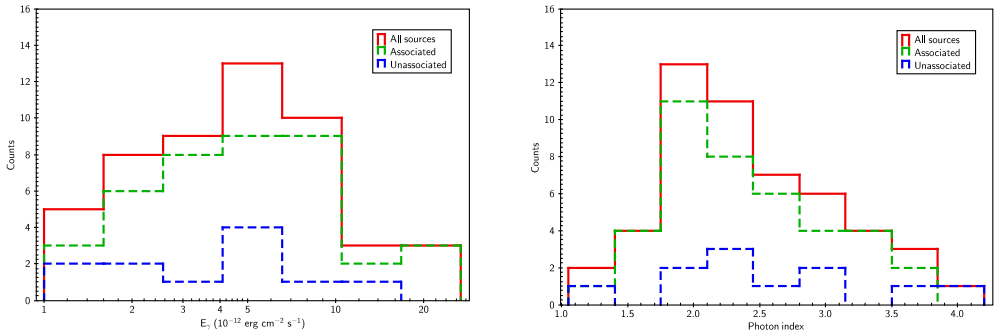

Figure 4.9: Distribution of γ-ray energy flux (left panel) and photon index (right panel) above 10 GeV for the detected sources. Solid red line: all sources; green dashed line: associated sources; blue dashed line: UGS.

responsible of the higher observed VLBI flux density. However, it is important to stress that we are comparing non concurrent observations at different spatial scales and at different frequencies. We note that two of these sources (1FHL J0307.4+4915 and 1FHL J0601.0+3838) are unassociated, and for them we propose a new low-frequency counterpart (see Sect. 4.6).

4.5 High energy properties

The distribution of the γ-ray energy fluxes above 10 GeV for the detected sources are reported in Table 4.4, and in the left panel of Fig. 4.9 (red solid line), showing a median value of 4.6×10^{-12} erg cm^{-2} s^{-1}. In particular, the associated (green dashed lines) and unassociated (blue dashed lines) sources, have median values of 4.8×10^{-12} and 4.2×10^{-12} erg cm^{-2} s^{-1}, respectively.

The photon index distribution is shown in the left panel of Fig. 4.9, and has a median value of 2.31. For the associated (green dashed lines) and unassociated (blue dashed lines) sources, the photon index median value is 2.30 and 2.39, respectively.

4.6 Proposed counterparts for unassociated sources

As previously mentioned in Sect. 4.1, a significant fraction of 1FHL sources ($\sim$ 13%) completely lack a statistically reliable low frequency association, and are classified as unassociateed sources. This is mainly because there are many low-luminosity radio source candidates within the γ-ray source error circle provided by *Fermi* at high energy.

Many efforts were made to find new possible low-frequency associations for the unassociated *Fermi* sources, by using indirect association methods based on the analysis of their MWL properties, such as the investigation of infrared colors (e.g. Massaro et al. 2013a), the low frequency spectral index (e.g. Nori et al. 2014) and the X-ray emission properties (e.g. Landi et al. 2015).

On the other hand, VLBI observations represent a powerful tool for the association of *Fermi* AGNs. The space density of VLBI sources is much lower than that of NVSS sources, so the chance probability of finding a VLBI source within the *Fermi* error ellipse is negligible. Therefore, when we detect parsec-scale emission by means of VLBI observations, we claim an association.

At present, the existing VLBI arrays, due to their small field of view, are not suitable for a "blind" survey of the sky. As a consequence it is not easy to have an immediate validation of the possible counterparts of *Fermi* γ-ray sources. A substantial improvement will be achieved with the advent of SKA, thanks to its large field of view, the multi-beam observing capability, the μJy sensitivity and the availability of many in-beam calibrators.

In the present work, we detect radio emission on VLBI scales for 11 1FHL UGS. Details about the detected UGS are reported in Table 4.5. We note that 7 out of the 11 detected UGS of our sample are also found in the 2FGL catalog (Table 4.5), and they are included in the all-sky radio survey, between 5 and 9 GHz, of sky areas surrounding all the 2FGL UGS by Schinzel et al. (2015). Our proposed low-frequency associations always match with those proposed by Schinzel et al.

Table 4.5: Details about the 11 detected UGS.

1FHL name	2FGL name	NVSS assoc	α[a]	σ_α	Notes
J0307.4+4915	J0307.4+4915	J030727+491510	-0.31	0.31	b,c,d
J0332.1+6307	J0332.1+6309	J033153+630814	-1.03	0.32	b,c,d
J0338.4+1304	J0338.2+1306	J033829+130215	-2.27	0.32	c,d
J0601.0+3838	J0600.9+3839	J060102+383828	-0.16	0.31	b,c,d,f,g
J0605.4+2726	-	J060501+272456	-	-	-
J0644.2+6036	J0644.6+6034	J064435+603849	-3.01	0.32	b,d,e,f
J0650.4+2056	-	J065035+205556	-	-	-
J1212.2+2318	-	J121238+231110	-	-	-
J1223.3+7953	J1223.3+7954	J122358+795329	-0.66	0.32	b,c,d,f,h
J1548.3+1455	J1548.3+1453	J154824+145702	-1.11	0.33	c,f
J1619.8+7540	-	J161913+753753	-	-	-

[a] Spectral index calculated by using the 5 GHz VLBA flux densities of the present work together with the 7 GHz VLBA flus densities provided by Schinzel et al. (2015).

[b] Massaro et al. (2013a).

[c] Massaro et al. (2015).

[d] Schinzel et al. (2015).

[e] Massaro et al. (2013b).

[f] Massaro et al. (2014).

[g] Paggi et al. (2013).

[h] Landi et al. (2015).

(2015) and by using their 7 GHz VLBA observations, together with our 5 GHz VLBA measurements, we compute the spectral index values (Table 4.5).

For these 7 unassociated 1FHL sources included in the 2FGL catalog, our proposed low-frequency counterparts are also supported bycomplementary results from other works which make use of association methods based on the analysis of the MWL properties, such as the investigation of infrared colors and the low frequency spectral index (Massaro et al. 2013a,b, 2014, 2015).

Our proposed counterparts for the sources 1FHL J0644.2+6036, 1FHL J1223.3+7953 and 1FHL J0601.0+3838 are compatible with the X-ray associations proposed by Landi et al. (2015) and Paggi et al. (2013). For the four sources 1FHL J0338.4+1304, 1FHL J0650.4+2056, 1FHL J0601.0+3838 and 1FHL J0332.1+6307 new low-frequency counterparts are now proposed in the 3FGL catalog, and they agree with those proposed in this work. Details about the comparison with other works are reported in Table 4.5.

For the sources 1FHL J0605.4+2726, 1FHL J1619.8+7540 and 1FHL J1212.2+2318 we propose, for the first time, a low-frequency association.

4.7 Brightness temperature

The high resolution of VLBI observations allows a direct measurement of the brightness temperature of a source. However, being blazar jets highly relativistic, and therefore Doppler boosted, it is difficult to measure the intrinsic brightness temperature (T_B^{int}). What we measure is the observed brightness temperature (T_B^{obs}), which is linked to T_B^{int} by the relation $T_B^{obs} = \delta^{3+\alpha} T_B^{int}$, where δ is the Doppler factor and α is the spectral index.

The VLBI core brightness temperature can be used to discern among the physical processes which can occur in the source. In a synchrotron source there are two main physical mechanisms which can limit the intrinsic brightness temperature. One is the IC process which limits T_B^{int} in the range $\sim 5 \times 10^{11} - 1 \times 10^{12}$ K

(Kellermann & Pauliny-Toth 1969). When this limit is exceeded, the IC process leads to rapid and catastrophic electron energy losses. The second relevant physical mechanism is the energy equipartition between particles and magnetic field which limits the T_B^{int} in the range $\sim 5 \times 10^{10} - 1 \times 10^{11}$ K (Readhead 1994).

By performing Gaussian modelfits to the calibrated visibilities, and assuming $\alpha = 0$, we determine T_B^{obs} for each source with the following equation (Piner et al. 1999; Tingay et al. 1998):

$$T_B^{obs} = 1.22 \times 10^{12} \frac{S_{core}(1+z)}{abv^2} \text{ K},$$

where S_{core} corresponds to the fitted core flux density at 5 GHz measured in Jy, a and b are the full widths at half maximum (FWHM) of the major and minor axes of the elliptical Gaussian core component measured in mas, z is the redshift, and ν is the observing frequency in GHz.

For the sources without any redshift estimation we assume $z = 0.2$, which corresponds to the median redshift value of 1FHL BL Lac objects. We note that for some sources the radio core is only slightly resolved or unresolved (i.e. less than half of the beam size). For those sources, we infer upper limits for the size (we use half beam size) and lower limits for T_B^{obs}.

The resulting brightness temperature values are reported in Table 4.4. For those sources whose radio core is resolved, the average T_B^{obs} is of the order of 2 $\times 10^{10}$ K, which is close to the expected value for equipartition.

4.8 Summary

The vast majority of the detected sources of our sample are radio weak (with flux densities of few mJy). For all the detected sources we reveal a VLBI compact component and we confirm their blazar nature. This finding supports the complementary association methods based on the analysis of their MWL properties, such as the investigation of infrared colors, the low frequency spectral index and the

X-ray association (e.g., D'Abrusco et al. 2013; Massaro et al. 2013a; Nori et al. 2014; Landi et al. 2015).

It is interesting to note that we also find a compact component for the UGS. This is a first indication that the nature of the UGS is similar to the associated ones. This hypothesis is mostly supported from the fact that both the 1.4 GHz NVSS and 5 GHz VLBI flux densities for the AGNs and the UGS, shown in Fig. 4.8, are distributed in a similar way. We note that for the UGS both the NVSS and VLBI flux densities are lower than for the associated ones, therefore they may be weaker blazars not yet identified. Moreover, for seven detected UGS we calculated the spectral index values between 5 and 7 GHz VLBA data, which are either flat or inverted, indicating the presence of a self-absorbed region. In particular for the source 1FHL J0644.2+6036 the spectral index is strongly inverted (α=-3.0), exceeding the canonical value of -2.5 for a homogeneous synchrotron emission region. This may be an indication that variability is occurring in this source.

For the 24 sources of our sample whose core is extended, we obtain brightness temperature values of the order of 2×10^{10} K, which is close to the expected value for equipartition. Therefore, what we expect is that the energy is almost equally stored in the magnetic field and in the radiating particles. These values are consistent with the typical HSP blazar T_B^{obs}, and are in agreement with the values obtained in other works (e.g. Piner et al. 2010; Piner & Edwards 2014). From these T_B^{obs} values no high Doppler factors are required and there is no evidence of a strong beaming. However, we note that at 5 GHz we are observing these sources in their self-absorbed part of the synchrotron spectrum, therefore the flux densities and the brightness temperatures are underestimated.

Chapter 5

Correlation analysis for the first *Fermi*-LAT catalog of sources above 10 GeV

5.1 Connection between radio and γ-ray emission in blazars

The vast majority of high energy (HE, $10\,\mathrm{MeV} < E < 100\,\mathrm{GeV}$) and very high energy (VHE, $E > 0.1\,\mathrm{TeV}$) γ-ray sources are associated with radio loud objects, typically blazars. For this reason, the possible correlation between radio and γ-ray emission has produced a great interest, and several works and observing campaigns have tried to address this topic (e.g. Kovalev et al. 2009; Ghirlanda et al. 2010, 2011; Giroletti et al. 2010; Mahony et al. 2010; Ackermann et al. 2011a; Nieppola et al. 2011; Mufakharov et al. 2015). Looking for the presence or not of any correlation between radio and γ-ray emission is a fundamental step to understand the blazar emission processes.

In the MeV/GeV domain, the *Fermi*-LAT has provided a deep, uniform sky survey detecting as many as 3.033 sources in the 3FGL catalog. The results from

Fermi show that both types of blazars are common HE emitters, with FSRQs having softer spectra and being generally more luminous than BL Lacs (see Sect. 1.2).

Moreover, the existence of a highly significant correlation between the radio flux density and the γ-ray energy flux was revealed by Ackermann et al. (2011a), by using both archival 8 GHz data and concurrent 15 GHz observations from the Owens Valley Observatory observing program (Richards et al. 2011) of the AGNs included in the 1FGL catalog. In their work, Ackermann et al. (2011a) find a highly significant positive correlation (with a probability $< 10^{-7}$ for data to be correlated by chance) for both FSRQs and BL Lac objects between radio emission at centimeter wavelength and the broadband γ-ray emission at $E >$100 MeV.

However, while the correlation between radio and γ-ray emission in the energy range 100 MeV - 100 GeV was found with a high significance level, a correlation between radio and VHE γ rays has never been explored. This is mainly due to the lack of a homogeneous coverage of the VHE sky.

VHE observations of blazars are conducted by imaging atmospheric Cherenkov telescopes (IACTs), which detect the Cherenkov radiation from secondary particles in air showers originating when very high energy γ rays strike the atmosphere. The great limitation of the IACT instruments, at present mainly represented by H.E.S.S, MAGIC and VERITAS, is that they operate in pointing mode with a limited sky coverage, and in general they observe sources in a peculiar state. For all these reasons, the current VHE catalogs are strongly biased and no evidence of a correlation between radio and VHE emission has been reported so far.

We note that observations from IACTs detect preferentially BL Lac sources, in particular of the HSP type. Among the 60 currently known TeV blazars included in the online catalog TeVCat[1], which contains all the TeV sources so far detected, about 77% (46 objects) belong to the HSP class[2]. Only five FSRQs are included in TeVCat. The different demographics of the VHE population is explained by

[1] `http://tevcat.uchicago.edu/`

[2] We refer to the catalog version 3.400.

two main factors: FSRQs have intrinsically softer spectra and, being more distant, they undergo a higher EBL attenuation.

The perfect chance to investigate the possible radio-VHE emission connection will be provided by the advent of the new generation Cherenkov Telescope Array (CTA), used in synergy with the SKA. At present, the best available resource for addressing the connection between radio and VHE emission is represented by the 1FHL catalog, which fills the gap existing between the HE and VHE regimes, at present represented by 3FGL and TeVCat, respectively.

5.2 1FHL blazars in the northern hemisphere

The majority of 1FHL sources (393 sources) are associated with AGNs, and ~86% of them are represented by blazars and blazar candidates. In more detail, among the 393 1FHL AGNs there are 259 BL Lacs, 71 FSRQs, 58 active galaxies of uncertain type (agu) and 5 radio galaxies.

We notice that ~ 58% (i.e. 151/259) of BL Lacs and ~ 61% (i.e. 43/71) of FSRQs are found in the northern hemisphere, while ~ 71% (i.e. 41/58) of AGUs are found in the southern hemisphere. This asymmetry in the source count distribution has not a physical origin, but it is rather due to a more sparse optical coverage in the southern hemisphere. Similarly, the fraction of high Galactic latitude ($|b|>10$) UGS is larger (24/38, or ~ 63%) in the southern hemisphere. For this reason, we focus our attention on 1FHL blazars found at Dec>0°, which represent the most significant and unbiased sample. In particular we consider those 1FHL blazars at Dec>0°, for which both arcsecond and milliarcsecond scale structure information is available. For the attended structure we make use of NVSS data (Sect. 3.1), whereas for the high angular resolution we consider our VLBI data (Chapter 4), complemented by archival observations. We obtain a sample of 231 sources (hereafter 1FHL-n) consisting of: 169 BL Lac objects, 44 FSRQs, 15 AGU and 3 radio galaxies.

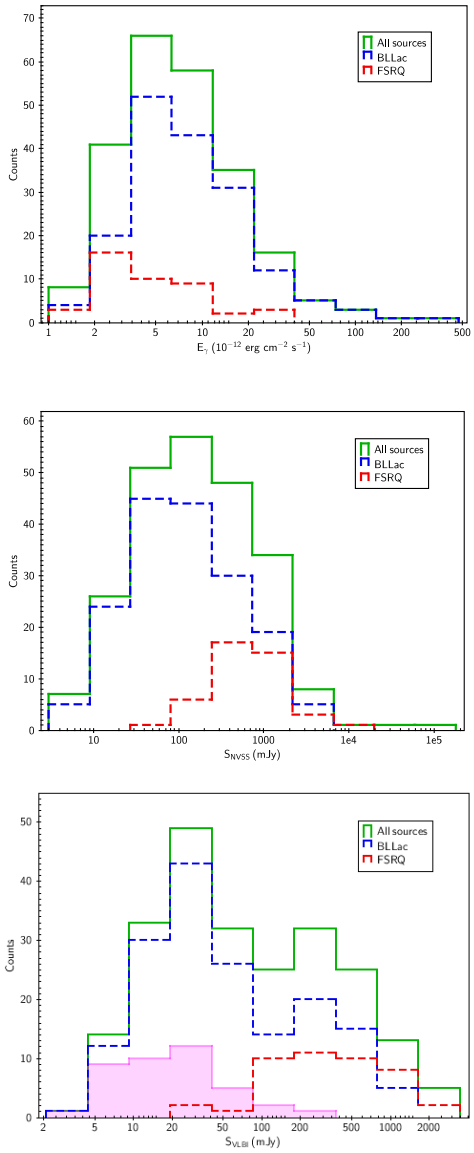

Figure 5.1: Top panel: Distribution of γ-ray energy flux above 10 GeV for 1FHL-n AGNs; middle panel: 1.4 GHz NVSS flux densities distribution; Bottom panel: 5 GHz VLBI flux density distribution; Solid green line: 1FHL AGNs; blue dashed line: BL Lacs; red dashed line: FSRQs. The magenta area in the bottom panel represents the 5 GHz VLBA data of the present work.

Table 5.1: Summary of SED classifications of 1FHL-n AGNs.

Spectral type	Number of sources	Sources with measured redshift
HSP	98	51
ISP	45	20
LSP	58	50
Not classified	30	11
Total	231	132

In addition to the optical classification of blazars, which is based on the presence or absence of emission lines, we also consider the complementary classification based on the spectral energy distribution. The SED classification is possible for 201 sources out of 231, and the dominant class (∼49%, i.e. 98/201), as expected, is represented by blazars of HSP type. In general, HSPs have hard spectra (i.e. with a power-law photon index ≤2), therefore they are expected to emit the highest-energy photons. ISP and LSP are 45 and 58, respectively. The fraction of the various SED classified AGN classes are depicted in Table 5.1.

The distribution of the γ-ray energy flux S_γ above 10 GeV is shown in the top panel of Fig. 5.1 (solid green line), which has a median value of $\sim 6.4 \times 10^{-12}$ erg cm^{-2} s^{-1}. BL Lacs and FSRQs are represented by blue and red dashed line, respectively. S_γ covers about three orders of magnitude (assuming values from 1.1×10^{-12} to 3.2×10^{-10} erg cm^{-2} s^{-1}), and the highest values are reached by BL Lacs.

On the other hand, the 1.4 GHz NVSS flux density distribution is shown in the middle panel of Fig. 5.1 (solid green line), which has a median value of 170 mJy. BL Lacs (blue dashed line) tend to cluster at lower flux density values (median value ∼ 103 mJy) while FSRQs (red dashed line) tend to cluster at higher flux density values (median value ∼ 638 mJy).

In the bottom panel of Fig. 5.1 we show the distribution of the VLBI flux den-

sity. Our VLBA observations described in Chapter 4 provide data for 40 sources. For the remaining sources we use the VLBI flux densities reported in the Radio Fundamental Catalog[3] (RFC). The RFC collects and provides archival VLBI flux densities and positions, in several observing bands, for thousands of compact radio sources, obtained from all available VLBI observations. 5 GHz VLBI data from the RFC are available only for 76 1FHL-n sources, while 8 GHz VLBI data are available for 191 sources. Being the available RFC 5 GHz VLBI flux densities consistent with the 8 GHz ones (their average spectral index is $\sim$ 0.1 and their ratio is $\sim$ 1), we use the 8 GHz dataset for our analysis.

The VLBI flux density distribution (solid green line in the bottom panel of Fig. 5.1) has a median value of $\sim$ 62 mJy. BL Lacs (blue dashed line) and FSRQs (red dashed line) have a median value of $\sim$ 38 and $\sim$ 322 mJy, respectively. In particular, with the magenta color, we indicate the histogram of 5 GHz VLBA flux densities obtained with the present work (Sect. 4.2). It emerges that the 1FHL sources that we targeted and characterized have the faintest radio flux densities, and represent an important extension to an unexplored region of the parameter space. The inclusion of these new flux densities was essential to gather a sample as large and unbiased as possible to explore the possible correlation between VLBI and $E >$10 GeV emission (Sect. 5.3.2).

The distributions of the photon indexes of the 1FHL-n blazar sample are reported in Fig. 5.2 in the energy range 0.1-300 GeV (upper panel), as reported in the 3FGL catalog, and in the energy range 10-500 GeV (lower panel), as reported in the 1FHL catalog. By comparing the two distributions, we note that, in both energy ranges, FSRQs (red solid line) tend to cluster at the softest photon index values while BL Lacs (blue solid line) tend to have the hardest values. The distribution of AGUs photon indexes (green dashed line) covers a wider range of values. in the $E >$ 10 GeV energy range, it extends to hard values, similar to the one of BL Lac objects, suggesting that a considerable fraction of them are likely

[3] `http://astrogeo.org/rfc/`

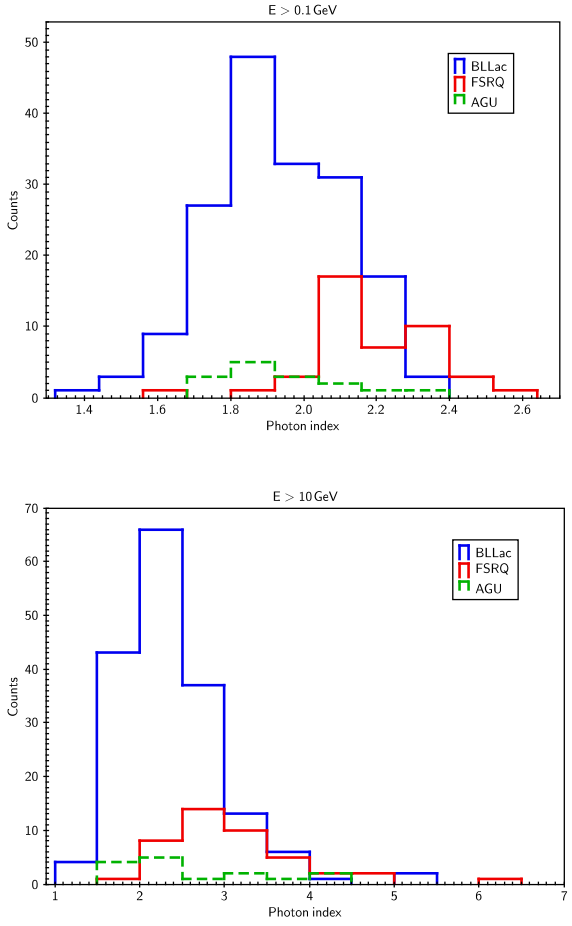

Figure 5.2: Distribution of the photon indexes of the 1FHL-n blazar sample in the energy range 0.1-300 GeV (upper panel), as reported in the 3FGL catalog, and in the energy range 10-500 GeV (lower panel), as reported in the 1FHL catalog. FSRQs and BL Lacs are indicated by red and blue solid lines, while active galaxies of unknown type (AGUs) are indicated by a green dashed line.

BL Lacs. However, the most evident feature which arises is that, when the minimum energy increases from 0.1 to 10 GeV, there is a spectral softening for both FSRQs and BL Lacs. This effect is partly intrinsic, due to internal γ-γ absorption, and partly due to γ-ray attenuation in the optical/UV EBL.

Out of the 231 sources of our sample 132 have known redshifts. In particular we note that, while the fraction of HSP objects with available redshift is ∼52% (51/98), for LSP objects this fraction is ∼86% (50/58). This is because ∼64% (37/58) of LSPs are FSRQs, and they have measured redshift by definition.

Among the 132 sources for which the redshift is available, 44 are FSRQs and 85 are BL Lacs. The redshift distribution of these 44 FSRQs (red line) and 85 BL Lacs (blue line) is shown in the upper panel of Fig. 5.3. The first feature that emerges is that most of the BL Lacs cluster at redshifts lower than 0.5, while FSRQs tend to have redshifts higher than 0.5. The lack of BL Lac objects at high redshifts could mainly be due to the fact that BL Lacs have a fainter intrinsic γ-ray luminosity with respect to FSRQs (see e.g. Abdo et al. 2010a). Moreover, it is important to mention that the redshift distribution of BL Lacs is strongly biased, because of the difficulty in determining their redshifts. While all FSRQs have known redshift, only half of the BL Lacs belonging to the 1FHL sample have measured redshifts.

In the lower panel of Fig. 5.3 is shown the redshift distribution of blazars divided into the various SED classes: HSP (blue line), ISP (green area) and LSP (red line). The distribution of blazars of HSP type peaks at the lowest redshift values.

In Fig. 5.4 is shown the scatter plot of the photon index vs. the redshift for FSRQs (red points) and BL Lacs (blue points), at E >0.1 GeV (top panel) and E >10 GeV (bottom panel). At E >0.1 GeV the spectral shape does not show any evolution (at least within each of the two classes), while at E >10 GeV the photon index has a redshift dependence, with sources getting softer when the redshift increases. While the photon index softening with increasing redshift at E >10 GeV

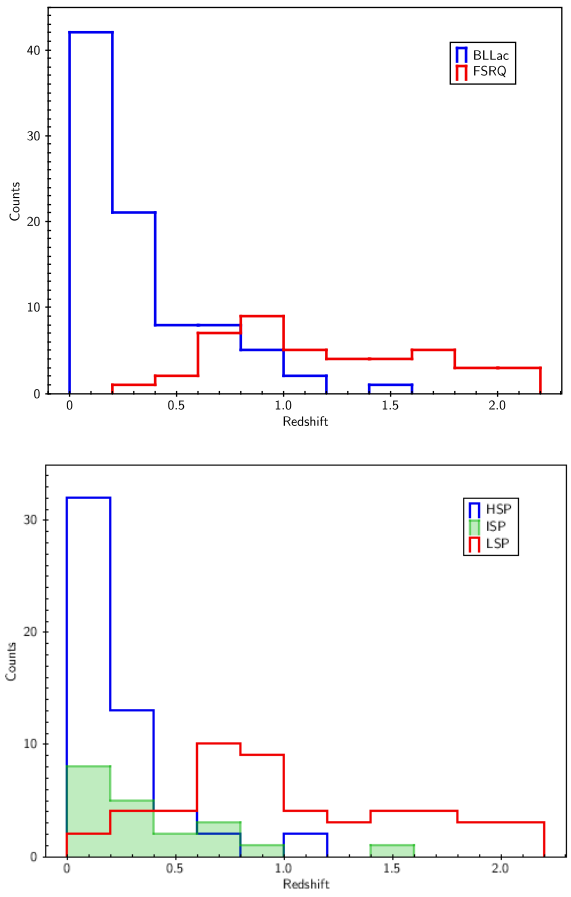

Figure 5.3: Upper panel: redshift distribution of the 44 FSRQs (red line) and the 88 BL Lacs (blue line) belonging to the 1FHL-n sample. Lower panel: redshift distribution of blazars divided in the various SED classes: HSP (blue line), ISP (green area) and LSP (red line).

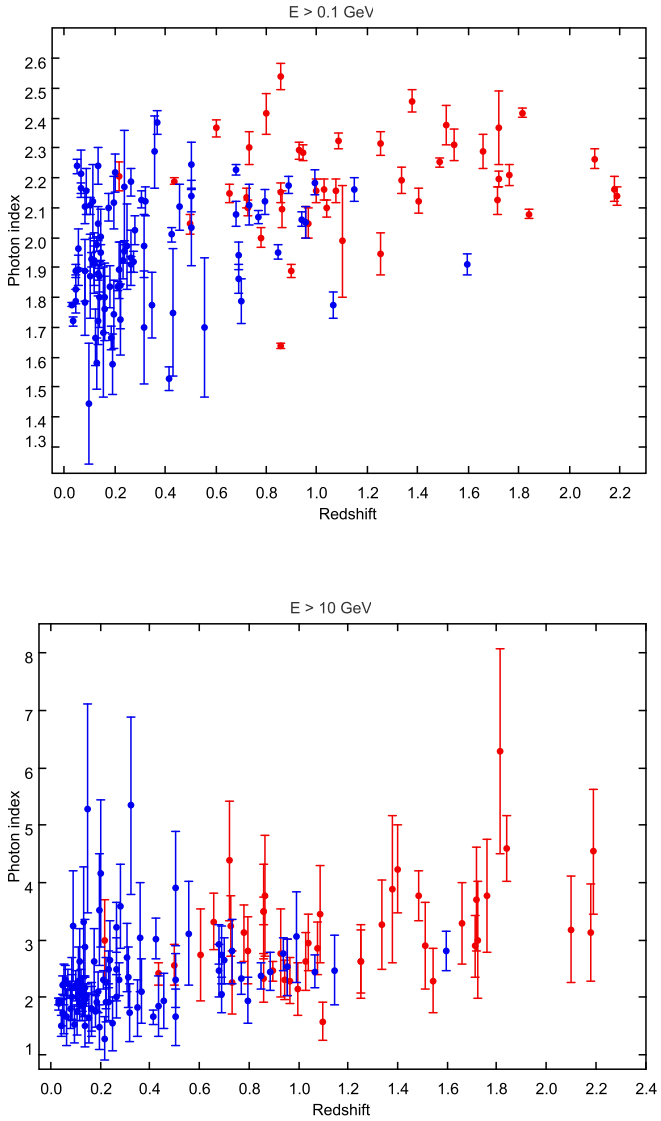

Figure 5.4: Scatter plot of the photon index vs. the redshift for 1FHL-n FSRQs (red points) and BL Lacs (blue points), for which the redshift is available, at E >0.1 GeV (top panel) and E >1 GeV (bottom panel).

is not clearly noticeable for BL Lacs, which cluster at low redshifts ($z < 0.6$), it clearly emerges in the FSRQs sample, extending at redshifts up to 2.5. The main reason for this spectral shape evolution at $E >10$ GeV could be the attenuation of the γ rays in the optical/UV EBL. The attenuation in the EBL is energy dependent and only affects photons with energies above few tens of GeV (Ackermann et al. 2012b). On the other hand, a cosmological evolution of FSRQs may also play a role, introducing an intrinsic spectral softening.

5.3 Correlation analysis between radio and γ-ray emission

By using the sample of 231 1FHL-n AGNs, introduced in the previous section, we investigate the possible existence of a correlation between radio and γ-ray at $E >10$ GeV emission. To quantify the strength of the correlation we use the Pearson product-moment correlation coefficient r:

$$r = \frac{\sum_{i=1}^{N}(X_i - \bar{X})(Y_i - \bar{Y})}{\sqrt{\sum_{i=1}^{N}(X_i - \bar{X})^2 \sum_{i=1}^{N}(Y_i - \bar{Y})^2}} \tag{5.1}$$

where X_i and Y_i represent the logarithmic flux densities for each single source at each frequency.

For this correlation study, at radio frequency we use VLBI flux densities because they are more representative of the innermost source region, where the γ-ray emission is produced. The VLBI flux density vs. 1FHL energy flux scatter plot is shown in Fig. 5.5, in which BL Lacs and FSRQs are indicated with blue and red colors, respectively. From this correlation analysis it emerges a lack of correlation between VLBI flux densities and γ-ray energy fluxes. We obtain $r = 0.05$ for the full sample, while for BL Lacs and FSRQs sub-classes we obtain $r = 0.17$ and $r = -0.02$, respectively.

To avoid artificial correlations introduced by the Malmquist bias, we inves-

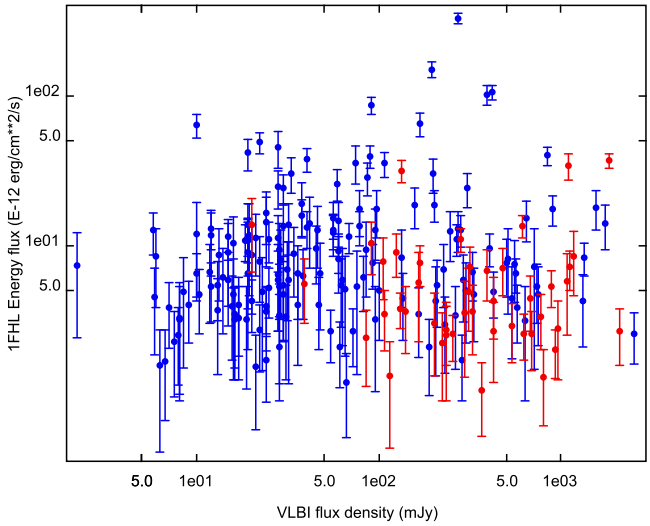

Figure 5.5: VLBI flux density vs. 1FHL energy flux scatter plots for the 1FHL-n sample. BL Lacs and FSRQs are indicated in blue and red colors, respectively.

tigated this possible correlation in the flux-flux plane. In flux-limited samples, most objects tend to concentrate close to the survey sensitivity, and they occupy a well defined and narrow region in the luminosity-luminosity plane, creating a strong bias. On the other hand, this effect cannot be simply removed by looking for any possible correlation in the flux-flux plane, where artificial apparent correlations can be produced because of the effect of a common distance radio and γ-ray luminosity modulation. This effect is particularly important, for example, in samples of sources in which the distance modulation range is large with respect to the luminosity dynamical range.

5.3.1 The method of surrogate data

The investigation of the possible correlation between radio and γ-ray emission is a non trivial task, due to the various observational biases which can apparently enhance or dilute any intrinsic luminosity correlation.

For this reason, Pavlidou et al. (2012) proposed a new statistical method, based on permutations of the observed flux densities, to quantitatively assess the significance of any observed apparent radio/γ-ray correlation in blazars, by tacking into account distance effects.

The null hypothesis that we assume is that the flux densities in the radio and γ-ray emission bands are intrinsically uncorrelated. From a frequentist point of view, by using this method, we want to know how frequently a sample of objects, with the same features of the sample under examination (i.e. with radio and γ-ray luminosities intrinsically uncorrelated and with the same dynamical range and distance effects), produces an apparent correlation as strong as the one observed in the original dataset. To produce simulated samples with the same selection criteria of the sample under examination, we use permutations of measured quantities. To simulate the effect of a common distance for objects with intrinsically uncorrelated luminosities, permutations are performed in the luminosity space, and this represents the novelty of this method, which consists of the following steps:

1. For not introducing artificial biases and to be sure that the simulated samples will have similar luminosity and redshift distributions as the real data, we divide the sample into n redshift bins. The number of bins is determined by imposing the condition that each bin contains at least 10 objects.

2. In each bin we calculate the γ-ray and radio luminosities from the measured flux densities, at a common rest-frame γ-ray and radio frequency.

3. To simulate sources with intrinsically uncorrelated luminosities, we perform permutations of the obtained luminosities. Moreover, if we perform permutations in the luminosity space, the simulated samples maintain the same luminosity dynamical range of the original sample.

4. To avoid the Malmquist bias we now come back to the flux density space. To do this, for each luminosity pair we use a common redshift, which is

randomly selected among the sources in each bin. In this way, we are simulating the common distance effect for the uncorrelated luminosities.

5. At this point, in the flux-density space we reject any pairs for which one of the flux density value falls outside the flux-density dynamical range of the original sample. As shown in Pavlidou et al. (2012) the number of such cases is low and decreases when the number of objects increases, but it is a necessary step to avoid artificial apparent correlations.

6. We now quantify the correlation strength by calculating the Pearson correlation coefficient r (Eq. 5.1).

To quantify the significance of the correlation of the original sample, we repeat the full process for 10^6 times and obtain the distribution of r values for the intrinsically uncorrelated flux densities. The fraction of $\mid r \mid > r_{data}$, where r_{data} is the Pearson correlation coefficient value for the observed quantities, represents the probability to obtain an apparent correlation which is at least as strong as that found in the original sample.

5.3.2 Results

We are now ready to asses the statistical significance of the correlation results between radio VLBI and γ-ray at E >10 GeV emission for 1FHL-n blazars, by using the above mentioned method of surrogate data.

We note that, the method of surrogate data requires the calculation of luminosities. Therefore, we only use sources with known redshifts. As a consequence the number of sources in the sample is reduced and the redshift distribution can be altered. This condition mainly affects the class of BL Lacs: only half of the 1FHL BL Lacs have measured redshifts.

For this reason, we extend our sample by including blazars found at Dec>-40°, for which the redshift and VLBI measurements are available, to obtain a sample

5.3. Correlation analysis between radio and γ-ray emission

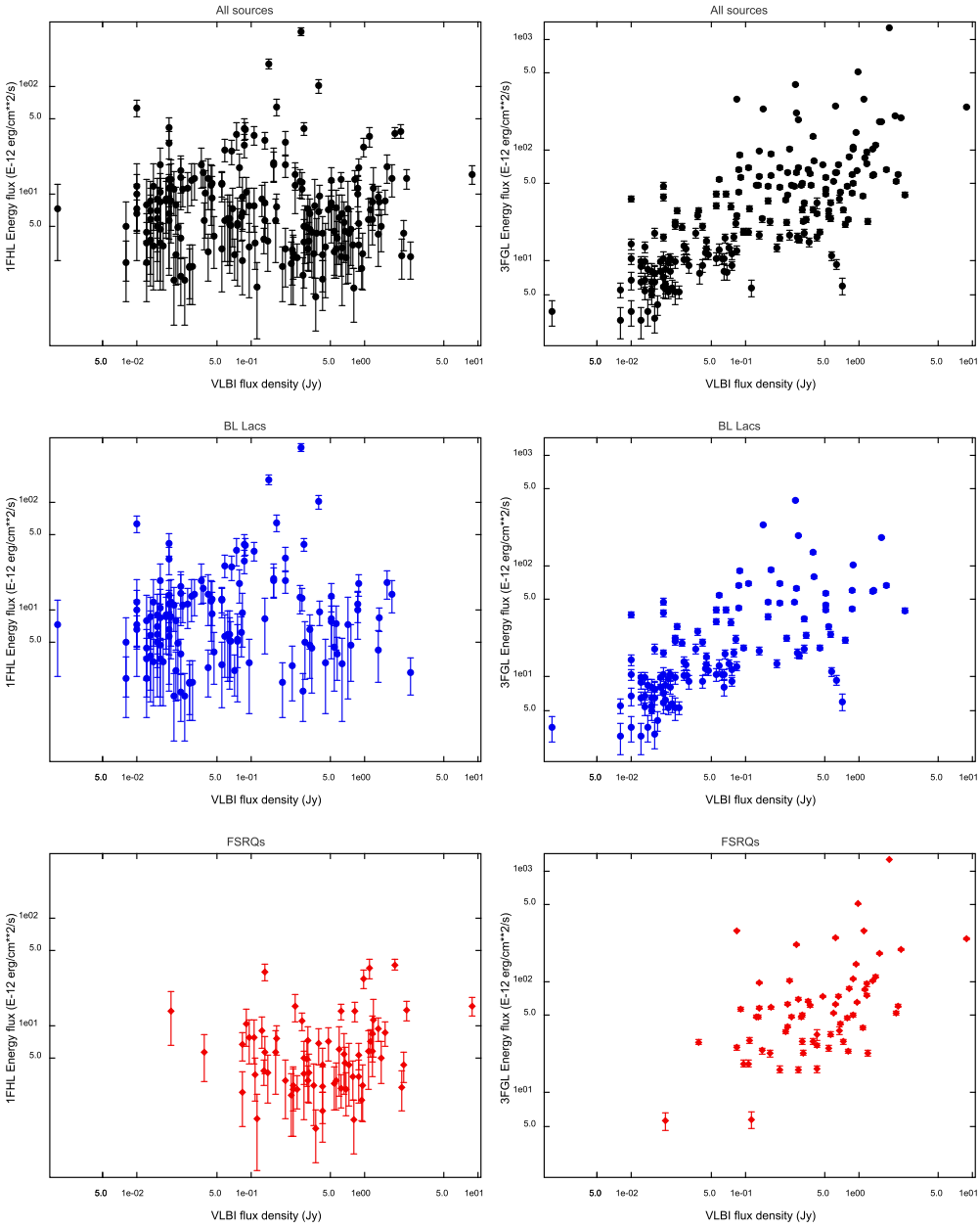

Figure 5.6: VLBI flux density vs. 1FHL (left panel) and 3FGL (right panel) energy flux scatter plots, for the full sample (top frames), BL Lacs (middle frames) and FSRQs (bottom frames).

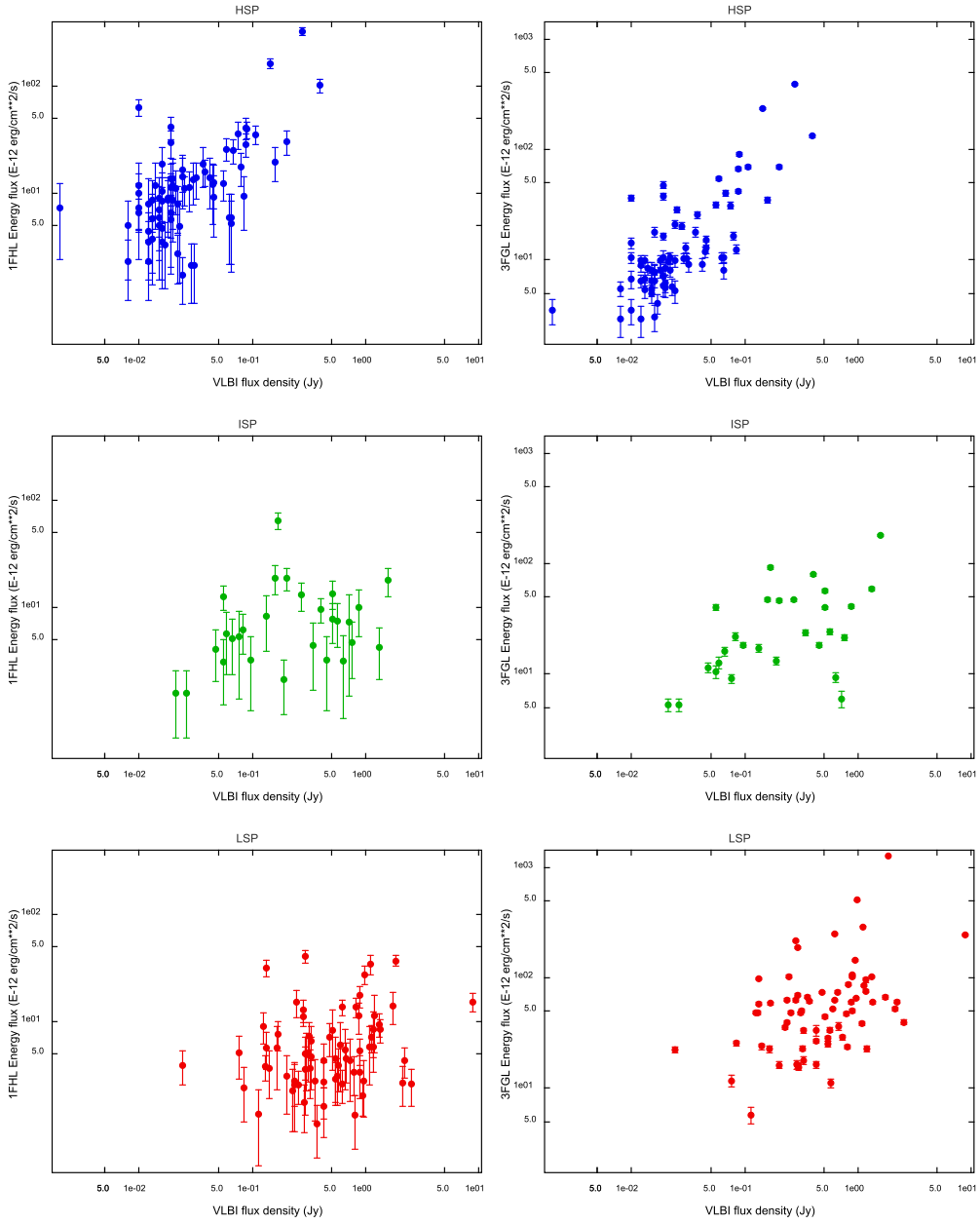

Figure 5.7: VLBI flux density vs. 1FHL (left panel) and 3FGL (right panel) energy flux scatter plots, for the HSP (top frames), ISP (middle frames) and LSP (bottom frames) objects.

as large as possible, without introducing any bias. The resulting sample that we use for the analysis contains 198 1FHL sources. We also investigate the possible correlation for different subsets of blazars, divided according to the optical (BL Lacs and FSRQs) and spectral (HSP, ISP and LSP) classification. For comparison, we perform the same correlation analysis, for all sources of our sample and for the various subsets, by using their 3FGL (0.1-300 GeV) energy fluxes.

In Fig. 5.6 we show the scatter plots of the VLBI flux density vs. 1FHL (left panel) and 3FGL (right panel) energy flux, for the full sample (top frames), BL Lacs (middle frames) and FSRQs (bottom frames). In Fig. 5.7 we show the scatter plots of the VLBI flux density vs. 1FHL (left panel) and 3FGL (right panel) energy flux, for the three different spectral types: HSP (top frames), ISP (middle frames) and LSP (bottom frames).

The results of the correlation analysis are shown in Table 5.2, in which we report the number of sources in each subset, the number of redshift bins (determined by imposing the condition that each bin contains at least 10 objects), the resulting Pearson product-moment correlation coefficient r, and the correlation statistical significance (which represents the probability to obtain a correlation, from intrinsically uncorrelated data, at least as strong as the one observed in the real sample).

Overall, for the sources of 1FHL sample, VLBI flux densities and energy fluxes appear to be uncorrelated: for the full sample we find $r = -0.02$. On the contrary, when we use the 3FGL energy fluxes we find a strong positive correlation ($r = 0.73$) with a high statistical significance (chance probability $< 10^{-6}$).

When we consider BL Lacs and FSRQs separately, for both subsets in the 1FHL energy range (10-500 GeV) we find only a weak correlation with $r = 0.13$, and a chance probability of ~ 0.5. On the other hand, in the 3FGL energy range (0.1-300 GeV) both optical blazar classes show significant correlation (at the $p < 10^{-6}$ level), with BL Lac objects showing a higher correlation coefficient ($r = 0.67$) with respect to FSRQs ($r = 0.52$).

Table 5.2: Results of the correlation analysis between 1FHL (10-500 GeV) energy fluxes and VLBI flux densities for various sub-samples. For comparison the same analysis was performed by using 3FGL (0.1-300 GeV) energy fluxes.

Source type	Catalog	Num. of sources	Num. of z-bins	r-Pearson	Significance
All sources	1FHL	198	18	-0.02	0.8
	3FGL	198	18	0.73	$< 10^{-6}$
BL Lac	1FHL	123	12	0.13	0.5
	3FGL	123	12	0.67	$< 10^{-6}$
FSRQ	1FHL	67	6	0.13	0.4
	3FGL	67	6	0.52	4.5×10^{-5}
HSP	1FHL	75	7	0.60	3.2×10^{-3}
	3FGL	75	7	0.76	2.0×10^{-6}
ISP	1FHL	28	2	0.33	0.1
	3FGL	28	2	0.55	6.3×10^{-3}
LSP	1FHL	70	6	0.23	9.3×10^{-2}
	3FGL	70	6	0.45	1.3×10^{-3}

An interesting behavior for the correlation coefficient is observed when the single spectral blazar sub-classes are considered. The Pearson correlation coefficient increases when the synchrotron peak moves to higher frequencies: LSPs have $r = 0.23$ (chance probability 9.3×10^{-2}), ISPs have $r = 0.33$ (chance probability 0.1) and HSPs have $r = 0.60$ (chance probability 3.2×10^{-3}). The same correlation coefficient trend is observed when 3FGL energy fluxes are considered: $r = 0.45$ for LSP (chance probability 1.3×10^{-3}), $r = 0.55$ for ISP (chance probability 6.3×10^{-3}) and $r = 0.76$ for HSP (chance probability 2.0×10^{-6}).

HSP blazars are therefore the only blazar sub-class for which a significant correlation between VLBI and 1FHL fluxes is found.

5.4 Discussion

In this Chapter, we explored the possible existence of a correlation between radio and hard γ-ray emission for blazars, based on the most complete and unbiased sample available at present. In Fig. 5.8, we show the VLBI flux densities vs. γ-ray energy flux scatter plot for the three spectral types LSP (red squares), ISP (green squares) and HSP (blue squares); in the upper panel, we consider the $E > 10$ GeV (1FHL) γ-ray band and in the lower panel, the $E > 100$ MeV (3FGL) γ-ray band. The results of our statistical analysis can be outlined as follows:

- **1FHL-n sample:** the population of 1FHL blazars does not show any evidence for a correlation between VLBI radio flux density and hard γ-ray energy flux ($r = -0.02$);

- **1FHL-n FSRQs and BL Lacs:** even when considered separately, both the sub-classes of 1FHL-n FSRQs and BL Lacs do not show any evidence for a correlation between VLBI radio flux density and hard γ-ray energy flux ($r = 0.13$ for both types);

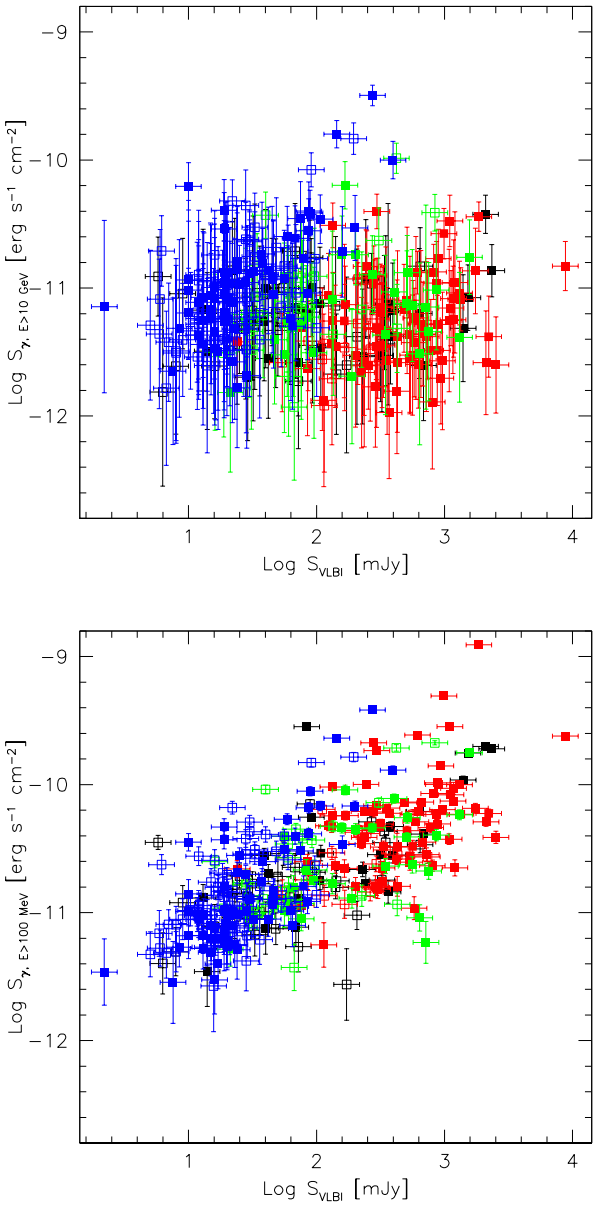

Figure 5.8: VLBI flux density vs. 1FHL (upper panel) and 3FGL (lower panel) energy flux scatter plots for the full sample. HSP, ISP and LSP sub-classes are indicated in blue, green and red colors, respectively The sources for which the spectral classification is not possible are indicated in black color. The filled and empty symbols represents sources with and without redshift, respectively.

- **1FHL-n LSP, ISP, HSP:** when we consider the three SED-type defined blazars, the correlation progressively evolves from weak and not significant for LSP blazars ($r = 0.23$, $p = 0.09$) to strong and significant for HSP blazars ($r = 0.60$, $p = 0.003$);

- **Hard vs. soft γ-ray emission:** the lack of correlation observed between radio and hard γ-ray band emission for the 1FHL-n population, and for most of its subsets (FSRQs, BL Lacs, LSP, and ISP blazars) evolves to a strong and significant correlation when the soft γ-ray band ($E > 0.1$ GeV) is considered ($r_{\mathrm{all,\,3FGL}} = 0.73$, $p_{\mathrm{all,\,3FGL}} < 10^{-6}$);

- **Hard vs. soft γ-ray emission for HSP:** the already strong correlation between VLBI and hard γ-ray band emission for the 1FHL-n HSP blazars improves when the soft γ-ray band ($E > 0.1$ GeV) is considered ($r_{\mathrm{HSP,\,3FGL}} = 0.76$, $p_{\mathrm{HSP,\,3FGL}} = 2 \times 10^{-6}$);

The most interesting results of this work are that **(1) HSP blazars are the only sub-class showing a significant correlation between VLBI radio and hard γ-ray emission** and **(2) the radio-γ ray correlation is found for all classes when soft, instead of hard, γ-ray emission is considered**.

These results may be explained in the framework of blazar SEDs and their interpretation. As discussed in Chapter 1, powerful objects are characterized by soft γ-ray spectra; as shown in Fig. 5.9, the high energy component peak occurs at energies lower than those sampled by the LAT. Moreover, the 1FHL energy range is limited to the highest energies of LAT ($E > 10$ GeV), where the emission has dropped severely. It is worth noting that at high energy, powerful objects show spectral breaks (Finke & Dermer 2010; Harris et al. 2012; Stern & Poutanen 2014) due to severe cooling losses of the emitting particles and $\gamma\gamma$ absorption processes. This applies to FSRQs and BL Lacs of the LSP type. ISP blazars share most of these features, except that their high energy emission peak may fall in the softest part of the LAT energy band.

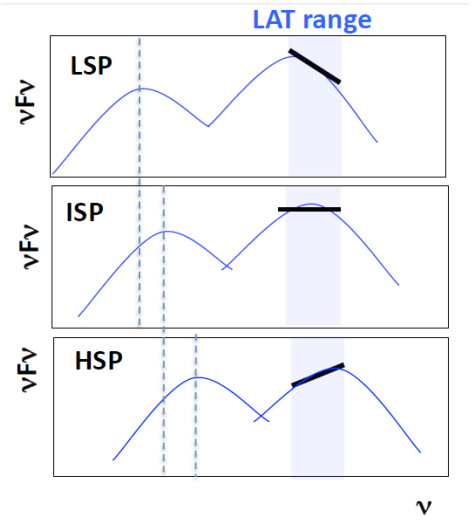

Figure 5.9: LSP, ISP and HSP blazar spectral classification, according to the position of S^{Syn}_{peak}. The filled area represents the portion of the high energy bump covered by LAT, which depends on the blazar SED classification.

Weak objects suffer less cooling losses (Ghisellini et al. 1998) and therefore their spectral peaks are located at higher energies with respect to the powerful blazar population. The synchrotron component peaks above 10^{15} Hz (therefore they are classified as HSPs) and the part of the high energy spectrum affected by cooling effects is well beyond the LAT energy range. Therefore they have a rising spectrum both in the 3FGL and 1FHL catalogs.

There are several complications that affect this simple picture. First, blazars are highly variable objects and variability is more pronounced above the SED peak. Luminous blazars such as FSRQs are more variable. Since our data are not taken simultaneously, the variability may spoil an already weak correlation for these sources. On the other hand, HSPs are not as variable in either band and their correlation is less affected by the use of non simultaneous data.

Chapter 6

Physical and kinematic properties of the HSP blazar Markarian 421

After the characterization of the statistical properties of HSP blazars included in the 1FHL *Fermi* catalog, we discuss in more detail their physical and kinematic properties. For this purpose, one of the best candidates is the HSP source Mrk 421 (R.A.=11^h 04^m 27.313943^s, Dec.=+38° 12′ 31.79906″, J2000), which is one of the brightest 1FHL sources, indicated with a red square symbol in the VLBI flux density vs. 1FHL energy flux scatter plot in Fig. 6.1.

Being one of the nearest (z = 0.03, de Vaucouleurs et al. 1991) BL Lac of HSP spectral type, Mrk 421 is suitable for probing and investigating the physics of the innermost regions of relativistic jets. For this reason, Mrk 421 has been intensively studied throughout the electromagnetic spectrum, especially since it was detected at TeV energies in 1992 (Punch et al. 1992).

Multiwavelength (MWL) coordinated campaigns are a fundamental tool for understanding the physical properties of the source, e.g. by studying variability, which is present at all frequencies, but particularly at TeV energies where Gaidos et al. (1996) measured a doubling time of ∼ 15 minutes. The accurate MWL study and SED modeling performed by Abdo et al. (2011) revealed some interesting

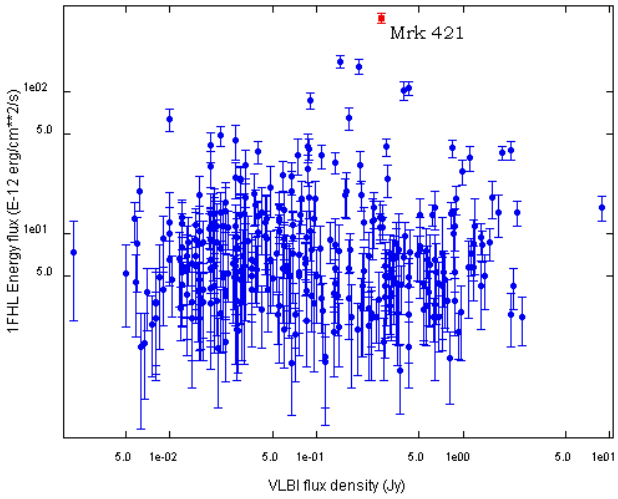

Figure 6.1: VLBI flux density vs. 1FHL energy flux scatter plot. The source Mrk 421 is indicated with a red square symbol.

results, such as the size of the emitting region R and the magnetic field B, which in the context of the leptonic scenario, were estimated to be $R \lesssim 10^4 R_g$ and $B \sim 0.05$ G. However, the details of the physical processes responsible for the observed emission are still poorly constrained. Because of the considerable variability and the broadband spectrum, MWL long-term observations are required for a good comprehension of the emission mechanisms.

At radio frequencies, Mrk 421 shows a one-sided jet structure closely aligned with our line of sight (Giroletti et al. 2006). In this chapter, we present new VLBA observations to study in detail the inner jet structure on parsec scales. The resolution of our observations allows us to investigate the evolution of shocks that arise in the jet, by means of the model-fitting technique. In earlier works (Piner et al. 1999; Piner & Edwards 2004), the jet components show only subluminal apparent motion, which seems to be a common characteristic of TeV blazars. Thanks to accurate measurements of changes on parsec scales, we may find valid constraints on the geometry and kinematics of the jet.

This study is part of a multi-epoch and multi-instrument campaign, which in-

volves observations in the sub-mm (SMA), optical/IR (GASP), UV/X-ray (Swift, RXTE, MAXI), and γ rays (*Fermi*-LAT, MAGIC, VERITAS), as well as at the cm wavelengths with low resolution observations (e.g. F-GAMMA, Medicina). The aim of this observational effort is to shed light on fundamental questions such as the nature of the radiating particles, the connection between the radio and γ-ray emission, the location of the emitting regions, and the origin of the flux variability. VLBI plays an important role in addressing these scientific questions because it is the only technique that can resolve (at least partially) the inner structure of the jet.

We note that, at the redshift of the target, 1 mas corresponds to 0.59 pc.

6.1 Observations

We observed Mrk 421 with the VLBA once per month throughout 2011 at three frequencies: 15, 24, and 43 GHz. Observations were carried out in total and polarized intensity. We also observed, at regular intervals, three other sources (J0854+2006, J1310+3220, and J0927+3902) used as fringe finders and calibrators for the band pass, the instrumental (feed) polarization, and the electric-vector position angle (EVPA). At each epoch, Mrk 421 was observed for nearly 40 minutes at each frequency, spread into several scans of about 3 minutes each, interspersed with calibrator sources in order to improve the (u,v)-coverage. Calibrators were observed for about 10 minutes each, generally spread into three scans of 3 minutes. In some epochs, one or more antennas did not work properly because of technical problems (for a complete report see Table 6.1).

For the a priori calibration, the fringe-fitting procedure, and the detection of cross-polarized fringes we used the software package Astronomical Image Processing System (AIPS) (Greisen 2003). We produced the cleaned and final images with the software package DIFMAP (Shepherd 1997). The polarization D-terms were determined with the task LPCAL in AIPS. We compared antenna tables (which provide the phase and amplitude values for the R and L circular polariza-

Table 6.1: Details of the VLBA observations.

Observation date	MJD	Map peak (mJy/beam)		Beam (mas × mas, °)		1σ rms (mJy/beam)		Notes
		15 GHz	24 GHz	15 GHz	24 GHz	15 GHz	24 GHz	
2011/01/14	55575	348	319	1.05 × 0.65, 15.3	0.79 × 0.47, 8.84	0.19	0.18	No MK, no NL
2011/02/25	55617	391	338	1.16 × 0.74, 14.4	0.64 × 0.39, −6.52	0.35	0.18	NL snowing
2011/03/29	55649	386	359	1.06 × 0.66, −5.37	0.65 × 0.39, −4.26	0.17	0.24	No HK
2011/04/25	55675	367	308	0.92 × 0.50, −3.79	0.61 × 0.34, −3.88	0.28	0.33	-
2011/05/31	55712	355	297	0.93 × 0.51, −5.56	0.64 × 0.35, −8.41	0.25	0.29	-
2011/06/29	55741	262	208	0.89 × 0.50, −7.17	0.56 × 0.32, −12.3	0.17	0.37	No LA
2011/07/28	55770	220	197	0.91 × 0.56, −0.89	0.60 × 0.37, −1.14	0.20	0.30	-
2011/08/29	55802	275	200	0.97 × 0.55, 0.26	0.63 × 0.35, −2.70	0.18	0.27	No HK
2011/09/28	55832	264	238	1.06 × 0.67, 16.2	0.72 × 0.47, 18.4	0.26	0.24	No MK
2011/10/29	55863	261	167	1.06 × 0.69, 0.09	0.73 × 0.44, −3.73	0.26	0.14	HK snowing
2011/11/28	55893	283	201	1.02 × 0.59, 18.0	0.70 × 0.42, 14.3	0.28	0.17	No PT, FD, MK
2011/12/23	55918	295	287	0.89 × 0.49, 1.82	0.61 × 0.35, −5.74	0.15	0.21	No HK

tion for each antenna) at two consecutive epochs to determine the relative EVPA rotations using the IDL routines developed by J. L. Gómez. We calibrated the instrumental polarization using the strong (flux density > 1 Jy) and unresolved source J1310+3220. This source also provides good coverage of the parallactic angle (> 100°) and has negligible polarization on large scales, which is important because of the different angular resolution of the VLBA with respect to the JVLA, whic is used for the calibration of the EVPA (see Sect. 7.1).

In this Chapter, we present the total intensity analysis of the 15 and 24 GHz datasets (Lico et al. 2012), while in Chapter 7 we will present the polarization analysis and the radio vs. γ-ray connection, by including the 43 GHz dataset.

6.2 Results

6.2.1 Images

All the 12 images (one per epoch) at each frequency show a similar structure, consisting of a well-defined and well-collimated one-sided jet structure emerging from a compact nuclear region (core-dominated source). This is the typical structure of a BL Lac object (Giroletti et al. 2004a). A sample couple of 15 and 24 GHz images is shown in Fig. 6.2. The jet extends for roughly 4.5 mas (~2.7 pc), with a position angle (PA) of $\sim -35^{\circ}$. This morphology agrees with the results of other studies of similar angular resolution (Marscher 1999).

We show in Fig. 6.3 two images of Mrk 421 at 15 and 24 GHz, which were produced by stacking all the images respectively at 15 and 24 GHz created with DIFMAP. Since the morphology was stable from epoch to epoch, the stacking did not smear any details of the structure. The alignment of the images was checked by comparing the pixel position of the peak. In both images, we set the lowest contour equal to about three times the off-source residual rms noise level.

6.2.2 Model fits

For each epoch, we used the model-fitting routine in DIFMAP to fit the visibility data of the source in the (u, v) plane with either elliptical or circular Gaussian components. In this way, we were able to investigate in detail the inner jet structure and its evolution.

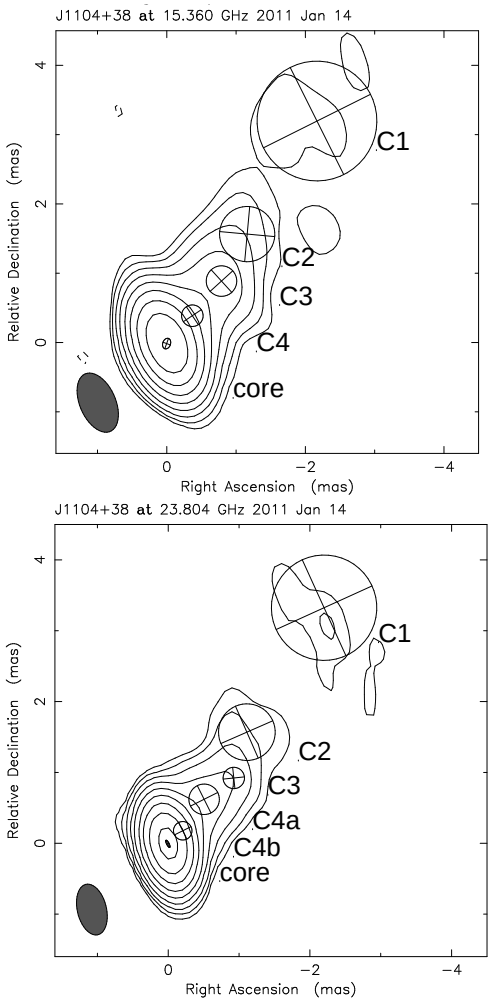

Figure 6.2: Images of Mrk 421 with model fit components for the first epoch at 15 GHz (upper panel) and at 24 GHz (lower panel). Levels are drawn at $(-1, 1, 2, 4...)\times$ the lowest contour, that is at 1.0 mJy/beam for both images, in steps of 2. The restoring beam is shown in the bottom left corner; its size is given in Table 6.1.

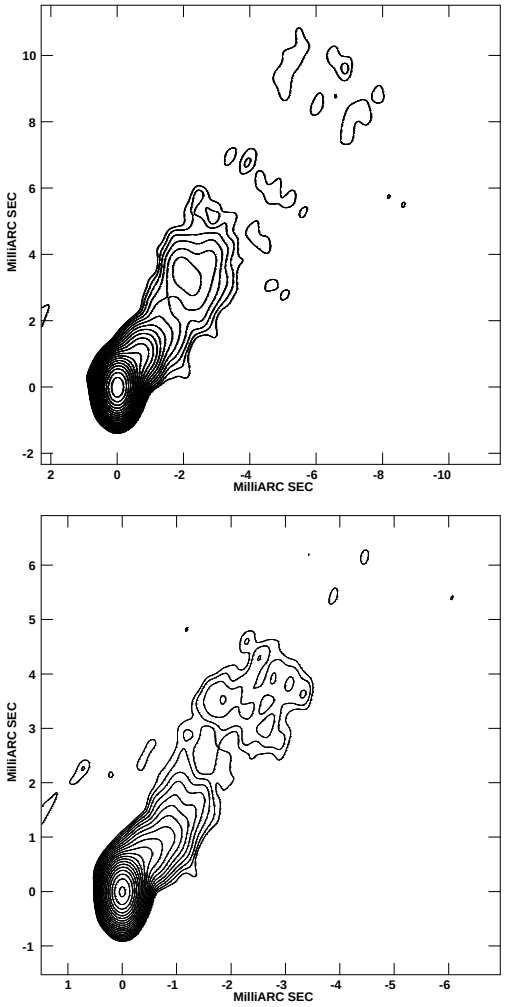

Figure 6.3: Images of Mrk 421 at 15 GHz (upper panel) and 24 GHz (lower panel). These two images were obtained by stacking all of the images of the twelve epochs, at the respective frequency. The restoring beam for the 15 GHz image is 0.9 mas×0.55 mas and the peak flux density is 307.2 mJy/beam. For the 24 GHz image, the restoring beam is 0.6 mas×0.35 mas and the peak is 251.9 mJy/beam. In both images the first contour is 0.35 mJy/beam, which corresponds to three times the off-source noise level. Contour levels are drawn at $(-1, 1, 1.4, 2, 2.8, 4...)$ in steps of $\sqrt{2}$.

Table 6.2: Gaussian models. Col. 1: observing epoch; col. 2: observing frequency; col. 3: component identification; col. 4: flux density in mJy; col. 5: estimated errors for the component flux density; cols. 6 and 8: r and PA are the polar coordinates of the component's center with respect to the core. The PA is measured from North through East; col. 7: estimated errors in the component position; cols. 9 and 10: a and b are the FWHM of the major and minor axes of the Gaussian component; col. 11: Position angle of the major axis measured from North through East.

Epoch	Frequency (GHz)	Component ID	S (mJy)	σ_S (mJy)	r (mas)	σ_r (mas)	PA (deg)	a (mas)	b/a	Φ (deg)
14/01/11	15	Core	350	35	...	...	...	0.16	0.71	-20.0
		C4	30	3.1	0.52	0.08	-43.6	0.31	1.00	...
		C3	22	2.3	1.17	0.08	-41.7	0.44	1.00	...
		C2	8.6	1.0	1.93	0.08	-36.6	0.80	1.00	...
		C1	14	1.5	3.85	0.10	-34.1	1.73	1.00	...
	24	Core	312	31	...	...	...	0.11	0.32	27.3
		C4b	23	2.4	0.26	0.06	-49.3	0.26	1.00	...
		C4a	17	1.8	0.79	0.06	-39.2	0.43	1.00	...
		C3	8.1	1.0	1.3	0.06	-45.1	0.30	1.00	...
		C2	7.1	0.9	1.91	0.06	-35.3	0.80	1.00	...
		C1	5.9	0.8	3.98	0.27	-33.5	1.49	1.00	...
25/02/11	15	Core	386	39	...	...	...	0.10	0.65	43.7
		C4	19	2.2	0.42	0.09	-44.8	0.19	1.00	...
		C3	19	1.3	1.08	0.09	-39.8	0.44	1.00	...
		C2	8.4	1.3	1.91	0.09	-44.8	0.91	1.00	...
		C1	14	1.7	4.06	0.09	-32.9	1.29	1.00	...
	24	Core	335	34	...	...	...	0.07	1.00	...
		C4b	21	2.1	0.24	0.05	-16.0	0.32	1.00	...
		C4a	14	0.9	0.71	0.05	-35.6	0.36	1.00	...
		C3	6.6	0.9	1.29	0.05	-44.2	0.28	1.00	...
		C2	5.3	0.8	1.91	0.07	-34.6	0.80	1.00	...
		C1	6.7	0.9	3.89	0.17	-33.9	1.17	1.00	...
29/03/11	15	Core	379	38	...	...	...	0.04	1.00	...
		C4	16	1.7	0.46	0.08	-34.8	0.28	1.00	...
		C3	21	2.1	1.2	0.08	-36.0	0.46	1.00	...

Table 6.2: Continued.

Epoch	Frequency (GHz)	Component ID	S (mJy)	σ_S (mJy)	r (mas)	σ_r (mas)	PA (deg)	a (mas)	b/a	Φ (deg)
		C2	4.7	0.7	1.86	0.08	-45.2	0.78	1.00	...
		C1	15	1.6	3.82	0.08	-34.3	1.34	1.00	...
	24	Core	358	36	...	...	...	0.06	1.00	...
		C4b	15	1.6	0.32	0.05	-28.9	0.21	1.00	...
		C4a	13	1.5	0.83	0.05	-32.7	0.25	1.00	...
		C3	10	1.2	1.2	0.05	-44.1	0.43	1.00	...
		C2	5.7	0.9	1.96	0.06	-37.3	0.72	1.00	...
		C1	8.5	1.1	4.03	0.25	-36.2	1.31	1.00	...
25/04/11	15	Core	367	37	...	...	...	0.11	0.85	-12.4
		C4	22	2.4	0.45	0.07	-33.6	0.25	1.00	...
		C3	20	2.2	1.21	0.07	-36.7	0.41	1.00	...
		C2	6.7	1.1	2.11	0.07	-46.6	0.85	1.00	...
		C1	16	1.8	3.95	0.12	-33.1	1.47	1.00	...
	24	Core	299	30	...	...	...	0.05	1.00	...
		C4b	27	2.9	0.2	0.05	-41.7	0.12	1.00	...
		C4a	9.4	1.4	0.81	0.05	-32.6	0.26	1.00	...
		C3	10	1.4	1.35	0.05	-39.0	0.37	1.00	...
		C2	5.2	1.1	2.14	0.35	-38.6	1.04	1.00	...
		C1	11	1.5	4.32	0.28	-33.6	1.23	1.00	...
31/05/11	15	Core	346	35	...	...	...	0.04	1.00	...
		C4	24	2.5	0.4	0.07	-29.4	0.25	1.00	...
		C3	17	1.8	1.26	0.07	-33.6	0.40	1.00	...
		C2	4.7	0.9	1.81	0.07	-43.0	0.53	1.00	...
		C1	15	1.7	4.09	0.18	-34.4	1.72	1.00	...
	24	Core	290	29	...	...	...	0.04	1.00	...
		C4b	18	2.0	0.31	0.05	-18.0	0.18	1.00	...
		C4a	10	1.3	0.74	0.05	-31.0	0.29	1.00	...
		C3	7.5	1.1	1.23	0.05	-42.1	0.41	1.00	...
		C2	4.5	1.0	2.01	0.05	-34.2	0.53	1.00	...
		C1	8.9	1.2	4.45	0.35	-35.8	1.35	1.00	...
29/06/11	15	Core	263	26	...	...	...	0.19	0.41	-16.8

Table 6.2: Continued.

Epoch	Frequency (GHz)	Component ID	S (mJy)	σ_S (mJy)	r (mas)	σ_r (mas)	PA (deg)	a (mas)	b/a	Φ (deg)
		C4	26	2.7	0.47	0.07	-30.8	0.26	1.00	...
		C3	16	1.7	1.2	0.07	-37.0	0.51	1.00	...
		C2	6.1	0.8	1.86	0.07	-35.9	0.61	1.00	...
		C1	19	1.9	4.08	0.16	-36.8	2.01	1.00	...
	24	Core	202	20	...	...	...	0.08	1.00	...
		C4b	27	2.9	0.23	0.04	-26.3	0.20	1.00	...
		C4a	12	1.6	0.59	0.04	-28.5	0.23	1.00	...
		C3	13	1.7	1.19	0.04	-37.0	0.51	1.00	...
		C2	6.3	1.3	2.13	0.14	-39.7	0.75	1.00	...
		C1	15	1.9	4.12	0.80	-32.9	2.56	1.00	...
28/07/11	15	Core	231	23	...	...	...	0.23	0.30	-19.4
		C4	26	2.6	0.5	0.07	-30.6	0.30	1.00	...
		C3	14	1.6	1.29	0.07	-35.6	0.45	1.00	...
		C2	5.5	0.8	2.45	0.07	-38.3	0.99	1.00	...
		C1	9.3	1.1	4.45	0.24	-35.5	1.82	1.00	...
	24	Core	199	20	...	...	...	0.14	0.56	-30.9
		C4b	28	2.9	0.29	0.05	-25.3	0.25	1.00	...
		C4a	10	1.4	0.77	0.05	-34.4	0.41	1.00	...
		C3	10	1.3	1.36	0.05	-35.4	0.55	1.00	...
		C2	2.2	0.9	2.13	0.21	-35.4	0.70	1.00	...
		C1	7.9	1.2	3.95	0.80	-35.5	2.36	1.00	...
29/08/11	15	Core	267	27	...	...	...	0.15	0.64	-21.5
		C4	30	3.1	0.33	0.07	-33.3	0.38	1.00	...
		C3	16	1.7	1.2	0.07	-32.0	0.42	1.00	...
		C2	4.6	0.7	1.97	0.07	-43.9	0.64	1.00	...
		C1	13	1.4	3.98	0.17	-34.8	1.86	1.00	...
	24	Core	183	18	...	...	...	0.03	1.00	...
		C4b	30	3.1	0.22	0.05	-18.0	0.17	1.00	...
		C4a	10	1.3	0.78	0.05	-28.9	0.37	1.00	...
		C3	4.5	0.9	1.39	0.05	-40.9	0.28	1.00	...
		C2	3.6	0.9	2	0.09	-31.5	0.66	1.00	...

Table 6.2: Continued.

Epoch	Frequency (GHz)	Component ID	S (mJy)	σ_S (mJy)	r (mas)	σ_r (mas)	PA (deg)	a (mas)	b/a	Φ (deg)
		C1	6.5	1.0	4.19	0.80	-41.0	2.02	1.00	...
28/09/11	15	Core	251	25	...	...	...	0.15	0.58	12.2
		C4	34	3.5	0.33	0.08	-34.3	0.39	1.00	...
		C3	18	1.9	1.15	0.08	-32.1	0.59	1.00	...
		C2	4.2	0.9	2.02	0.13	-43.6	1.13	1.00	...
		C1	12	1.5	4.3	0.34	-32.9	2.26	1.00	...
	24	Core	228	23	...	...	...	0.09	0.42	15.2
		C4b	24	2.5	0.27	0.06	-31.0	0.15	1.00	...
		C4a	15	1.7	0.8	0.06	-30.9	0.42	1.00	...
		C3	3.3	0.8	1.35	0.06	-44.4	0.55	1.00	...
		C2	2.7	0.8	1.85	0.06	-29.0	0.43	1.00	...
		C1	9.2	1.2	4.19	0.80	-33.0	2.19	1.00	...
29/10/11	15	Core	255	25	...	...	...	0.15	0.32	-33.2
		C4	24	2.6	0.47	0.09	-34.3	0.28	1.00	...
		C3	17	1.8	1.12	0.09	-31.7	0.44	1.00	...
		C2	3.0	0.8	1.71	0.09	-35.4	0.44	1.00	...
		C1	11	1.4	4.18	0.24	-33.0	1.98	1.00	...
	24	Core	154	15	...	...	...	0.04	1.00	...
		C4b	21	2.1	0.23	0.06	-23.2	0.18	1.00	...
		C4a	11	1.2	0.8	0.06	-31.5	0.35	1.00	...
		C3	3.3	0.5	1.29	0.06	-32.8	0.41	1.00	...
		C2	3.2	0.5	1.97	0.08	-35.9	0.83	1.00	...
		C1	8.6	1.0	4.23	0.41	-33.0	1.99	1.00	...
28/11/11	15	Core	285	28	...	...	...	0.18	0.15	-14.1
		C4	19	2.1	0.48	0.08	-33.4	0.36	1.00	...
		C3	14	1.7	1.29	0.08	-32.3	0.41	1.00	...
		C2	4.8	1.0	2.04	0.08	-35.5	0.87	1.00	...
		C1	4.8	1.0	3.86	0.16	-33.3	1.17	1.00	...
	24	Core	207	21	...	...	...	0.14	0.58	-22.7
		C4b	17	1.7	0.34	0.05	-24.4	0.34	1.00	...
		C4a	6.7	0.8	0.87	0.05	-33.7	0.36	1.00	...

Table 6.2: Continued.

Epoch	Frequency (GHz)	Component ID	S (mJy)	σ_S (mJy)	r (mas)	σ_r (mas)	PA (deg)	a (mas)	b/a	Φ (deg)
		C3	7.3	0.9	1.35	0.05	-33.7	0.46	1.00	...
		C2	2.7	0.6	2.1	0.05	-32.2	0.68	1.00	...
		C1	6.0	0.8	3.92	0.28	-32.4	1.44	1.00	...
23/12/11	15	Core	230	23	...	...	...	0.07	1.00	...
		C4	14	1.5	0.39	0.07	-27.0	0.38	1.00	...
		C3	12	1.3	1.17	0.07	-32.7	0.50	1.00	...
		C2	5.8	0.7	2.05	0.07	-35.0	0.74	1.00	...
		C1	6.2	0.8	4.16	0.21	-31.4	1.53	1.00	...
	24	Core	271	27	...	...	...	0.04	1.00	...
		C4b	30	3.1	0.16	0.05	-19.5	0.16	1.00	...
		C4a	16	1.8	0.61	0.05	-28.5	0.29	1.00	...
		C3	12	1.3	1.23	0.05	-39.4	0.55	1.00	...
		C2	6.2	0.9	2.04	0.05	-35.0	0.74	1.00	...
		C1	2.6	0.7	4.15	0.80	-31.4	1.53	1.00	...

For all epochs at 15 GHz, a good fit was obtained with five Gaussian components, while at 24 GHz we needed six components, likely due to the higher resolution at such frequency. At both frequencies we identified the core with the brightest, innermost, and most compact feature. We label the other components C1, C2, C3, and C4, starting from the outermost (C1) to the innermost (C4). The higher angular resolution achieved at 24 GHz resolves the second innermost 15 GHz component (C4 located at ~0.45 mas from the core) into two features: C4b at ~0.3 mas and C4a ~0.7 mas from the core (see Fig. 6.2).

Thanks to the good time-sampling, we were able to make an attempt to identify the same component in each epoch. Overall, the components extend out to a region of about 4.5 mas. In this way, with a limited number of components, it was possible to analyze the proper motions and flux density levels of each component at various times. From Fig. 6.4, we can see that the data occupy well-defined regions in the radius vs. time plot, and that this behavior helps us to identify the

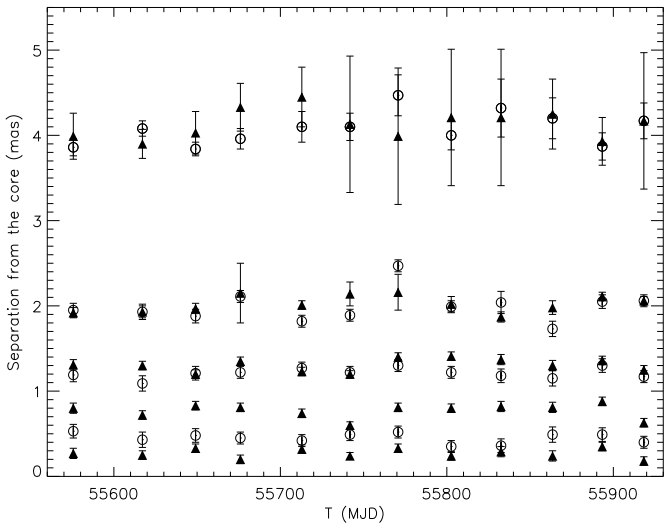

Figure 6.4: Results of model-fit analysis. Circles and triangles refer to the positions of the Gaussian components at 15 and 24 GHz, respectively.

individual components across epochs.

All details of the model fit analysis are shown in Table 6.2. We calculated the uncertainties in the position (error bars in Fig. 6.4) using the ratio of the size of each component to the signal-to-noise ratio (S/N). In the case of bright, compact components, the nominal error value is too small and replaced by a conservative value equal to 10% of the beam size (Orienti et al. 2011). On the other hand, when the calculated error is very large (i.e. comparable to the component radius, as in the case of an extended component with a low flux density), we replace it with a threshold value equal to the maximum value of the calculated errors for the same component at different epochs.

6.2.3 Flux density variability

Using the results of the model-fit technique, we analyzed the temporal evolution of the flux density for each component of the source. The core is the brightest component; at 15 GHz its flux density is $\sim$ 350 mJy. The jet is brighter close

to the core component and then becomes fainter outwards. By comparing the flux density of each component at the various epochs, it emerges that there are no significant variations in the flux densities of the C1-C4 components. The flux density of each component remains roughly constant at various times within the uncertainties providing no indication of flaring activity. Any small variations may be artifacts brought about by our fitting procedures: for instance, the flux density of the inner components may be underestimated in some cases, because part of it was incorporated into the core component flux, or the flux density of the most extended features may be underestimated at epochs missing some short baseline data because of telescope failures.

In Fig. 6.5, we show the light curve for Mrk 421 during 2011 at 15 GHz (upper panel) and at 24 GHz (lower panel), considering the total flux density (squares) and the core flux density (triangles). The light curve reveals an interesting feature: in the second part of the year (starting at MJD ~55700), we note a decrease in the total flux density. From the complete flux-density analysis, we found that the core is the component responsible for the decrease, while the extended region does not display any significant variation. To further exclude calibration effects, we performed the same analysis on the three calibrators. In Fig. 6.5, we present the light curves of the calibrator J1310+3220 (diamonds) at 15 GHz (upper panel) and 24 GHz (lower panel). By this comparison, we can assert that the flux density decrease observed for the core of Mrk 421 is a real feature. Error bars were calculated by considering a calibration error of about 10% of the flux density and a statistical error equal to three times the rms noise on the image plane.

6.2.4 Apparent speeds

From our model-fit, we infer a small or no displacement for the jet components. To verify and quantify this statement, we determined the speed of each component by means of linear fits to the separation of the individual features from the core at different epochs. For the three outer components (C1, C2, and C3), we

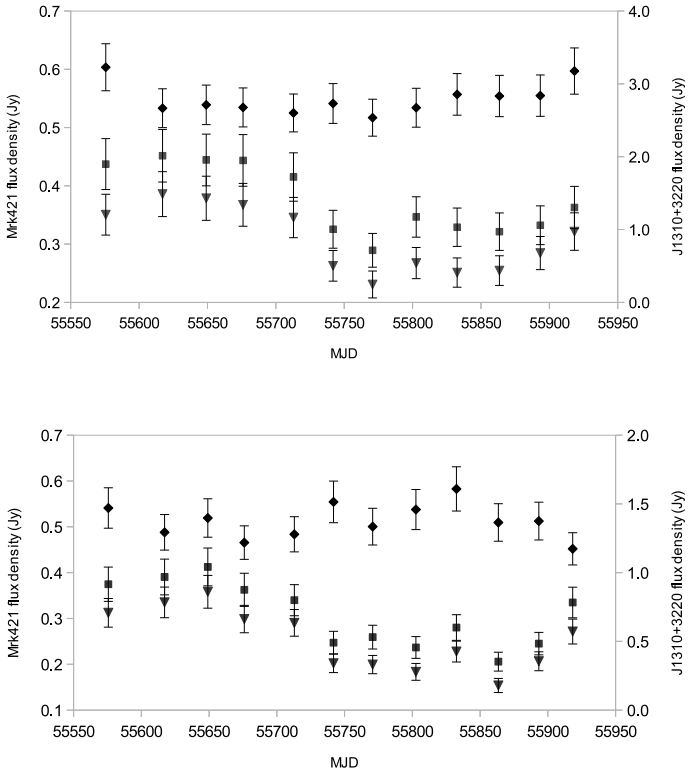

Figure 6.5: Light curves for Mrk 421 (squares represent the total flux density and triangles represent the core flux density) and the calibrator J1310+3220 (diamonds represent the total flux density, with scale given on the right hand y-axis). The upper and lower panels refer to the 15 GHz and 24 GHz data, respectively.

Table 6.3: Apparent speed from the linear fit analysis.

Component	Apparent speed (mas/yr)	β_{app}
C1	0.17 ± 0.12	0.34 ± 0.24
C2	0.08 ± 0.10	0.16 ± 0.20
C3	0.05 ± 0.06	0.10 ± 0.11
C4a	-0.01 ± 0.09	-0.02 ± 0.17
C4b	-0.02 ± 0.06	-0.03 ± 0.11

used combined data at 15 and 24 GHz, since the positions of each component at the two frequencies are generally consistent within the errors. For the two inner components (C4a and C4b), we only used data at 24 GHz. Results are shown in Table 6.3.

We found low values for the apparent speeds, in agreement with previous studies (e.g. Piner & Edwards 2005). The two innermost components (C4a and C4b) are essentially stationary, with an upper limit to their separation velocity of $\sim$ 0.1c. In addition C2 and C3 are consistent with being stationary, while the outermost component C1 has a low-significance (1.5σ) subluminal motion $\sim$ 0.3c. If this trend of increasing velocity at larger radii were real and if the apparent speeds shown in Table 6.3 represented the bulk apparent speed of the plasma in the jet, we could speculate that some mechanism involving an acceleration acts in the outer region of the jet.

6.2.5 Jet/counter-jet ratio

We estimated the ranges of viewing angles θ and of β from the jet/counter-jet brightness ratio. Assuming that the source has two symmetrical jets of the same intrinsic power, we used the Eq. 2.16. For the jet brightness, we used $B_J \sim 28.4$ mJy/beam, measured at 24 GHz, in the image resulting from the stacking of all the 12 epoch images, in the jet region located at $\sim$ 1 mas from the core. For the

counter-jet, which is not visible, we used an upper limit provided by the 3σ rms noise level measured in the image, which resulted in $B_{cJ} = 0.11$ mJy/beam; this consequently yields a lower limit to both R and $\beta \cos\theta$. With a value of $\alpha = 0.4$, obtained for the core component, we obtained $R > 254.8$ and then $\beta \cos\theta > 0.82$. Therefore, the minimum allowed jet bulk velocity is $\beta_{\rm min} = 0.82$ (corresponding to a bulk Lorentz factor $\gamma > 1.74$) and the maximum viewing angle is $\theta_{\rm max} = 35.0°$.

6.3 Discussion

The Doppler factor (Eq. 2.2) is a key element in the study of blazars, since it affects various parameters such as the observed brightness, the SED peak frequency, the variability timescale, and more. Modeling of the SED and study of the variability in different wavebands generally require large values of the blazar Doppler factors; in the case of Mrk 421, Gaidos et al. (1996) estimated $\delta > 9$, from the observed TeV variability time of about 30 min and Abdo et al. (2011) required a Doppler factor between 20 and 50 to reproduce the broadband SED. In turn, VLBI observations can also constrain δ by posing limits on β and θ, as provided by the various arguments discussed earlier in this Chapter.

When closely time spaced repeated observations are available, the study of the proper motion is a useful tool in determining the ranges for β and θ. Surprisingly, several works (e.g. Giroletti et al. 2004b; Piner et al. 2008, 2010) have reported subluminal motions in the jets of TeV blazars, sometimes consistent with the component being stationary. Thanks to the large number of dual-frequency observations, the fine time-sampling, and the high quality of the data provided by the good (u, v)-coverage, we performed a robust identification of the Gaussian components and constrained their motion to be consistent with no displacement at all. At the same time, the high sensitivity and in particular the stacked image place significant constraints on the jet/counter-jet ratio.

The first immediate consequence is that we can reject the hypothesis that the

small $\beta_{\rm app}$ is solely due to a projection effect, since it would require an unrealistically narrow viewing angle: in the case of component C4b, the upper limit to the observed motion implies a viewing angle $< 1.3^\circ$ to reproduce the observed jet/counter-jet ratio (and even smaller to agree with the high energy limits). If the jets' distribution is isotropic on the sky, the real number of misaligned sources (parent population) is incompatible with these small values of θ. For example, in the Bologna Complete Sample selected by Giovannini et al. (2005) at low frequency (and thus free from Doppler favoritism bias), one would expect fewer than 0.03 sources with $\theta < 1.3^\circ$ (see also Tavecchio 2005; Henri & Saugé 2006).

On the other hand, since larger values of the viewing angle capable of reproducing the observed lack of proper motion are incompatible with the jet/counter-jet ratio, we conclude that the pattern velocity cannot be representative of the bulk flow velocity. The Gaussian components obtained in our model fit provide a good description of the visibility data but do not represent well-defined, high-contrast jet features (see Lyutikov & Lister 2010). In our interpretation, the low apparent speeds found imply that the proper motion of Mrk 421 does not provide any information about the jet bulk velocity; even on the basis of the sole jet brightness ratio, untenable viewing angles would be necessary to match the pattern and bulk velocities.

What then are the real values of the viewing angle and the jet bulk velocity in Mrk 421? To reproduce the observed jet asymmetry, we needed to consider a range of velocities $0.82 < \beta < 1$ and angles $0^\circ < \theta < 35.0^\circ$. We could exclude the upper range of the θ values, since this would not reproduce the high Doppler factors required by high energy observations (Gaidos et al. 1996; Abdo et al. 2011); in particular, we were unable to achieve $\delta > 20, 10, 5, 3$ when $\theta > 3.0^\circ, 5.7^\circ, 11.5^\circ, 19.4^\circ$, respectively.

Smaller angles thus seem to be favored since they were the only ones consistent with high values of δ. However, such small angles would still represent a challenge to the observed radio properties. We were able to estimate the in-

trinsic power of the radio core $P_c^{\rm intr}$, by debeaming the observed monochromatic luminosity of the core $P_c^{\rm obs}$ with the equation

$$P_c^{\rm obs} = P_c^{\rm intr} \times \delta_c^{2+\alpha}.$$

With a value of $P_c^{\rm obs} \sim 6.8 \times 10^{23}$ W Hz^{-1} at 15 GHz, $\alpha = 0.4$, and $\delta = 20$, we obtained for the intrinsic power of the core $P_c^{\rm intr} \sim 5.8 \times 10^{20}$ W Hz^{-1}; this value is at the very low end of the typical range of intrinsic power found for different samples of radio galaxies (e.g. Liuzzo et al. 2011), suggesting that lower values of δ provide a more typical core power.

Moreover, the 12 monthly observations have not revealed any dramatic flux-density variability in the core of the source, which further points to a lower Doppler factor for the radio jet. We estimated the variability brightness temperature of the core ($T_{\rm B,var}$) by using the Eq. 1.2. With the values provided by our observations and $\tau \sim 90$ days, we obtained a value of $T_{\rm B,var} \sim 2.1 \times 10^{10}$ K, which does not require any significant beaming.

We similarly calculated $T_{\rm B}$ for the most compact component by using the Eq. 1.1. The resulting $T_{\rm B}$ is on the order of 1×10^{11} K, only slightly exceeding the limit derived by Readhead (1994) from equipartition arguments.

Taken together, the lack of superluminal features, the low core dominance, and the weak variability suggest a scenario in which no strong beaming is required in the radio jet. Low values of the Doppler factor, e.g. $\delta \sim 3$, can reproduce the observational radio properties, including the jet brightness asymmetry.

We conclude that the Doppler factor must be different in the radio band than in the γ-ray band. Since we do not expect that the viewing angle changes significantly, this leads us to the necessity of a velocity structure in the jet, as previously discussed by e.g. Chiaberge et al. (2000), Georganopoulos & Kazanas (2003), and Ghisellini et al. (2005). The presence of a transverse velocity structure across the jet axis is supported by a limb brightening that we reveal in the 43 GHz images (see Chapter 7 for a detailed discussion). This structure consists of two compo-

nents: a fast inner *spine* and a slower outer *layer*. Different Doppler factors were obtained depending on whether we measured the speed of the spine or the layer.

A viable scenario for Mrk 421 is that the viewing angle is between 2° and 5°, which is consistent with the statistical counts of low-power radio sources and the possibility of reaching the high Doppler factors required by SED modeling and high energy variability. The jet velocity is structured, with a typical Lorentz factor of $\gamma \sim 1.8$ in the radio region (yielding $\delta \sim 3$), and $\gamma \sim \delta \sim 20$ in the high energy emission region.

Chapter 7

Polarization properties and γ-ray connection in Mrk 421

Since the emission from blazar objects is dominated by nonthermal radiation, studying their polarization properties can provide important information on the magnetic field structure and the emission mechanisms. Furthermore, thanks to the MWL observations, we can investigate the location where the radiation is produced.

On the other hand, cross-correlation studies of VLBA data with data from other energy ranges (in particular γ rays) can provide us with important information about the structure of the jet and the location of the blazar emission.

In this Chapter we present the analysis of the multi-frequency VLBA observations in linearly polarized intensity, introduced in Chapter 6, which allows us to determine some physical parameters such as the degree of polarization and the absolute orientation of the EVPA, and to obtain some useful information on the magnetic field topology. We also investigate the possible radio and γ-ray connection by using the data collected by the *Fermi*-LAT during the entire 2011.

Table 7.1: VLBA 43 GHz data provided by the Boston University blazar monitoring program. Col. 1: observing date; Col. 2: Observing MJD; Col. 3: flux density in mJy; Col. 4: estimated errors for the flux density.

Epoch	MJD	S	σ_S
year/month/day		(mas)	(mas)
2011/01/02	55563	328.0	21.9
2011/02/04	55597	355.3	23.7
2011/03/01	55621	415.9	27.7
2011/04/21	55673	324.6	21.6
2011/05/22	55703	275.0	18.3
2011/06/12	55724	223.6	14.9
2011/07/21	55763	177.0	11.8
2011/08/23	55796	220.3	14.7
2011/09/16	55820	162.7	10.8
2011/10/16	55850	189.0	12.6
2011/12/02	55897	199.6	13.3

7.1 Polarization calibration

For the present analysis, our 43 GHz dataset has been expanded by adding data from 11 epochs provided by the VLBA Boston University blazar program[1] (see Table 7.1).

In general, to obtain the absolute orientation of the EVPAs (defined as $\chi = 0.5 \times \arctan(U/Q)$, where U and Q are Stokes flux densities) in VLBI observations, a comparison with quasi-simultaneous single-dish or JVLA observations is required. This is because of the lack of polarization calibrators with stable EVPAs on (sub)milliarcsecond scales.

To determine the EVPA absolute orientation, we used the method developed by Leppänen et al. (1995), which makes use of the instrumental polarization pa-

[1] `http://www.bu.edu/blazars/VLBAproject.html`

rameters (the so-called D-terms). This method provides us with an independent way of calibrating the absolute right-left (R-L) circular polarization phase offset; it is based on the assumption that the D-terms change slowly with time (see Gómez et al. 2002). For most of the antennas we found that D-terms remain stable during the whole 12-month observing period.

The method consists of comparing the D-terms for each antenna in consecutive epochs, which yields the relative rotation in right (R) and left (L) circular polarization. In other words, the phase offset in R and L between two epochs is provided by the phase difference of the D-terms. We note that since the VLBA consists of ten antennas, twenty different values are involved in the comparison to determine the relative rotation between two epochs, (two R-L values for each antenna). This guarantees an accurate and reliable determination of the phase offset in case of an antenna failure.

The relative rotations obtained for 15, 24, and 43 GHz are reported in Cols. 4, 7, and 10 in Table 7.2. For a specific epoch the relative rotation may differ at different frequencies because it depends on the reference antenna used for the calibration (the reference antennas used at the different frequencies are listed in Cols. 5, 8, and 11 in Table 7.2).

After determining the relative rotations, we set the absolute EVPA calibration for one epoch by comparison with a JVLA observation provided by the POLCAL program[2] (values in boldface in Table 7.2). Then we determined the absolute orientation for all the EVPAs by applying the relative rotations obtained from the D-terms. For example, after fixing a value in the third column for the 15 GHz data by the comparison with JVLA, we obtained the other values by summing the previous value in the same column and the relative rotation for the same epoch in Col. 4. For example, at 15 GHz in Col. 3 of Table 7.2 for the 11th observing epoch (November 2011) we obtain the value of 25.5° by the comparison with JVLA. Then, to obtain the absolute rotation for the consecutive epoch (December

[2] http://www.aoc.nrao.edu/~smyers/evlapolcal/polcal_master.html

Table 7.2: Final EVPA rotations for 15, 24, and 43 GHz (Cols. 3, 6, and 9, respectively); numbers in boldface refer to the comparison with JVLA values. We also report the relative rotations, obtained by comparing antenna tables for consecutive epochs, and the reference antennas used for the phase calibration.

Epoch	MJD	Final Δ[a]	ΔD-terms[b]	Reference	Final Δ[a]	ΔD-terms[b]	Reference	Final Δ[a]	ΔD-terms[b]	Reference[c]
year/month/day		(deg)	(deg)	antenna	(deg)	(deg)	antenna	(deg)	(deg)	antenna
		15 GHz			24 GHz			43 GHz		
2011/01/14	55575	−21.7		PT	−8.5		PT	−3.2		PT
2011/02/25	55617	−21.7	0	PT	−8.5	0	PT	−3.2	0	PT
2011/03/29	55649	**−21.7**	0	PT	**−8.5**	0	PT	**−3.2**	0	PT
2011/04/25	55675	−21.7	0	PT	−8.5	0	PT	−3.2	0	PT
2011/05/31	55712	−21.7	0	PT	−8.5	0	PT	−3.2	0	PT
2011/06/29	55741	**22.2**	45	OV	−91	−82.5	OV	−25.2	−22	KP
2011/07/28	55770	22.2	0	OV	−153.5	−62.5	KP	−25.2	0	KP
2011/08/29	55802	85.2	63	KP	−153.5	0	KP	−25.2	0	KP
2011/09/28	55832	157.2	72	PT	−6.5	−33	PT	6.8	32	PT
2011/10/29	55863	157.2	0	PT	−6.5	0	PT	6.8	0	PT
2011/11/28	55893	**25.5**	45	OV	**−79.7**	−67.7	OV	**−49.2**	−51	OV
2011/12/23	55918	−19.5	-45	PT	−9.7	−110	PT	0.8	50	KP

[a] Final rotation to apply to obtain the absolute EVPA orientation.

[b] Relative rotation obtained by comparing antenna table of two consecutive epochs.

[c] PT = Pie Town, KP = Kitt Peak, OV = Owens Valley.

2011), we just add the relative rotation to the value of 25.5° (fourth column), which in this case is −45°, and we obtain a final rotation of −19.5°. The relative rotation between two epochs is 0° for the same reference antenna at both epochs.

At 15 GHz we have three JVLA measurements taken during 2011, which enabled two cross checks. The values obtained with the D-terms method and those from the comparison with the JVLA agree within 5°. For the 24 and 43 GHz observations we have two JVLA measurements, which we also cross-checked, finding a good agreement within 5°. This confirms the validity and accuracy of the D-terms calibration method previously reported by Gómez et al. (2002).

7.1.1 Determination of uncertainties

Error bars for the total intensity flux density (S) and the linearly polarized emission (defined as $P = \sqrt{Q^2 + U^2}$) were calculated by considering a calibration uncertainty σ_c of about 10% of the flux density and a statistical error provided by the rms noise measured in the image plane.

To determine the statistical error for the jet emission we also took the number of beams into account:

$$\Delta_S = \sqrt{\sigma_c^2 + \left(\sqrt{\frac{\text{box size}}{\text{beam size}}} \times rms \right)^2}. \tag{7.1}$$

The box size term is defined in Sect. 7.3.1. The uncertainties in fractional polarization (defined as $m = P/S$) were calculated from error propagation theory:

$$\Delta m = \frac{1}{S} \sqrt{\sigma_P^2 + \left(\frac{P}{S} \times \sigma_S \right)^2}, \tag{7.2}$$

where σ_S and σ_P represent the uncertainties in S and P.

The uncertainties in EVPA values were calculated by taking into account all of these contributions:

$$\Delta\chi = \sqrt{\sigma_{\text{cal}}^2 + \sigma_{\text{D-terms}}^2 + \sigma_{\text{JVLA}}^2 + \sigma_{\chi}^2}, \tag{7.3}$$

where $\sigma_{\rm cal}$ is the scatter of the value measured on the polarization image, $\sigma_{\rm D-terms}$ is the calibration uncertainty introduced when we compare D-terms at different epochs to obtain the relative rotations by using the antenna tables, and $\sigma_{\rm JVLA}$ is the 5° mean difference between the JVLA and the D-terms methods. The last term σ_χ is the uncertainty in χ calculated from error propagation theory:

$$\sigma_\chi = \frac{0.5}{Q^2 + U^2}\sqrt{U^2\Delta_Q^2 + Q^2\Delta_U^2}, \tag{7.4}$$

where Δ_Q and Δ_U are the uncertainties in the Q and U Stokes flux densities, which are calculated using Eq. (7.1). Since $\Delta_Q \sim \Delta_U$ (Fanti et al. 2001), the formula becomes

$$\sigma_\chi = \frac{0.5 \times \Delta_Q}{\sqrt{Q^2 + U^2}} = 0.5 \times \frac{\Delta_Q}{P}. \tag{7.5}$$

To determine the polarization parameters we did not include the random noise correction (Wardle & Kronberg 1974); this contribution is always within the uncertainties.

7.2 *Fermi*-LAT data: selection and analysis

The *Fermi*-LAT data reported here were collected from 2011 January 1 (MJD 55562) to December 31 (MJD 55926). During this time, the *Fermi* observatory operated almost entirely in survey mode. The analysis was performed with the software package `ScienceTools` version v9r32p5. The LAT data were extracted within a region of 20° radius centered on the location of Mrk 421. Only events belonging to the 'Source' class were used. The time intervals collected when the rocking angle of the LAT was greater than 52° were rejected. In addition, a cut on the zenith angle (< 100°) was applied to reduce contamination from the Earth limb γ rays, which are produced by cosmic rays interacting with the upper atmosphere. The spectral analysis was performed with the instrument response functions `P7REP_SOURCE_V15` using an unbinned maximum-likelihood method implemented in the Science tool `gtlike`. A Galactic diffuse emission model and

isotropic component, which is the sum of an extragalactic and residual cosmic-ray background, were used to model the background[3]. The normalizations of the two components in the background model were allowed to vary freely during the spectral fitting.

We analyzed a region of interest of 10° radius centered on the location of Mrk 421. We evaluated the significance of the γ-ray signal from the sources by means of the maximum-likelihood test statistic TS = 2Δlog(likelihood) between models with and without a point source at the position of Mrk 421 (Mattox et al. 1996). The source model used in `gtlike` includes all of the point sources from the 2FGL catalog (Nolan et al. 2012) that fall within 15° of the source. The spectra of these sources were parametrized by power-law functions, except for 2FGL J1015.1+4925, for which we used a log-parabola as in the 2FGL catalog. A first maximum-likelihood analysis was performed to remove from the model the sources with TS < 25 and/or the predicted number of counts based on the fitted model $N_{pred} < 3$. A second maximum-likelihood analysis was performed on the updated source model. In the fitting procedure, the normalization factors and the photon indexes of the sources lying within 10° of Mrk 421 were left as free parameters. For the sources located between 10° and 15° from our target, we kept the normalization and the photon index fixed to the values from the 2FGL catalog.

The systematic uncertainty on the effective area[4] is 10% below 100 MeV (Ackermann et al. 2012a), decreasing linearly with the logarithm of energy to 5% between 316 MeV and 10 GeV, and increasing linearly with the logarithm of energy up to 15% at 1 TeV.

[3] `http://fermi.gsfc.nasa.gov/ssc/data/access/lat/BackgroundModels.html`
[4] `http://fermi.gsfc.nasa.gov/ssc/data/analysis/LAT_caveats.html`

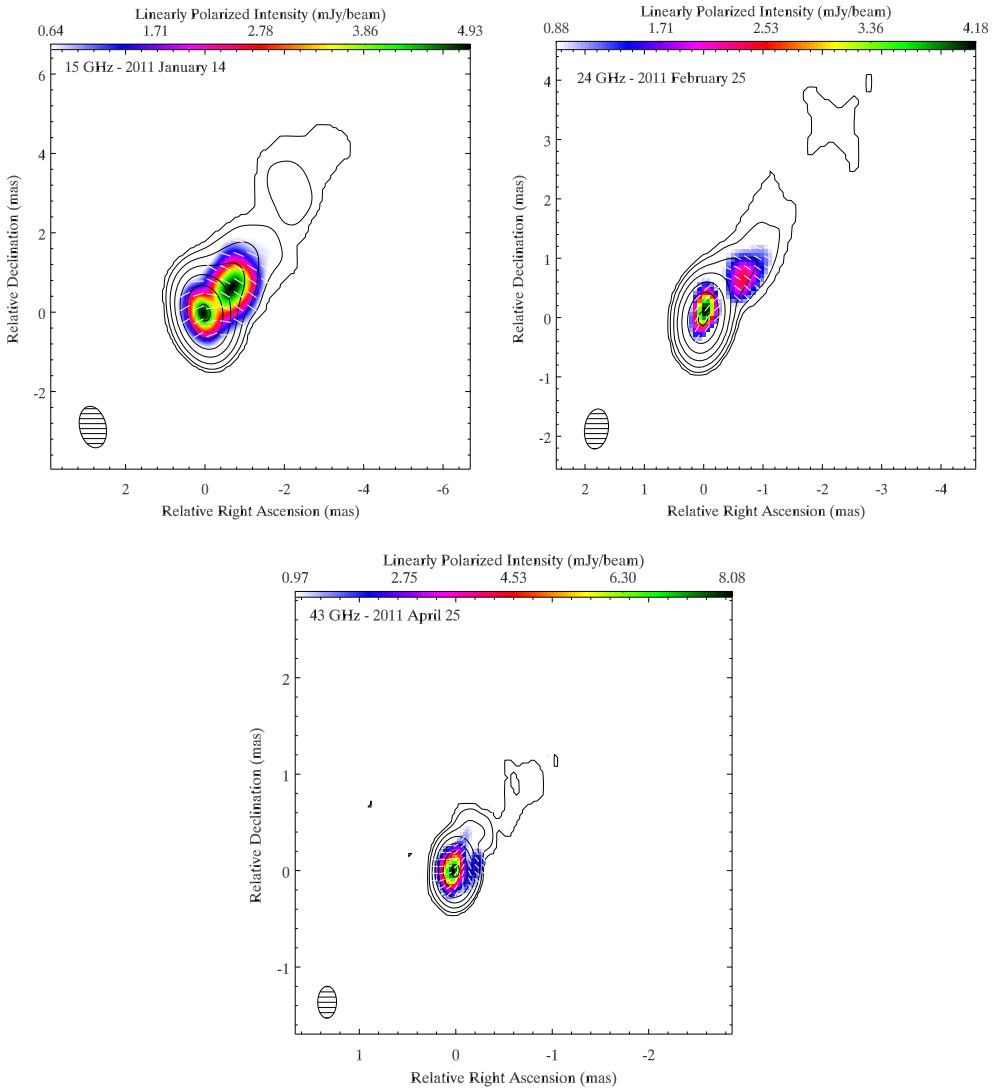

Figure 7.1: Images of Mrk 421 for the first observing epoch at 15 GHz (top left image), the second observing epoch at 24 GHz (top right image), and the third observing epoch at 43 GHz (bottom image). Levels are drawn at $(-1, 1, 2, 4...)\times$ the lowest contour (that is, at 1.0 mJy/beam for 15 and 24 GHz images and at 0.65 mJy/beam for the 43 GHz image) increasing by factors of 2. The restoring beam, shown in the bottom left corner, has a value of 1.05 mas $\times$ 0.66 mas, 0.67 mas $\times$ 0.40 mas, and 0.33 mas $\times$ 0.19 mas for 15, 24, and 43 GHz, respectively. The overlaid color maps show the linearly polarized intensity, and bars represent the absolute orientation of the EVPAs.

7.3 Results

7.3.1 Images and morphology

In Fig. 7.1 we show a sample of three polarization images of Mrk 421 at 15 GHz (upper left panel), 24 GHz (upper right panel), and 43 GHz (lower panel) produced with DIFMAP and IDL[5]. To improve the sensitivity to the extended jet emission, we restored the images with natural weighting. The contours show the total intensity, the overlaid color maps show the linearly polarized intensity. Bars represent the absolute orientation of the EVPAs. We note that the position of the peak in the linearly polarized and total intensity emission images do not always coincide. For example, in the first observing epoch at 15 GHz (upper panel in Fig. 7.1), the peak is 4.93 mJy/beam, and it is not coincident with the total intensity peak, instead it lies in the jet about 1 mas from the core region. From the total intensity images at all three frequencies, we detect a well-defined and collimated one-sided jet structure, emerging from a compact nuclear region that extends about 4.5 mas (∼2.7 pc), with a PA of about −35°. At 15 GHz the linearly polarized emission extends for about 1 mas from the core region, allowing us to distinguish core and jet emission. The outer polarized emission is too faint to be detected. The polarized emission in the jet becomes fainter at higher frequencies: at 24 GHz it is still detected, but at 43 GHz we only detect polarized emission from the core region; this is probably due to sensitivity limitations.

We estimated the jet polarized flux density as the difference between the total amount and the contribution of the core region. In practice, we first measured the total polarized flux density $P_{\rm tot}$ at each epoch by setting a box containing the entire polarized region; we adjusted the size of the box depending on the extension of the polarized emission. We then determined the core contribution $P_{\rm core}$ from the value of the polarized flux density at the position of the total intensity peak. Finally, we estimated the jet polarized flux density as $P_{\rm jet} = P_{\rm tot} - P_{\rm core} \times \cos(\chi_{\rm core} - \chi_{\rm jet})$. We

[5] http://www.exelisvis.com/ProductsServices/IDL.aspx

also determined the jet EVPA directly on the image at the location where the jet polarized flux density is highest.

Table 7.3: Summary of the total and polarized intensity parameters plotted in Figs. 7.2 and 7.3. Col. 1: obseving date; col. 2: obseving frequency; col. 3: source region; col. 4: flux density in mJy; col. 5: estimated errors for the flux density; col. 6: polarized flux density in mJy; col. 7: estimated errors for the polarized flux density; col. 8: fractional polarization; col. 9: estimated errors for the fractional polarization; col. 10: EVPAs; col. 11: estimated errors for the EVPAs.

Epoch	Frequency	Region	S	σ_S	P	σ_P	m	σ_m	χ	σ_χ
year/month/day	(GHz)		(mJy)	(mJy)	(mJy)	(mJy)	(%)	(%)	(deg)	(deg)
2011/01/14	15	Core	332.2	33.2	4.9	0.5	1.5	0.2	108.3	8.7
		Jet	60.5	6.1	8.9	1.0	14.8	2.3	58.3	7.5
	24	Core	318.9	31.9	2.7	0.3	0.8	0.1	126.5	8.8
		Jet	47.4	4.8	6.4	0.9	13.6	2.3	58.5	9.0
	43	Core	291.2	29.1	2.2	0.3	0.8	0.1	117.8	10.9
2011/02/25	15	Core	392.9	39.3	4.2	0.4	1.1	0.2	117.3	7.8
		Jet	43.4	4.4	6.5	0.8	15.0	2.5	55.3	8.1
	24	Core	419.9	42.0	4.2	0.5	1.0	0.1	143.5	8.2
		Jet	45.1	4.6	5.7	0.9	12.6	2.3	55.5	8.7
	43	Core	408.6	40.9	2.6	0.3	0.6	0.1	113.8	10.2
2011/03/29	15	Core	399.6	40.0	2.6	0.3	0.7	0.1	177.3	12.4
		Jet	55.7	5.6	7.6	0.9	13.7	2.2	56.3	12.6
	24	Core	364.7	36.5	5.5	0.6	1.5	0.2	172.5	12.3
		Jet	39.6	4.0	11.5	1.3	29.1	4.4	61.5	12.5
	43	Core	346.8	34.7	12.5	1.4	3.6	0.5	142.8	13.1
2011/04/25	15	Core	367.4	36.7	5.1	0.5	1.4	0.2	174.3	10.5
		Jet	47.3	4.8	16.5	1.8	34.8	5.1	58.3	8.9
	24	Core	328.8	32.9	6.5	0.7	2.0	0.3	157.5	10.5
		Jet	44.0	4.5	16.4	1.7	37.3	5.5	72.5	10.5
	43	Core	306.7	30.7	8.1	0.8	2.6	0.4	130.8	11.8
2011/05/31	15	Core	344.4	34.4	1.1	0.2	0.3	0.1	130.3	13.8
		Jet	43.7	4.4	5.4	0.8	12.3	2.2	51.3	9.6

Table 7.3: Continued.

Epoch	Frequency	Region	S	σ_S	P	σ_P	m	σ_m	χ	σ_χ
year/month/day	(GHz)		(mJy)	(mJy)	(mJy)	(mJy)	(%)	(%)	(deg)	(deg)
	24	Core	301.4	30.1	3.0	0.3	1.0	0.1	168.5	10.1
		Jet	35.3	3.6	3.7	0.7	10.4	2.2	66.5	11.4
	43	Core	246.8	24.7	3.4	0.4	1.4	0.2	149.8	10.1
2011/06/29	15	Core	264.6	26.5	1.8	0.2	0.7	0.1	102.2	11.4
		Jet	55.6	5.6	8.9	1.1	16.0	2.5	61.2	11.6
	24	Core	219.5	22.0	2.2	0.3	1.0	0.2	144.0	14.7
		Jet	37.3	3.9	6.0	1.0	16.2	3.2	46.0	13.0
	43	Core	176.0	17.6	2.4	0.4	1.3	0.2	129.8	11.5
2011/07/28	15	Core	246.8	24.7	2.6	0.4	1.1	0.2	196.2	20.2
		Jet	45.9	4.7	6.4	1.1	13.9	2.7	56.2	20.2
	24	Core	215.3	21.5	4.0	0.5	1.9	0.3	165.5	20.4
		Jet	43.3	4.4	1.8	1.1	4.2	2.5	52.5	26.3
	43	Core	195.9	19.6	3.4	0.5	1.7	0.3	159.8	20.0
2011/08/29	15	Core	299.2	29.9	4.4	0.5	1.5	0.2	91.2	13.4
		Jet	47.3	4.8	12.6	1.5	26.6	4.2	63.2	14.4
	24	Core	259.5	25.9	2.6	0.4	1.0	0.2	115.5	13.4
		Jet	38.9	4.0	7.9	1.2	20.3	3.7	49.5	14.3
	43	Core	216.1	21.6	4.7	0.5	2.2	0.3	172.8	13.7
2011/09/28	15	Core	275.4	27.5	2.5	0.3	0.9	0.1	181.2	18.1
		Jet	38.7	3.9	3.8	0.8	9.7	2.2	57.2	18.8
	24	Core	258.7	25.9	4.0	0.5	1.6	0.2	175.5	17.9
		Jet	42.2	4.3	5.3	1.0	12.7	2.8	42.5	19.2
	43	Core	227.0	22.7	3.0	0.4	1.3	0.2	149.8	18.5
2011/10/29	15	Core	267.8	26.8	4.7	0.5	1.8	0.3	108.2	10.5
		Jet	53.1	5.4	5.5	0.9	10.3	2.0	65.2	11.1
	24	Core	259.7	26.0	1.8	0.3	0.7	0.1	103.5	13.3
		Jet	34.1	3.5	6.8	0.9	19.9	3.4	43.5	12.1
	43	Core	233.9	23.4	2.5	0.4	1.1	0.2	140.8	11.5
2011/11/28	15	Core	303.8	30.4	2.6	0.4	0.9	0.1	106.5	17.1
		Jet	43.1	4.4	7.0	1.1	16.2	3.1	83.5	17.6
	24	Core	304.1	30.4	2.1	0.3	0.7	0.1	109.3	18.5

Table 7.3: Continued.

Epoch	Frequency	Region	S	σ_S	P	σ_P	m	σ_m	χ	σ_χ
year/month/day	(GHz)		(mJy)	(mJy)	(mJy)	(mJy)	(%)	(%)	(deg)	(deg)
		Jet	40.7	4.3	2.9	1.0	7.0	2.6	115.3	19.6
	43	Core	278.5	27.9	3.1	0.4	1.1	0.2	152.8	17.2
2011/12/23	15	Core	303.8	30.4	2.9	0.4	1.0	0.2	114.5	14.1
		Jet	46.3	4.7	3.6	0.9	7.8	2.0	64.5	13.6
	24	Core	284.9	28.5	1.9	0.3	0.7	0.1	144.3	13.8
		Jet	25.8	2.7	0.4	0.6	1.6	2.3	-	-
	43	Core	202.9	20.3	3.3	0.4	1.6	0.3	162.8	12.5

The 43 GHz images reveal a transverse structure in the inner part of the jet in the form of limb brightening in the polarized emission. This transverse structure is clearly revealed in the April 2011 polarization image (see lower panel in Fig. 7.1). During this epoch the polarization emission peak is in the core region and is $\sim$ 8 mJy/beam, while in the limbs the polarization peak is $\sim$ 2.3 mJy/beam. The limb-brightening structure is also detected in March and May 2011, but it is less pronounced, while it is absent from all the other epochs.

7.3.2 Radio light curves and evolution of polarization angle

In Fig. 7.2, we show the light curves for the core region of Mrk 421 during 2011 at 15 GHz (upper frame), 24 GHz (middle frame), and 43 GHz (lower frame). For each frame, we show in four panels (from top to bottom) the total intensity and the polarized flux density, the fractional polarization, and the EVPAs. The plots for the jet region are shown in Fig. 7.3 at 15 GHz (upper frame) and 24 GHz (lower frame). No polarized emission from the jet is apparent in the 43 GHz images. All of these values are reported in Table 7.3.

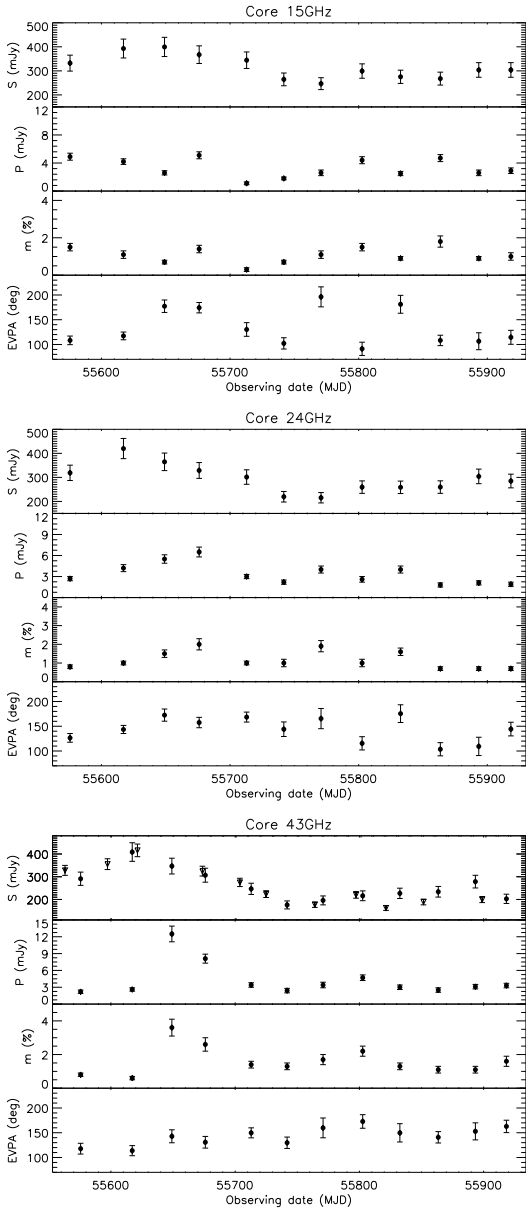

Figure 7.2: Evolution with time of some observational parameters of Mrk 421 in the core region at 15 GHz (upper frame), 24 GHz (middle frame), and 43 GHz (lower frame). For each frame we report from the first to the fourth panel the light curves for the total intensity, the polarized flux density, the fractional polarization, and the EVPA values. In the lower frame (first panel) triangles represent the VLBA 43 GHz observations of Mrk 421 provided by the VLBA-BU-BLAZAR program.

Core region

For all the three observing frequencies (15, 24, and 43 GHz) the total intensity light curves peak around the end of February (MJD ~55617), with a decrease until July 28 (MJD 55770) followed by a slight increase in the last part of the year.

In the core region the linearly polarized emission at 15 GHz and 24 GHz is significantly variable ($> 3\sigma$ difference between the highest and the lowest value), but we observe the most significant variation at 43 GHz, where we detect a peak of 12.5 mJy/beam during the third observing epoch (MJD ~55649). This behavior may be connected with the enhanced activity in the γ-ray light curve between MJD 55562 and MJD 55660, as described in Sect. 7.3.4.

The core polarization fraction has a mean value of 1%, in agreement with other studies of this source (e.g., Marscher et al. 2002; Pollack et al. 2003). At 43 GHz the polarization percentage is higher, around 2%, reaching $\sim$ 4% during the third observing epoch, which is close in time with the enhanced activity at high energy.

In the bottom panel of each frame of Fig. 7.2, we also show the trend of the polarization angle for the core region of Mrk 421 during 2011 at 15 GHz (upper frame), 24 GHz (middle frame), and 43 GHz (lower frame). The EVPAs vary. For most of the year, they show values varying between 110° and 150°. In between some pairs of epochs, in particular at 15 GHz, they change by about 90°, which has no clear connection with the EVPA variation at 24 and 43 GHz or with the polarized flux density trend.

Jet region

The light curves for the jet region, extending to about 1 mas from the core at 15 and 24 GHz, are shown in Fig. 7.3. The situation is different in the jet with respect to the core region. The total intensity flux density for the extended region does not show any significant variation. The polarized flux density shows some variability, reaching a peak during the fourth epoch at 15 and 24 GHz. The polar-

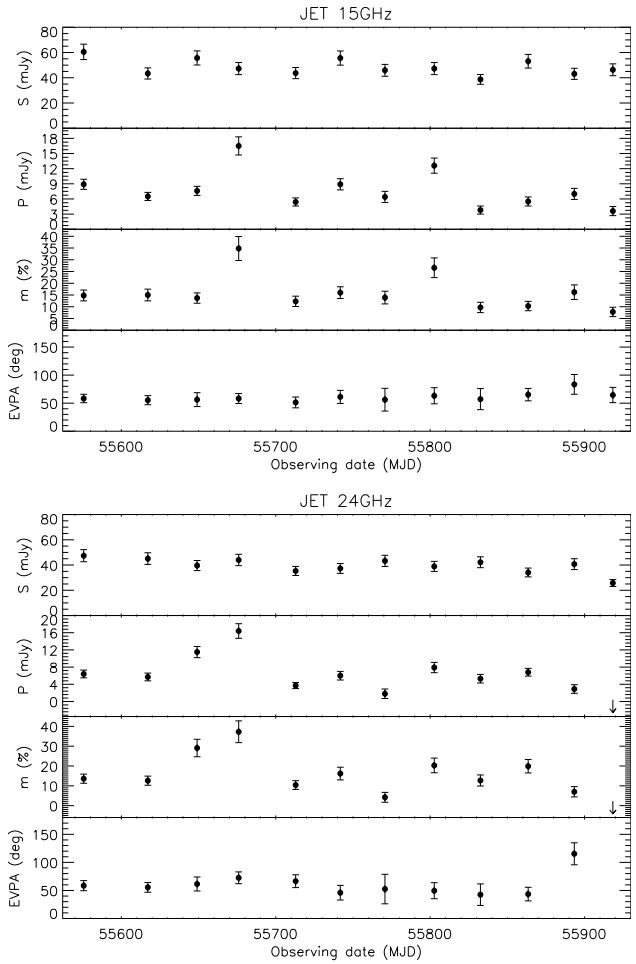

Figure 7.3: Evolution with time of some physical parameters in the jet region at 15 GHz (upper frame) and at 24 GHz (lower frame). For each frame we report from the first to the fourth panel the light curves for the total intensity, the polarized flux density, the fractional polarization, and the EVPA values.

ization percentage in the jet region is about 16%; this increase of the polarization degree with the distance from the core seems to be a common feature in blazars (Lister 2001). Finally, the EVPAs are also quite stable, fluctuating weakly around a value of 60°, i.e., roughly perpendicular to the jet position angle ($\sim -35°$).

7.3.3 Faraday rotation analysis

A polarized wave propagating through a magnetized plasma is affected by Faraday rotation. As a consequence, the observed polarization angle ($\chi_{\rm obs}$) appears rotated with respect to its intrinsic value ($\chi_{\rm int}$). This effect is described by a linear relationship between $\chi_{\rm obs}$ and the observing wavelength squared (λ^2):

$$\chi_{\rm obs} = \chi_{\rm int} + RM \times \lambda^2, \tag{7.6}$$

where RM represents the rotation measure, a quantity related to the electron density n_e (cm^{-3}), the parallel to the line of sight, aberrated by relativistic motion, component of the magnetic field $\mathbf{B}_{\parallel}$ (milligauss), and the path length dl (parsecs):

$$RM = 812 \times \int n_e \mathbf{B}_{\parallel} \cdot dl \quad [\text{rad m}^{-2}]. \tag{7.7}$$

For the core region, where EVPA values at 15, 24, and 43 GHz for each observing epoch are available (see Table 7.3), we performed linear fits of EVPAs versus λ^2, obtaining the RM and $\chi_{\rm int}$ values and uncertainties (Table 7.4). Since the two flips of EVPAs observed at 15 GHz in July and September strongly suggest optically thin-thick transitions, we carried out RM fits using EVPA values rotated by 90° at 15 GHz in these epochs. All of these linear fits are reported in Fig. 7.4; in some cases they show significant scatter about a linear trend (e.g., in February 2011), and in other cases they agree well with a linear behavior (e.g., in December 2011). The time evolution of RM values and of the intrinsic EVPA values are reported in the upper and lower panels of Fig. 7.5, respectively.

The RM values are distributed across a wide range of values, spanning ($-3640\pm$

Table 7.4: Rotation measure and intrinsic polarization angle values for the core region. Col. 1: observing date; col. 2: obseving MJD; col. 3: Rotation measure in rad m^{-2}; col. 4: estimated error for the rotation measure; col. 5: intrinsic polarization angle in deg; col. 6: estimated error for the intrinsic polarization angle.

Epoch	MJD	RM	σ_{RM}	χ	σ_χ
year/month/day		(rad m^{-2})	(rad m^{-2})	(°)	(°)
2011/01/14	55576	−710	650	127	10
2011/02/25	55617	−450	590	132	9
2011/03/29	55649	1450	880	148	13
2011/04/25	55676	1940	750	132	11
2011/05/31	55713	−1060	850	163	10
2011/06/29	55742	−1570	790	141	12
2011/07/28	55771	−2930	1380	178	20
2011/08/29	55803	−3640	930	168	13
2011/09/28	55833	−3500	1250	180	18
2011/10/29	55863	−1310	750	135	12
2011/11/28	55893	−1970	1180	147	17
2011/12/23	55918	−2370	930	168	13

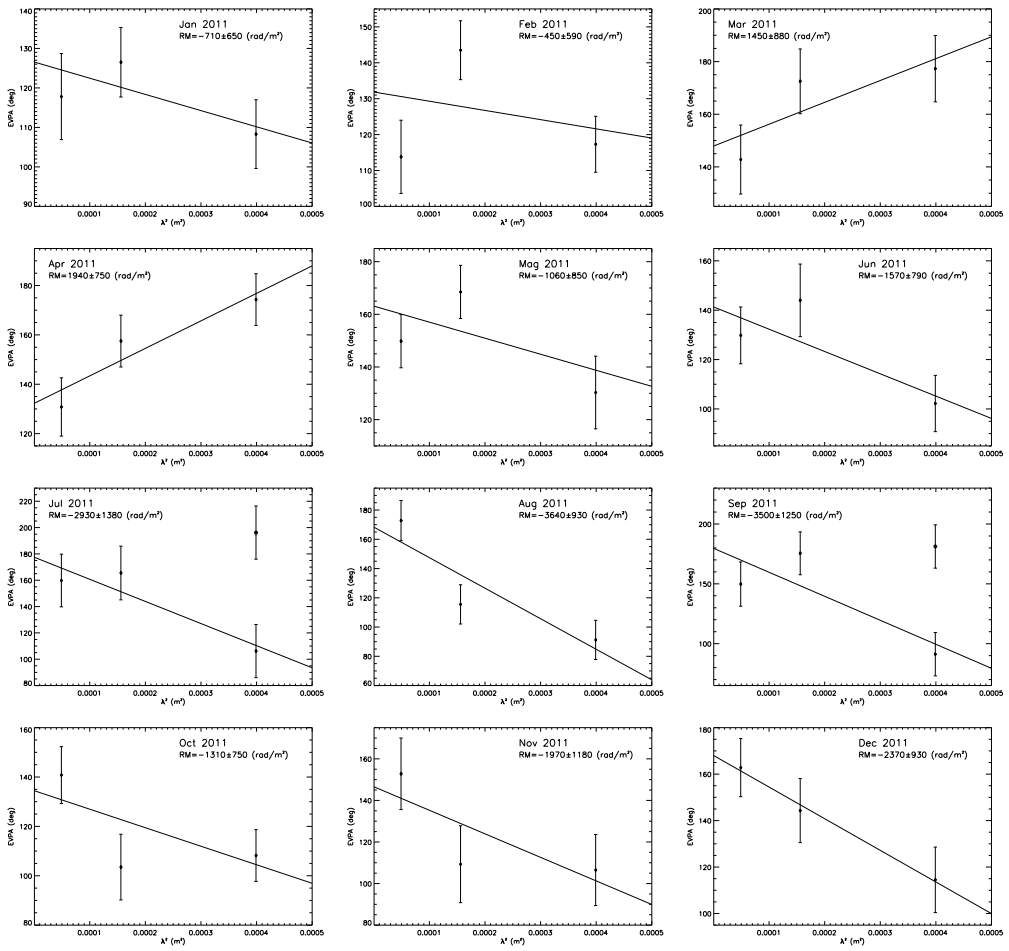

Figure 7.4: EVPAs versus λ^2 linear fits for all the observing epochs. We also show the 15 GHz EVPAs with empty symbols as measured in the images, i.e. before the rotation of 90° applied for July and September to account for opacity effects.

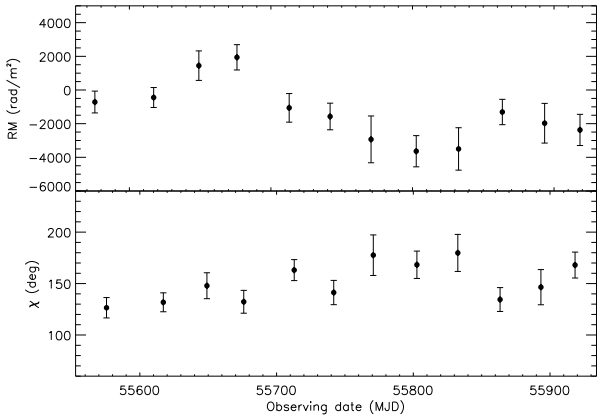

Figure 7.5: Upper panel: time evolution for the RM values derived for the core region using 15, 24, and 43 GHz data. Lower panel: time evolution for the intrinsic values of the polarization angle obtained from the λ^2 fits.

930) to (+1940 ± 750) rad m^{-2}. However, the uncertainties are often very large, with many values being consistent with 0 within 1σ or 2σ. It is thus difficult to provide accurate values and even more difficult to claim significant variability during the year. For the intrinsic values of the polarization angle, the results tend to reflect the roughly stable behavior observed for the 43 GHz EVPAs, with a value of about 150°, that is roughly parallel to the jet axis (see Fig. 7.5). However, there is some residual, mildly significant variability (see Sect. 7.4.2) (F_{var} is 0.10 ± 0.04).

7.3.4 γ-ray light curves from *Fermi* data

After integrating over the period 2011 January 1 - December 31, we obtain a fit with a power-law model in the 0.1-100 GeV energy range that results in TS = 8728 ($\sim 93\,\sigma$), with an average flux of $(17.4 \pm 0.5) \times 10^{-8}$ ph cm^{-2} s^{-1}, a photon index of $\Gamma = 1.77 \pm 0.02$, and an apparent isotropic γ-ray luminosity of 7.5×10^{44} erg s^{-1}, which is fully compatible with the values obtained over the first two years of *Fermi* operation (Nolan et al. 2012). In Fig. 7.6 we show the γ-ray flux using time bins

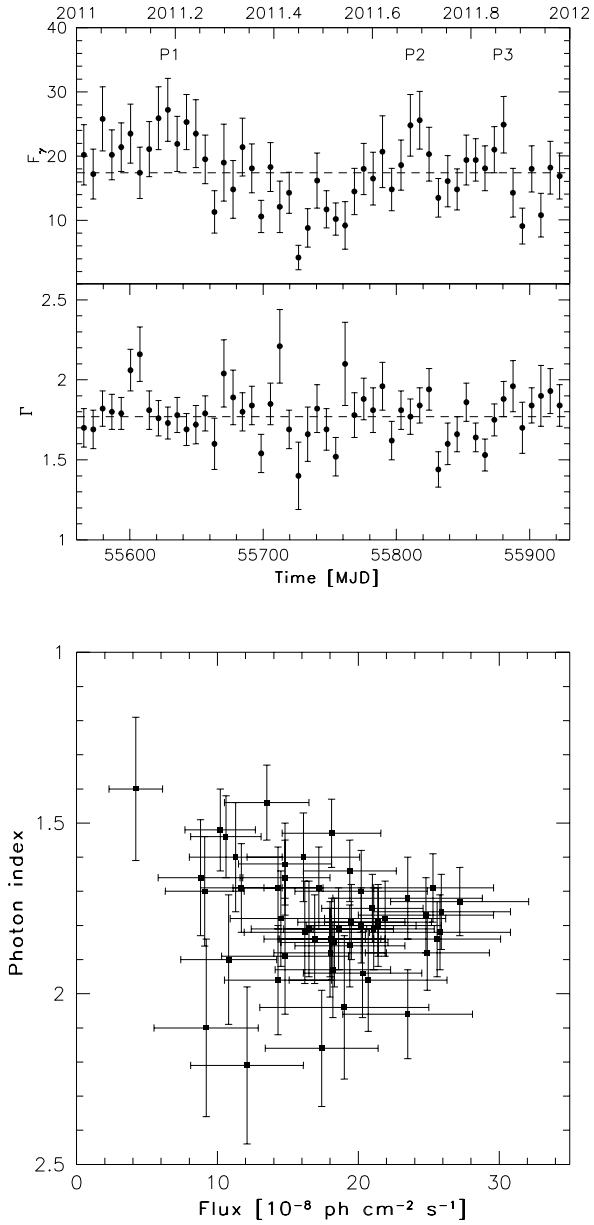

Figure 7.6: 0.1-100 GeV flux in units of 10^{-8} ph cm^{-2} s^{-1} (top panel) and the photon index from a power-law fit (bottom panel) for Mrk 421 for time intervals on one week during 2011 (from MJD 55562 to MJD 55926). The dashed line in both panels represents the mean value. In the right frame we show the scatter plot of the photon index vs the γ-ray flux.

of one week (top panel) and the photon index variation (bottom panel) over the entire observing period. For each time bin, the spectral parameters for Mrk 421 and for all the sources within a radius of 10° were left free to vary.

In the γ-ray light curve we identify three peaks: a main peak (P1) in the first observing period (2011 March 5-11, MJD 55625-55631) with a subsequent decrease to the lowest flux level in 2011 June, followed by two other peaks in the final observing period (P2 in 2011 September 3-16, MJD 55807-55820; P3 in 2011 November 12-18, MJD 55877-55883).

The daily peak flux during P1 is $(38 \pm 11) \times 10^{-8}$ ph cm^{-2} s^{-1}, observed on 2011 March 7, corresponding to an apparent isotropic γ-ray luminosity of 1.6×10^{45} erg s^{-1}. The daily peak flux during P2 and P3 is $(37 \pm 12) \times 10^{-8}$ ph cm^{-2} s^{-1} and $(30 \pm 9) \times 10^{-8}$ ph cm^{-2} s^{-1}, observed on September 8 and November 13, respectively.

Spectral hardening during flares has been seen in some blazars, in particular FSRQs (e.g., PKS 1510−089; D'Ammando et al. 2011). This sort of behavior is not without precedent in BL Lacs, but it is rare (e.g., Gasparrini 2011; Raiteri et al. 2013). Consistent with the trend for BL Lacs in general, and for Mrk 421 in particular (e.g., Abdo et al 2011), we do not detect any spectral hardening in Mrk 421 during the periods of enhanced γ-ray activity, and no obvious relation is observed between the photon index versus the γ-ray flux (see Fig. 7.6). Furthermore, the photon index is generally compatible with the average, ranging from 1.4 to 2.2.

7.3.5 Correlation between radio and γ-ray data

The comparison of the 15, 24, and 43 GHz radio core and γ-ray light curves suggests similar trends. We calculated the Pearson correlation coefficient between the radio core flux density at each epoch and frequency and the γ-ray flux during the weekly period containing the radio observations. We report these results in Table 7.5. All of the radio data sets show a strong mutual correlation, with coefficients in the range $0.88 - 0.96$. The correlation coefficients between radio and

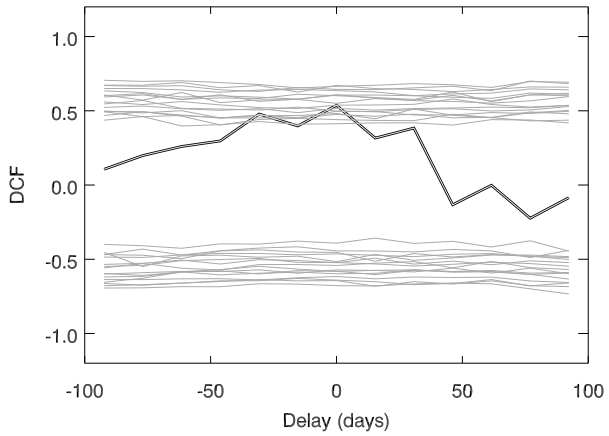

Figure 7.7: Discrete cross-correlation function between the γ-ray and 43 GHz radio light curves (black curve). The gray curves represent the 99.7% confidence limits relative to stochastic variability, obtained from the combination of different power spectral density slopes.

γ-ray data are lower, in the range 0.42 – 0.46; the strongest correlation is found with the data at 43 GHz, where the largest number of data points is available.

To assess the significance of this correlation and to determine a possible time lag, we calculated the discrete cross-correlation function (DCF) between the radio core flux density at 43 GHz and the γ-ray flux. The results of the correlation analysis are shown in Fig. 7.7.

To compute the DCF, we used the algorithm developed by Edelson & Krolik (1988), and to determine the significance of the correlation, we followed the approach recommended by Chatterjee et al. (2008) and Max-Moerbeck et al. (2010). As recommended by Timmer & Koenig (1995), we simulated 3000 light curves with the same mean and standard deviation as the observed light curves. The power spectral density (PSD), corresponding to the power in the variability of emission as a function of timescale, is represented by a power-law PSD $\propto f^{-\beta}$, where f is the inverse of the timescale. For each set of simulations, β varies from 1 to 2.5 in steps of 0.5. The curves obtained from different combinations of differ-

ent PSD slopes, with a confidence level > 99.7%, are shown in gray in Fig. 7.7.

We investigated the delay over a range of ±100 days, with a bin of 15 days. The highest value for the correlation (0.54) is found for zero delay. As is clear from Fig. 7.7, this peak does not have a high significance level for all combinations of the different PSD slopes used here. It has a significance level > 99.7% for the combination of β lower than 1.5 for the γ-ray PSD and β ranging from 1 to 2.5 for the radio PSD. This agrees with the fact that we observe the strongest variability on shorter timescales for the γ-ray emission (flatter β) and on longer timescales for the radio emission (steeper β).

7.4 Discussion

For many decades, Mrk 421 has been a target of regular monitoring at radio frequencies, showing only moderate variability (Aller et al. 1999; Venturi et al. 2001; Fan et al. 2007; Nieppola et al. 2009). MWL campaigns have failed to reveal significant correlations between variability at high (or very high) energy and radio wavelengths (Abdo et al. 2011; Acciari et al. 2011). The variability detected within the present campaign and its possible connection to the γ-ray light curve are therefore of great interest, especially considering that they foreshadowed the dramatic and unprecedented radio and γ-ray flares in 2012 (D'Ammando & Orienti 2012; Richards et al. 2013).

7.4.1 Possible radio and γ-ray connection

We find significant variability in the first months of 2011 at all three observing frequencies (15, 24, and 43 GHz) in the total intensity emission (> 3σ difference between the highest and lowest value). During the same observing period, enhanced activity also occurred at high energies. In Fig. 7.8 we show the radio and γ-ray light curves normalized to the peak value.

Table 7.5: Pearson correlation coefficients between radio flux density and γ-ray photon flux.

Data pairs	r
r_{15-24}	0.93
r_{15-43}	0.88
r_{24-43}	0.96
$r_{15-\gamma}$	0.44
$r_{24-\gamma}$	0.42
$r_{43-\gamma}$	0.46

In the radio band, the increase of the flux density is stronger at 43 GHz, where the fractional variability amplitude F_{var} (Edelson et al. 2002; Vaughan et al. 2003) is 0.24 ± 0.06, while at longer wavelengths it corresponds to 0.13 ± 0.04 and 0.18 ± 0.05 at 15 GHz and 24 GHz. In the γ-ray light curve F_{var} is 0.17 ± 0.04, on a weekly timescale. In both radio and γ-ray energy bands, the peak value is reached close in time, although the sampling interval of our observations does not allow us to determine the date of the radio burst with a better accuracy than a few weeks.

The main peak in the radio light curve (around MJD 55621) occurs close in time with the first γ-ray peak (MJD 55627); no clear radio counterpart was observed for the second and third γ-ray enhanced activity episodes. Overall, we find a good correlation between the low-frequency and high energy emission, as shown by the high and statistically significant value of the correlation coefficient. This could indicate a co-location of the radio and γ-ray emission regions, and a size as compact as $c\,\Delta t\,\delta \sim 5.3 \times 10^{16} \times \delta$ cm, assuming $\Delta t \sim 3$ weeks.

On the other hand, the study of the possible delay between radio and γ-ray light curves, based on the DCF, did not provide significant constraints on the lag between the radio and γ-ray light curves. In fact, much longer data trains are necessary to reach highly significant lag values (for a detailed discussion of the

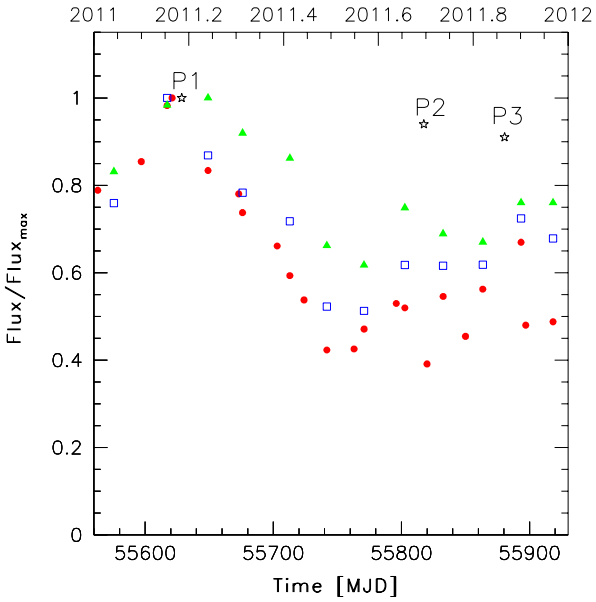

Figure 7.8: Radio light curves normalized to the peak value. Triangles, squares, and circles represent 15, 24, and 43 GHz data, respectively. All error bars (not shown) are about 0.1 mJy. The stars (labeled with P1, P2 and P3) represent the three main peaks in the γ-ray light curve normalized to the highest value.

significance of radio-gamma light curve correlation and lags, see Max-Moerbeck et al. 2013). Moreover, we note that in a recent study of the radio and γ-ray correlated variability in *Fermi* bright blazars based on 3.5 years of dense monitoring, Fuhrmann et al. (2014) did not find significant correlation between the 7mm and the γ-ray data for Mrk 421.

The proximity between the radio and γ-ray enhanced activity at the beginning of 2011 differs from what was observed in 2012, where the γ-ray flare (D'Ammando & Orienti 2012) led the radio burst by about 40 days at 15 GHz (Richards et al. 2013). However, the enhanced activities observed in 2011 and 2012 are different. The latter is characterized by a γ-ray apparent luminosity of 6.7×10^{45} erg s^{-1}, that is, about four times more powerful than the former, with simultaneous tentative detection in the TeV energy band (Bartoli et al. 2012). The different behavior of the two flares may suggest different regions for the γ-ray activity: upstream of the radio emission in the 2012 flare, while downstream along the jet where the emission is not opaque at the radio frequencies in the 2011 episode.

Interestingly, after the main peak in February 2011, which was observed both at radio and high energies, the polarized flux density at 43 GHz increases rapidly (Fig. 7.2) and peaks on 2011 March 29 (MJD 55649). Simultaneously the polarization percentage increases at 43 GHz and reaches a peak value of 3.6%, followed by a gradual decrease to the mean value ($\sim$ 1%). A similar behavior was observed by Piner & Edwards (2005) after an enhanced activity at TeV energies, when the polarization percentage of the core reached $\sim$ 5% at 22 GHz. This behavior is less pronounced in our data at 15 and 24 GHz.

In the jet region the polarized flux density and the fractional polarization reach a peak on 2011 April 25 (MJD 55675) at 15 and 24 GHz. These peaks occur just after the enhanced activity observed in the core region in total intensity emission. This behavior could be associated with a propagating disturbance, but no new components were detected in the total intensity images.

Blasi et al. (2013) investigated the behavior in the optical regime during 2011, by considering optical data provided by the Steward Observatory of the University of Arizona, finding a peak in the V magnitude occurring during the same period. The optical polarization increased from $\sim 1\%$ to $\sim 7\%$ and the optical polarization angle reduced its scatter. This may indicate that the magnetic field underwent a transition from a tangled state to a more regular one, in correspondence to the observed enhanced activity.

7.4.2 EVPA variation and magnetic field topology

To fully understand the possible relation between the enhanced activity and the physical changes occurring in the source, it is important to investigate the EVPA trend in the different regions of the source. So far, no obvious relation has been found between EVPA variation and high energy activity.

In the jet region, extending about 1 mas from the VLBI core, the EVPAs maintain a stable value of about 60° during the entire observing period, roughly perpendicular to the inner jet position angle, which is $\sim -35°$. This implies that the magnetic field is parallel to the jet axis, which is a rare behavior in BL Lac objects. However, we note that previous VLBI observations of Mrk 421 had indicated this peculiar magnetic field configuration in its parsec scale jet (Piner & Edwards 2005). This configuration could be caused either by velocity shear across the jet or by a helical magnetic field with a pitch angle smaller than 45° (Wardle 2013). At 24 GHz, we observe an EVPA rotation of about 60° at the end of 2011 (MJD 55893). This behavior may be associated with the propagation of a shock, but no new component and no significant motion were detected in total intensity images. We note that the nondetection of the jet polarized emission at the following epoch (MJD 55918) results in a lack of the EVPA, which does not allow us to confirm the possible EVPA rotation.

In the core region, the EVPA trend is more complex. At 43 GHz, where the Faraday rotation effects are weaker, the EVPAs are roughly stable in a range of

values between $\sim$ 100° and $\sim$ 150°, that is, roughly parallel to the jet axis. This trend is then reflected in the intrinsic values of the polarization angle, obtained from the λ^2 fits (see the lower panel in Fig. 7.5). Assuming that this emission region is optically thin at 43 GHz, the EVPA configuration reflects a magnetic field nearly orthogonal to the jet axis, which is typical of the emission from a transverse shock and different from what is observed in the outer jet. A similar behavior was reported in Piner & Edwards (2005): they found parallel EVPAs both in the core and in the innermost jet component (at ∼0.3 mas from the core). The extent of the validity of the optically thin emission assumption can be debated. However, the average core spectral index between 15 and 43 GHz in our data is $\alpha = 0.20 \pm 0.13$ (see also Blasi et al. 2013), suggesting that at 43 GHz the emission region is predominantly optically thin.

Considering the low frequencies, in particular at 15 GHz, we find at least two clear flips of the core EVPAs by about 90° (from parallel to perpendicular to the jet, in July and September, with a smaller change also in March). A similar behavior for the EVPAs in the VLBI core region of Mrk 421 was observed also by Charlot et al. (2006). They measured a rotation of $\sim$ 60° during a three-month period at 15 and 22 GHz. This behavior is the typical signature of a transition between an optically thin and thick regime, in which the EVPA swings from perpendicular to parallel to the magnetic field direction. Indeed, both in July and September the spectral index flattens ($\Delta\alpha^{15-43}_{\mathrm{Jul-Jun}} = -0.17$ and $\Delta\alpha^{15-43}_{\mathrm{Sep-Aug}} = -0.13$). To account for these variations solely by an opacity effect, we adopted in this discussion the core 15 GHz EVPAs rotated by 90° for the July and September data, as we already did in determining the RM fits in Sect. 7.3.3.

To explain the observed variability at longer wavelengths, a possible physical scenario might be an association with opacity effects and variable Faraday rotation. The RM variability might be related to changes in the accretion rate, as suggested also by the similar trends found for the RM and the core flux density evolution (for viable explanations of the RM sign change in relativistic jets, see

also O'Sullivan & Gabuzda 2009 and Gómez et al. 2011).

Finally, residual variability (F_{var} is 0.10 ± 0.04) is present in the intrinsic (Faraday de-rotated) EVPAs. This intrinsic variability can be the consequence of a blend of variable cross-polarized subcomponents within the beam, whose relative contributions to the total polarization properties vary as a function of time. This structure explains both the variations of the intrinsic EVPA values, which are integrated over the VLBI core region, and the low polarization of the core, resulting from significant cancellation from subcomponents with different EVPAs.

The cross-polarized subcomponents can be explained by two different physical scenarios: (1) the jet base might be turbulent, so that the subcomponents would be turbulent cells with random field direction; (2) the core magnetic field might be perpendicular to the jet, but with much of the emission optically thick at 15 GHz, giving rise to EVPAs parallel to the jet in the optically thin part and EVPAs perpendicular to the jet in the optically thick part. In either scenario the intrinsic EVPA variations are the direct consequence of changes in the relative weight of one component with respect to the other(s). The second scenario seems to be favored by the observed behavior at 43 GHz (EVPAs stable in the range 100°-150°).

The relevance of subcomponent blending can be directly seen in the April data (MJD 55675): the 43 GHz polarization image shows a transverse EVPA distribution and a limb-brightened structure in the polarized emission in the inner part of the jet (see the lower panel in Fig. 7.1). We argue that velocity gradients in this region might cause Kelvin-Helmholtz instabilities that would heat the boundary layer, causing the limb brightening. A similar transverse structure for this source was observed by Piner et al. (2010) at 22 GHz. These authors noted that the EVPAs were almost parallel along the jet axis and became orthogonal toward the jet edges. This is similar to what we observe in the EVPAs in the western limb. This may reflect a spine plus layer polarization structure and seems to be a common feature in TeV blazars, such as Mrk 501 (e.g., Giroletti et al. 2008; Piner et al.

2010).

The observed transverse EVPA rotation implies a complex topology for the magnetic field. For example, Lyutikov et al. (2005) argued that such a transverse EVPA distribution may be consistent with a large scale helical magnetic field in a resolved cylindrical jet. This transverse polarization structure would reflect the intrinsic magnetic field geometry, and not the propagation of a shock arising from the core and interacting with the surrounding medium (Lyutikov et al. 2005; Gabuzda et al. 2004). Finally, we observe that, contrary to what was found by Piner et al. (2010), no increase of the fractional polarization towards the jet edges is observed in our data. This may be due to the high activity state of Mrk 421, causing an enhancement of the polarized emission from the core region.

Conclusions

In this thesis work we presented the physical and statistical properties of HSP blazars, by using a combined approach: from one hand we explored the statistical properties of a large and homogeneous sample of hard γ-ray blazars, included in the 1FHL *Fermi* catalog, on the other hand we investigated the parsec scale properties by means of an intensive multi-frequency and multi-epoch VLBI monitoring, carried out during 2011, of one of the most remarkable HSP blazars Mrk 421.

In the following we summarize the main results, implications, and perspectives of the present thesis work.

Unassociated γ-ray sources.

In Chapter 4 we presented 5 GHz VLBA observations of the faintest γ-ray sources of the 1FHL *Fermi* catalog. We reveal a VLBI compact component for 51 sources, thus confirming their blazar nature. For these sources we obtained brightness temperature values of the order of 2×10^{10} K, which are close to the expected value for equipartition. The obtained T_B^{obs} values do not require high Doppler factors and there is not evidence of a strong beaming.

In particular, thanks to the new VLBI observations, we proposed low frequency counterparts for 11 1FHL UGS. In more detail, for 8 out of the 11 selected 1FHL UGS our proposed low-frequency counterparts are in agreement with those proposed by using indirect and complementary association methods based on the analysis of their MWL properties, such as the investigation of the low-frequency spectral index and the infrared colors. For the remaining three 1FHL UGS we

propose for the first time a low-frequency counterpart.

Our method to associate UGS is based on the detection of a high brightness temperature component, thus it naturally favors the selection of UGS similar to the associated ones. This hypothesis is supported by the fact that both 5 GHz VLBI and 1.4 GHz NVSS flux densities for the AGNs and the UGS have a similar distribution, and by the VLBI spectral indexes, which are either flat or inverted.

In this area, future sensitive observations with SKA will provide massive datasets for a systematic search of UGS blazar counterparts. On the hand, ones all blazars hidden in the UGS population will be revealed, the remaining sources will form a population worth of a dedicated investigation to understand their true, possibly exotic, nature.

Radio and γ-ray emission connection.

In Chapter 5 we explored the possible existence of a correlation between radio and γ-ray emission. We considered the most complete and unbiased sample available at present, composed of 231 blazars from the 1FHL sky survey catalog. Overall, the radio VLBI and hard γ-ray emission ($E > 10$ GeV) appears to be uncorrelated ($r = -0.02$), even when BL Lacs and FSRQs are considered separately. On the other hand, when we consider soft γ-ray energies ($E > 0.1$ GeV) we find a strong and significant correlation ($r = 0.73$, $p < 10^{-6}$).

When we consider the single SED classes, HSP objects are the only blazar subclass showing strong and significant correlation between radio VLBI flux densities and hard γ-ray energy fluxes ($r = 0.60, p = 0.0032$). When soft γ-ray energy fluxes are considered the radio and γ-ray correlation for HSP blazars becomes even higher ($r = 0.76$, $p = 2 \times 10^{-6}$).

We explain and give an interpretation of these findings in the framework of the blazar SED properties. The most powerful objects, in general BL Lacs and FSRQs of the LSP type, show soft γ-ray spectra with the high energy component peaking at energies lower than those sampled by the *Fermi*-LAT. Moreover, when

we focus on the 1FHL energy range, limited to the highest LAT energies ($E > 10$ GeV), the emission decreases further, because of cooling losses of the emitting particles and the $\gamma\gamma$ absorption processes.

On the other hand, weak objects, i.e. blazars of HSP type, suffer less cooling losses and their synchrotron peaks reach higher frequencies with respect to the most powerful objects. The part of the energy spectrum affected by cooling effects is located beyond the entire *Fermi*-LAT energy range, therefore we are considering their rising spectrum both when we consider $E > 0.1$ GeV and $E > 10$ GeV.

Parsec-scale properties of the HSP blazar Mrk 421.

In Chapters 6 and 7, we have presented the results of a broadband monitoring campaign on the HSP blazar Mrk 421. Mrk 421 is one of the brightest and closest and as such it is one of the few blazars that are continuously monitored over the whole electromagnetic spectrum, since the launch of *Fermi* in 2008.

Radio properties: total intensity and polarisation.

In Chapter 6, we focused on the multi-frequency, multi-epoch, full polarization VLBA monitoring. We do not find any evidence of strong relativistic beaming in the relativistic jet of Mrk 421: we obtain a variability brightness temperature of the order of 2×10^{10} K, a jet/counter-jet brightness ratio R>250, and we exclude the presence of superluminal motions with high confidence. These results provide the strongest evidence of a "Doppler factor crisis" in Mrk 421, and in HSP and TeV blazars in general.

In Chapter 7 we investigated the polarization properties of Mrk 421, which appear to be variable with time, frequency and location along the jet. We found the core region to be polarized by about 1% while the jet region showed an average fractional polarization of $\sim$ 16%. In the jet region EVPAs were roughly orthogonal to the jet position angle, implying a magnetic field parallel to the jet axis, which could be caused by velocity shear across the jet. In the core region, the EVPAs varied between $\sim 100^\circ$ and $\sim 150^\circ$ at 43 GHz, but they were more variable at

lower frequencies, in particular at 15 GHz, because of opacity effects and variable Faraday rotation. Near the VLBI radio core we found a limb-brightened structure in polarized emission and a transverse EVPA distribution, which supports the presence of a transverse velocity structure within the jet (e.g. spine/layer model). The velocity gradients, within the jet, might cause Kelvin-Helmholtz instabilities that would heat the boundary layer, causing the observed limb brightening. To explain the intrinsic EVPA variations in the core region, we proposed sub components within the VLBI core region, with different polarization properties, which also result in the low degree of polarization.

Radio and γ-ray connection.
During the one-year observing period the source showed both significant radio flux density and γ-ray flux variability. In particular, in the first part of 2011 we detected an enhanced γ-ray activity which appears to be associated with a prominent peak in the total intensity radio light curves, as well as with a peak occurred in the 43 GHz core polarized emission. By means of a DCF analysis we obtained a correlation coefficient of 0.54 at zero delay, between the radio core and the γ-ray light curves, at a significance level of <99.7%. Such evidence of radio and γ-ray connection for a HSP blazar in a relatively quiescent state was never observed before, and provides a starting point for future broadband analyses that could improve our knowledge about the emission of HSP blazars.

Throughout this thesis work we pointed out how and how much the new generation radio telescope SKA will improve the knowledge in blazar physics, thanks to its μJy sensitivity, large field of view and multi-beam observing capability. Thanks to the high sensitivity circular and linear polarization observations SKA will help us to investigate and understand the sub-parsec magnetic field topology, the Jet formation, collimation, composition, evolution, and the interaction with the surrounding medium, as well as the origin of intrinsic jet power differences in radio-loud AGNs (Agudo et al. 2015). In particular, thanks to the synergy of SKA with

CTA, it will be possible to definitively explore the possible radio-VHE emission connection and reveal the true nature of *Fermi* UGS.

Acknowledgments

Part of the results of this work are based on observations obtained through the BG207 and S6340 VLBA projects, which makes use of the Swinburne University of Technology software correlator, developed as part of the Australian Major National Research Facilities Programme and operated under licence (Deller et al. 2011). This research has made use of NASA's Astrophysics Data System. The National Radio Astronomy Observatory is a facility of the National Science Foundation operated under cooperative agreement by Associated Universities, Inc. For this thesis work we made use of the NASA/IPAC Extragalactic Database NED which is operated by the JPL, Californian Institute of Technology, under contract with the National Aeronautics and Space Administration. This research has made use of the VizieR catalogue access tool, CDS, Strasbourg, France. The *Fermi*-LAT Collaboration acknowledges support for LAT development, operation and data analysis from NASA and DOE (United States), CEA/Irfu and IN2P3/CNRS (France), ASI and INFN (Italy), MEXT, KEK, and JAXA (Japan), and the K.A. Wallenberg Foundation, the Swedish Research Council and the National Space Board (Sweden). Science analysis support in the operations phase from INAF (Italy) and CNES (France) is also gratefully acknowledged. Part of this work was supported by the Marco Polo program of the University of Bologna and the COST Action MP0905 "Black Holes in a Violent Universe". This research has made use of Topcat (Taylor 2005).

I would like to thank Marcello, which for me is a mentor, a tutor, a teacher and above all a friend. He really taught me a lot and made this thesis work possible.

It is very difficult to find the right words to express my gratitude to him. Many thanks to Monica for her patience and all of the precious and precise suggestions and discussions which significantly improved this thesis work and my professional knowledge.

I would like to thank Prof. Giovannini for the wise guidance, the valuable advice, and all of the great opportunities provided to me during these three years of PhD. Many thanks to my polarization instructor and friend Dr. José Luis Gómez (I had a huge benefit from his IDL support), to Dr. Vaso Pavlidou for the precious support for the statistical analysis, to Dr. Sevtlana Jorstad and Prof. Alan Marsher for hosting me at the Boston University and for their great scientific support. I would like to thank Filippo for the "high energy" support, Carolina for introducing me in the world of polarization, Prof. Thomas Krichbaum, Prof. Glenn Piner, Dr. David Paneque, Dr. Motoki Kino, Dr. Miguel Perez-Torres, Prof. Yuri Kovalev, Dr. Bill Cotton, Prof. Philip Edwards, Dr. Lars Fuhrmann, and Dr. Kirill Sokolovsky for the fruitful comments and discussions about some of the results of the present thesis work.

Infine, un ringraziamento speciale ai miei genitori, che mi hanno insegnato a non puntare mai sulle cose materiali e a cercare sempre la più intima essenza delle cose.

Bibliography

Abdo, A. A., Ackermann, M., Ajello, M., et al. 2009a, ApJ, 700, 597

Abdo, A. A., Ackermann, M., Ajello, M., et al. 2009b, ApJS, 183, 46

Abdo, A. A., Ackermann, M., Agudo, I., et al. 2010a, ApJ, 716, 30

Abdo, A. A., Ackermann, M., Ajello, M., et al. 2010b, ApJS, 188, 405

Abdo, A. A., Ackermann, M., Ajello, M., et al. 2010c, ApJ, 715, 429

Abdo, A. A., Ackermann, M., Ajello, M., et al. 2011, ApJ, 736, 131

Acciari, V. A., Aliu, E., Arlen, T., et al. 2011, ApJ, 738, 25

Acero, F., Ackermann, M., Ajello, M., et al. 2015, ApJS, 218, 23

Ackermann, M., Ajello, M., Allafort, A., et al. 2011a, ApJ, 741, 30

Ackermann, M., Ajello, M., Allafort, A., et al. 2011b, ApJ, 743, 171

Ackermann, M., Ajello, M., Albert, A., et al. 2012a, ApJS, 203, 4

Ackermann, M., Ajello, M., Allafort, A., et al. 2012b, Science, 338, 1190

Ackermann, M., Ajello, M., Allafort, A., et al. 2013, ApJS, 209, 34

Ackermann, M., Albert, A., Atwood, W. B., et al. 2014, ApJ, 793, 64

Ackermann, M., Ajello, M., Atwood, W. B., et al. 2015, ApJ, 810, 14

Agudo, I., Boettcher, M., Falcke, H. D. E., et al. 2015, aska.conf, 93

Aharonian, F., Akhperjanian, A. G., Bazer-Bachi, A. R., et al. 2007, ApJ , 664, L71

Aller, M. F., Aller, H. D., Hughes, P. A., & Latimer, G. E. 1999, ApJ, 512, 601

Atwood, W. B., Abdo, A. A., Ackermann, M., et al. 2009, ApJ, 697, 1071

Barkov, M. V., Aharonian, F. A., Bogovalov, S. V., Kelner, S. R., & Khangulyan, D. 2012, ApJ, 749, 119

Bartoli, B., Bernardini, P., Bi, X. J., et al. 2012, The Astronomer's Telegram, 4272, 1

Beckmann, V., & Shrader, C. 2012, Proceedings of the 9th INTEGRAL Workshop and celebration of the 10th anniversary of the launch (INTEGRAL 2012).PoS(INTEGRAL 2012)069

Begelman, M. C., Fabian, A. C., & Rees, M. J. 2008, MNRAS, 384, L19

Blandford, R. D., & Rees, M. J. 1978, PhyS, 17, 265

Blandford, R. D., & Payne, D. G. 1982, MNRAS, 199, 883

Blasi, M. G., Lico, R., Giroletti, M., et al. 2013, A&A, 559, A75

Böttcher, M., & Dermer, C. D. 2002, ApJ, 564, 86

Caccianiga, A., Maccacaro, T., Wolter, A., Della Ceca, R., & Gioia, I. M. 2002, ApJ, 566, 181

Charlot, P., Gabuzda, D. C., Sol, H., Degrange, B., & Piron, F. 2006, A&A, 457, 455

Chatterjee, R., Jorstad, S. G., Marscher, A. P., et al. 2008, ApJ, 689, 79

Chiaberge, M., Celotti, A., Capetti, A., & Ghisellini, G. 2000, A&A, 358, 104

Chiaberge, M., & Marconi, A. 2011, MNRAS, 416, 917

Cornwell, T. J. 2009, A&A, 500, 65

D'Abrusco, R., Massaro, F., Paggi, A., et al. 2013, ApJS, 206, 12

D'Ammando, F., Raiteri, C. M., Villata, M., et al. 2011, A&A, 529, A145

D'Ammando, F., & Orienti, M. 2012, The Astronomer's Telegram, 4261, 1

D'Elia, V., & Cavaliere, A. 2001, Blazar Demographics and Physics, ASP Conference Series, 227, 252

Deller, A. T., Brisken, W. F., Phillips, C. J., et al. 2011, PASP, 123, 275

Dermer, C. D., Schlickeiser, R., & Mastichiadis, A. 1992, A&A, 256, L27

de Vaucouleurs, G., de Vaucouleurs, A., Corwin, H. G., Jr., et al. 1991, Third Reference Catalogue of Bright Galaxies. Volume I: Explanations and references. Volume II: Data for galaxies between 0^h and 12^h. Volume III: Data for galaxies between 12^h and 24^h (New York, NY:Springer).

Donato, D., Ghisellini, G., Tagliaferri, G., & Fossati, G. 2001, A&A, 375, 739

Edelson, R. A., & Krolik, J. H. 1988, ApJ, 333, 646

Edelson, R., Turner, T. J., Pounds, K., et al. 2002, ApJ, 568, 610

Elvis, M., Wilkes, B. J., McDowell, J. C., et al. 1994, ApJS, 95, 1

Fan, J. H., Liu, Y., Yuan, Y. H., et al. 2007, A&A, 462, 547

Fanti, C., Pozzi, F., Dallacasa, D., et al. 2001, A&A, 369, 380

Finke, J. D., & Dermer, C. D. 2010, ApJ, 714, L303

Fossati, G., Maraschi, L., Celotti, A., Comastri, A., & Ghisellini, G. 1998, MNRAS, 299, 433

Fuhrmann, L., Larsson, S., Chiang, J., et al. 2014, MNRAS, 441, 1899

Gabuzda, D. C., Murray, É., & Cronin, P. 2004, MNRAS, 351, L89

Gabuzda, D. C., Reichstein, A. R., & O'Neill, E. L. 2014, MNRAS, 444, 172

Gaidos, J. A., Akerlof, C. W., Biller, S., et al. 1996, Natur, 383, 319

Gasparrini, D. 2011, TheAstronomer's Telegram, 3462, 1

Georganopoulos, M., & Kazanas, D. 2003, ApJ, 594, L27

Ghirlanda, G., Ghisellini, G., Tavecchio, F., & Foschini, L. 2010, MNRAS, 407, 791

Ghirlanda, G., Ghisellini, G., Tavecchio, F., Foschini, L., & Bonnoli, G. 2011, MNRAS, 413, 852

Giannios, D., Uzdensky, D. A., & Begelman, M. C. 2009, MNRAS, 395, L29

Ghisellini, G., & Madau, P. 1996, MNRAS, 280, 67

Ghisellini, G., Celotti, A., Fossati, G., Maraschi, L., & Comastri, A. 1998, MNRAS, 301, 451

Ghisellini, G., & Celotti, A. 2001, A&A, 379, L1

Ghisellini, G., Tavecchio, F., & Chiaberge, M. 2005, A&A, 432, 401

Ghisellini, G., Tavecchio, F., Foschini, L., & Ghirlanda, G. 2011, MNRAS, 414, 2674

Giommi, P., Polenta, G., Lähteenmäki, A., et al. 2012a, A&A, 541, A160

Giommi, P., Padovani, P., Polenta, G., et al. 2012b, MNRAS, 420, 2899

Giovannini, G., Taylor, G. B., Feretti, L., et al. 2005, ApJ, 618, 635

Giroletti, M., Giovannini, G., Feretti, L., et al. 2004b, ApJ, 600, 127

Giroletti, M., Giovannini, G., Taylor, G. B., & Falomo, R. 2004a, ApJ, 613, 752

Giroletti, M., Giovannini, G., Taylor, G. B., & Falomo, R. 2006, ApJ, 646, 801

Giroletti, M., Giovannini, G., Cotton, W. D., et al. 2008, A&A, 488, 905

Giroletti, M., & Panessa, F. 2009, ApJ, 706, L260

Giroletti, M., Reimer, A., Fuhrmann, L., Pavlidou, V., & Richards, J. L. 2010, arXiv:1001.5123

Giroletti, M., Orienti, M., D'Ammando, F., et al. 2015, aska.conf, 153

Gómez J. L., Marcher, A., Alberdi, A., et al. 2002, NRAO Scientific Memos, n° 30

Gómez, J. L., Roca-Sogorb, M., Agudo, I., Marscher, A. P., & Jorstad, S. G. 2011, ApJ, 733, 11

Gould, R. J., & Schréder, G. P. 1967, Physical Review, 155, 1408

Greisen, E. W. 2003, ASSL, 285, 109

Harris, J., Daniel, M. K., & Chadwick, P. M. 2012, ApJ, 761, 2

Henri, G., & Saugé, L. 2006, ApJ, 640, 185

Hovatta, T., Valtaoja, E., Tornikoski, M., Lähteenmäki, A. 2009, A&A, 494, 527

Hovatta, T., Pavlidou, V., King, O. G., et al. 2014, MNRAS, 439, 690

Huan, H., Weisgarber, T., Arlen, T., & Wakely, S. P. 2011, ApJ, 735, L28

Jorstad, S. G., Marscher, A. P., Smith, P. S., et al. 2013, ApJ, 773, 147

Kellermann, K. I., & Pauliny-Toth, I. I. K. 1969, ApJL, 155, L71

Kellermann, K. I., Sramek, R., Schmidt, M., Shaffer, D. B., & Green, R. 1989, AJ, 98, 1195

Komatsu, E., Dunkley, J., Nolta, M. R., et al. 2009, ApJS, 180, 330

Kovalev, Y. Y., Aller, H. D., Aller, M. F., et al. 2009, ApJ, 696, L17

Krolik, J. H. 1999, Active galactic nuclei : from the central black hole to the galactic environment, Princeton University Press

Landi, R., Bassani, L., Stephen, J. B., et al. 2015, arXiv:1506.07373

Leppänen, K. J., Zensus, J. A., & Diamond, P. J. 1995, AJ, 110, 2479

Lico, R., Giroletti, M., Orienti, M., et al. 2014, A&A, 571, A54

Lico, R., Giroletti, M., Orienti, M., et al. 2012, A&A, 545, A117

Lister, M. L. 2001, ApJ, 562, 208

Liuzzo, E., Giovannini, G., & Giroletti, M. 2011, arXiv:1110.6360

Lyutikov, M., Pariev, V. I., & Gabuzda, D. C. 2005, MNRAS, 360, 869

Lyutikov, M., & Lister, M. 2010, ApJ, 722, 197

MacLeod, J. M., & Andrew, B. H. 1968, ApL, 1, 243

Mahony, E. K., Sadler, E. M., Murphy, T., et al. 2010, ApJ, 718, 587

Mannheim, K. 1993, A&A, 269, 67

Maraschi, L., Ghisellini, G., & Celotti, A. 1992, ApJL, 397, L5

Marscher, A. P., & Gear, W. K. 1985, ApJ, 298, 114

Marscher, A. P. 1999, APh, 11, 19

Marscher, A. P., Jorstad, S. G., Mattox, J. R., & Wehrle, A. E. 2002, ApJ, 577, 85

Massaro, E., Giommi, P., Leto, C., et al. 2009, A&A, 495, 691

Massaro, F., D'Abrusco, R., Giroletti, M., et al. 2013a, ApJS, 207, 4

Massaro, F., D'Abrusco, R., Paggi, A., et al. 2013b, ApJS, 206, 13

Massaro, F., D'Abrusco, R., Paggi, A., et al. 2014, arXiv:1404.5960

Massaro, F., Landoni, M., D'Abrusco, R., et al. 2015, A&A, 575, A124

Mattox, J. R., Bertsch, D. L., Chiang, J., et al. 1996, ApJ, 461, 396

Max-Moerbeck, W. et al. 2010 in Fermi Meets Jansky – AGN at Radio and Gamma-rays, ed. T. Savolainen et al. (Bonn: Max-Planck-Institute Fur Radioastronomie), 77

Max-Moerbeck, W., Richards, J. L., Pavlidou, V., et al. 2013, arXiv, arXiv:1303.2131, eConf C121028

Meyer, E. T., Fossati, G., Georganopoulos, M., & Lister, M. L. 2011, ApJ, 740, 98

Mufakharov, T., Mingaliev, M., Sotnikova, Y., Naiden, Y., & Erkenov, A. 2015, MNRAS, 450, 2658

Nalewajko, K., Giannios, D., Begelman, M. C., Uzdensky, D. A., & Sikora, M. 2011, MNRAS, 413, 333

Nieppola, E., Hovatta, T., Tornikoski, M., Valtaoja, E., Aller, M. F., & Aller, H. D. 2009, AJ, 137, 5022

Nieppola, E., Tornikoski, M., Valtaoja, E., et al. 2011, A&A, 535, A69

Nolan, P. L., Abdo, A. A., Ackermann, M., et al. 2012, ApJS, 199, 31

Nori, M., Giroletti, M., Massaro, F., et al. 2014, ApJS, 212, 3

Orienti, M., Venturi, T., Dallacasa, D., et al. 2011, MNRAS, 417, 359

Orienti, M., Koyama, S., D'Ammando, F., et al. 2013, MNRAS, 428, 2418

Orr, M. R., Krennrich, F., & Dwek, E. 2011, ApJ, 733, 77

O'Sullivan, S. P., & Gabuzda, D. C. 2009, MNRAS, 393, 429

Ostriker, J. P., & Vietri, M. 1990, Nature, 344, 45

Padovani, P. 1992, A&A, 256, 399

Padovani, P., & Urry, C. M. 1992, ApJ, 387, 449

Padovani, P., Giommi, P., Landt, H., & Perlman, E. S. 2007, ApJ, 662, 182

Paggi, A., Massaro, F., D'Abrusco, R., et al. 2013, ApJS, 209, 9

Paragi, Z., Godfrey, L., Reynolds, C., et al. 2015, aska.conf, 143

Pavlidou, V., Richards, J. L., Max-Moerbeck, W., et al. 2012, ApJ, 751, 149

Peterson, B. M. 1997, An introduction to active galactic nuclei, Cambridge University Press

Piner, B. G., Unwin, S. C., Wehrle, A. E., Edwards, P. G., Fey, A. L., & Kingham, K. A. 1999, ApJ, 525, 176

Piner, B. G., & Edwards, P. G. 2004, ApJ, 600, 115

Piner, B. G., & Edwards, P. G. 2005, ApJ, 622, 168

Piner, B. G., Pant, N., & Edwards, P. G. 2008, ApJ, 678, 64

Piner, B. G., Pant, N., Edwards, P. G., & Wiik, K. 2009, ApJ, 690, L31

Piner, B. G., Pant, N., & Edwards, P. G. 2010, ApJ, 723, 1150

Piner, B. G., & Edwards, P. G. 2013, EPJWC, 61, 4021

Piner, B. G., & Edwards, P. G. 2014, ApJ, 797, 25

Pollack, L. K., Taylor, G. B., & Zavala, R. T. 2003, ApJ, 589, 733

Punch, M., Akerlof, C. W., Cawley, M. F., et al. 1992, Natur, 358, 477

Raiteri, C. M., et al. 2013,MNRAS, 436, 1530

Readhead, A. C. S. 1994, ApJ, 426, 51

Rector, T. A., Stocke, J. T., Perlman, E. S., Morris, S. L., & Gioia, I. M. 2000, AJ, 120, 1626

Richards, J. L., Max-Moerbeck, W., Pavlidou, V., et al. 2011, ApJS, 194, 29

Richards, J. L., Hovatta, T., Lister, M. L., et al. 2013, EPJWC, 61, 04010

Sakamoto, Y., Nishijima, K., Mizukami, T., et al. 2008, ApJ, 676, 113

Schinzel, F. K., Petrov, L., Taylor, G. B., et al. 2015, ApJS, 217, 4

Shepherd, M. C. 1997, ASPC, 125, 77

Sikora, M., Begelman, M. C., & Rees, M. J. 1994, ApJ, 421, 153

Sikora, M., Moderski, R., & Madejski, G. M. 2008, ApJ, 675, 71

Stern, B. E., & Poutanen, J. 2014, ApJ, 794, 8

Stickel, M., Padovani, P., Urry, C. M., Fried, J. W., & Kuehr, H. 1991, ApJ, 374, 431

Taylor, M. B. 2005, Astronomical Data Analysis Software and Systems XIV, 347, 29

Taylor, A. M., Vovk, I., & Neronov, A. 2011, A&A, 529, A144

Tavecchio, F. 2005, Proceedings of the MG10 Meeting held at CBPF, Rio de Janeiro, Brazil, 20-26 July 2003, p. 512

Tavecchio, F., Ghisellini, G., Ghirlanda, G., Foschini, L., & Maraschi, L. 2010, MNRAS, 401, 1570

Thompson, D. J., Bertsch, D. L., Fichtel, C. E., et al. 1993, ApJS, 86, 629

Timmer, J., & Koenig, M. 1995, A&A, 300, 707

Tingay, S. J., Murphy, D. W., Lovell, J. E. J., et al. 1998, ApJ, 497, 594

Urry, C. M., & Padovani, P. 1995, PASP, 107, 803

Vagnetti, F., Cavaliere, A., & Giallongo, E. 1991, ApJ, 368, 366

Vaughan, S., Edelson, R., Warwick, R. S., & Uttley, P. 2003, MNRAS, 345, 1271

Venturi, T., Dallacasa, D., Orfei, A., et al. 2001, A&A, 379, 755

Wardle, J. F. C., & Kronberg, P. P. 1974, ApJ, 194, 249

Wardle, J. F. C. 2013, EPJWC, 61, 6001